

POLITECNICO DI TORINO

Master's Degree in Civil Engineering



Master thesis

**FLUTTER IN MULTI-BOX SUSPENSION  
BRIDGES: THE CASE-STUDY OF THE  
XIHOUMEN BRIDGE**

Supervisors:

Prof. Giuseppe Lacidogna

Dr. Gianfranco Piana

Dr. Sebastiano Russo

Candidate:

Pietro Camera

Academic Year 2024/2025



*Dedico la mia Tesi a chi c'è sempre stato,  
a chi ha creduto in me, fino alla fine.*

*A mio Nonno Silvio.*

*Mi ha insegnato a credere nei sogni.  
Spero possa sorridere in questo momento,  
guardando suo nipote averli realizzati.*

## Ringraziamenti

Porgo i miei più sentiti ringraziamenti all'istituzione Politecnico di Torino e a tutti i docenti che mi hanno accompagnato durante questo percorso di studi, facendomi crescere in ambito professionale e personale.

Un particolare ringraziamento al Prof. Giuseppe Lacidogna e al Prof. Alberto Carpinteri, per aver alimentato in me la curiosità verso l'ingegneria strutturale e per avermi offerto l'opportunità di approfondire quella che, sin dalla nascita, è la mia più grande passione: i ponti sospesi.

Un sentito ringraziamento al Dott. Gianfranco Piana, che con grande professionalità e disponibilità mi ha seguito durante tutto questo stimolante percorso di Tesi.

Un sincero ringraziamento al Dott. Sebastiano Russo, che con costante presenza e disponibilità ha saputo guidarmi con i suoi preziosi suggerimenti e insegnamenti.

Ringrazio i colleghi del corso e i compagni di studio, con i quali ho avuto la fortuna di condividere parte di questo percorso ricco di emozioni e insegnamenti.

Ringrazio tutti i miei amici, che hanno contribuito ad alleggerire e rallegrare questo tortuoso cammino, sostenendomi durante ogni difficoltà.

Il ringraziamento più sentito va a tutta la mia famiglia, in particolare ai miei genitori, Paola e Luciano e a mia sorella Greta, per aver gioito e sofferto con me durante tutto il percorso.

Il raggiungimento di questo traguardo è sicuramente anche merito del vostro immancabile sostegno e supporto.

## Abstract

Multi-box suspension bridges represent an innovative structural typology, characterised by multiple decks that offer greater stability, loading capacity and reduced torsional stresses.

Until the construction of the 1915 Çanakkale Bridge, the Xihoumen Bridge (completed in 2009) was the longest multi-box suspension bridge in the world. Its deck's configuration was studied to provide much better wind resistance performance, considering the stricter stability requirement of 78.4 m/s wind speed. With this structural innovation, the critical flutter speed reaches approximately 90 m/s.

The aim of this Thesis is to investigate the *flutter instability* of the Xihoumen Bridge adopting the finite element software ANSYS APDL and an analytical code implemented in MATLAB. An extensive aeroelastic analysis is carried out studying the combination of different structural models and different aeroelastic forces defined by various sets of flutter derivatives.

The first part of the Thesis presents the theoretical and bibliographical background of *flutter analysis*, necessary to understand the objectives of the following sections. This is followed by a description of the case study, analysing its structural characteristics, design challenges, and context. Next, a chapter is dedicated to the different methodologies used for calculating *flutter derivatives*: Theodorsen's simplified method and Andersen's method based on the superposition of flat plates are tested by the comparison of the derivatives provided with those obtained experimentally through wind tunnel tests. The concept of *gap width sensitivity* and its impact on the calculation of *flutter derivatives* is explored, underlying its fundamental role in understanding the differences in the results obtained.

In the final part of this Thesis, Finite Element Models of the case study are presented. Preliminary *zero-wind modal analyses* are performed and the results provided by the various models are discussed and compared with literature data.

Subsequently, using the previously discussed *flutter derivatives*, the *flutter analyses* are carried out to determine the critical flutter frequency and the critical wind speed at which instability occurs.

In conclusion, all results are presented and discussed. The comparison of the results obtained with literature values shows that the 1-axis central span model provides the best estimate of the bridge's dynamics which consequently translates in the best agreement of flutter wind speed (lower than 4%).

Another relevant result for this model is that similar conclusions are reached using both experimental flutter derivatives and those obtained through Andersen's simplified approach, when applying the gap-width scaling factor. This is an interesting outcome, highlighting both the importance of *gap-width sensitivity* and the potential to use simpler and faster approaches to predict *flutter derivatives*.

## Table of Contents

Ringraziamenti .....	I
Abstract.....	II
Table of Contents .....	IV
List of Figures.....	VII
List of Tables.....	IX
<i>Chapter 1</i> - Introduction .....	10
1.1 Structural characteristics of suspension bridges.....	10
1.2 History evolution and records.....	12
<i>Chapter 2</i> - Notes on flutter instability of suspension bridges .....	16
2.1 Steady aerodynamic forces.....	17
2.2 2-DoF flutter.....	19
2.3 3-DoF flutter.....	22
2.4 Flutter Analysis in MATLAB .....	24
2.5 Flutter analysis in ANSYS .....	26
<i>Chapter 3</i> - Description of the case study: Xihoumen Bridge.....	29
3.1 General bridge outline .....	29
3.1.1 Suspended deck with twin box-girders.....	30
3.1.2 External constraints and expansion joints .....	31
3.1.3 Suspension system.....	32
3.1.3.1 Main cable .....	32
3.1.3.2 Hangers.....	32
3.1.4 Towers .....	34
3.1.5 Foundations .....	37
3.2 Review of literature results for modal and flutter analysis.....	38
3.2.1 Yu <i>et al.</i> studies .....	38
3.2.2 Chu <i>et al.</i> studies .....	40
3.2.3 Jiang et al. studies.....	42
<i>Chapter 4</i> - Approximate calculation of flutter derivatives.....	45

4.1	Flat plate .....	45
4.2	Superposition of flat plates .....	48
4.2.1	Gap-width sensitivity.....	49
4.3	Application to the case study.....	52
<i>Chapter 5</i>	<i>- Structural models and modal analysis results .....</i>	<i>54</i>
5.1	Analytic model (MATLAB).....	54
5.2	Finite Element Models .....	56
5.2.1	Deck Polar moment of inertia.....	57
5.2.2	Central span 1-axis model .....	60
5.2.3	Central span 2-axis model .....	64
5.2.4	Complete 1-axis model.....	68
5.2.5	Complete 2-axis model.....	72
5.3	Comparison with literature results.....	76
5.3.1	MATLAB .....	76
5.3.2	ANSYS – Central span 1-axis model .....	76
5.3.3	ANSYS - Central span 2-axis model.....	77
5.3.4	ANSYS - Complete 1-axis model .....	78
5.3.5	ANSYS – Complete 2-axis model.....	79
5.3.6	Results summary .....	79
<i>Chapter 6</i>	<i>- Xihoumen Bridge flutter analysis .....</i>	<i>80</i>
6.1	Flutter analysis in MATLAB.....	80
6.1.1	Experimental flutter derivatives .....	80
6.1.2	Andersen’s flutter derivatives.....	82
6.1.3	Andersen’s flutter derivatives with gap-width scaling factor.....	84
6.1.4	Results comparison.....	86
6.2	Flutter analysis of central-span models in ANSYS.....	88
6.2.1	Single-axis model .....	88
6.2.1.1	Experimental flutter derivatives .....	88
6.2.1.2	Andersen’s flutter derivatives.....	90
6.2.1.3	Andersen’s flutter derivatives with gap-width scaling factor.....	91
6.2.2	Double-axis model.....	92
6.2.2.1	Theodorsen’s flutter derivatives .....	92
6.2.3	Results comparison.....	93



6.3	Flutter analysis of complete models in ANSYS.....	94
6.3.1	Single-axis model .....	94
6.3.1.1	Experimental flutter derivatives .....	94
6.3.1.2	Andersen’s flutter derivatives.....	95
6.3.1.3	Andersen’s flutter derivatives with gap-width scaling factor.....	97
6.3.2	Double-axis model.....	98
6.3.2.1	Theodorsen’s flutter derivatives .....	98
6.3.3	Results comparisons .....	100
6.4	Comparison of different models’ results .....	101
<i>Chapter 7</i>	- Conclusions .....	103
References	.....	106

## List of Figures

Figure 1.1 - Suspension bridge stress scheme [3] .....	11
Figure 1.2 - Suspension bridge components[2] .....	12
Figure 1.3 – Collapse of the Tacoma Narrows Bridge .....	13
Figure 1.4 - 1915 Çanakkale Bridge in Turkey [7] .....	14
Figure 2.1 - Suspension bridge scheme[9] .....	16
Figure 2.2 - Steady aerodynamic model[10] .....	17
Figure 2.3 - Examples of aerodynamic coefficients[10] .....	18
Figure 2.4 - 2-DoFs simplified model[9] .....	20
Figure 2.5 - Examples of flutter derivatives[9] .....	21
Figure 2.6 - 3-DoFs simplified model[9] .....	22
Figure 2.7 - Perturbated configuration of 1D continuum model[14] .....	25
Figure 2.8 - Hybrid finite element model for flutter analysis in ANSYS[4].....	27
Figure 3.1 - Zhoushan Archipelago and mainland linking project[17] .....	29
Figure 3.2 - Span arrangement of the Xihoumen Bridge (Units: cm)[17] .....	29
Figure 3.3 – Overview of the Xihoumen Bridge[18] .....	30
Figure 3.4 - Typical cross section of the twin-box girder (Units: mm)[17] .....	30
Figure 3.5 - Particular of the twin-box girder deck[18] .....	31
Figure 3.6 - Cross section of the main cable[17].....	32
Figure 3.7 - Dynamic positioning of carrying boat[19] .....	32
Figure 3.8 - View of hangers and the north pylon[21] .....	33
Figure 3.9 - View of south pylon[18] .....	34
Figure 3.10 - Particular of cross beam of south pylon[18].....	35
Figure 3.11 - Arrangement of north pylon (Dimension in cm)[17].....	36
Figure 3.12 - Plan and section of pylon leg[17] .....	36
Figure 3.13 - Arrangement of south pylon[17].....	37
Figure 3.14 - Flutter derivative $H_1^*$ and $A_1^*$ .....	39
Figure 3.15 - Flow chart of assessment of flutter probability[23].....	40
Figure 3.16 - Flutter derivatives of the Xihoumen Bridge section model[23] .....	41
Figure 3.17 - Distributions of the flutter critical wind speed in 100-year structural age[23]...	42
Figure 3.18 - Three-dimensional FE model of the Xihoumen Bridge[25].....	43
Figure 4.1 - Sign convention following [12] for a single flat plate .....	46
Figure 4.2 – Real, $R(Ck)$ , and Imaginary, $I(Ck)$ , part of Theodorsen's circulatory function, $Ck$ [27] .....	47
Figure 4.3 - Example of multi-box bridge girder .....	48
Figure 4.4 - Frequencies ( $f$ ) and damping ratios ( $\zeta$ ) for the torsional dominated mode of the case-study analysed in [27], for different values of the gap-width scaling factor ( $v$ ) .....	50

Figure 4.5 - Flutter derivatives of the Xihoumen Bridge .....	52
Figure 5.1 - Xihoumen Bridge modal shapes in wind-free condition .....	55
Figure 5.2 - Scheme of 1-axis equivalent deck and cables.....	57
Figure 5.3 - Scheme of 2-axis equivalent deck and cables.....	58
Figure 5.4 – Central span 1-axis FE model with a detail on the right.....	60
Figure 5.5 - Central span 2-axis FE model with a detail on the right.....	64
Figure 5.6 - Complete 1-axis FE model with a detail on the right .....	68
Figure 5.7 - Complete 2-axis FE model with a detail on the right .....	72
Figure 6.1 - Variation of the imaginary part of complex eigenvalues.....	80
Figure 6.2 - Variation of the real part of complex eigenvalues .....	81
Figure 6.3 - Xihoumen Bridge modal shapes in critical flutter condition.....	82
Figure 6.4 - Variation of the imaginary part of complex eigenvalues.....	83
Figure 6.5 - Variation of the real part of complex eigenvalues .....	84
Figure 6.6 - Variation of the imaginary part of complex eigenvalues.....	85
Figure 6.7 - Variation of the real part of complex eigenvalues .....	86
Figure 6.8 - Variation of the imaginary part of complex eigenvalues.....	88
Figure 6.9 - Variation of the real part of complex eigenvalues .....	89
Figure 6.10 - Deformed shape at flutter critical condition .....	89
Figure 6.11 - Variation of the imaginary part of complex eigenvalues.....	90
Figure 6.12 - Variation of the real part of complex eigenvalues .....	90
Figure 6.13 - Variation of the imaginary part of complex eigenvalues.....	91
Figure 6.14 - Variation of the real part of complex eigenvalues .....	91
Figure 6.15 - Variation of the imaginary part of complex eigenvalues.....	92
Figure 6.16 - Variation of the real part of complex eigenvalues .....	92
Figure 6.17 - Variation of the imaginary part of complex eigenvalues.....	94
Figure 6.18 - Variation of the real part of complex eigenvalues.....	95
Figure 6.19 - Variation of the imaginary part of complex eigenvalues.....	96
Figure 6.20 - Variation of the real part of complex eigenvalues .....	96
Figure 6.21 - Variation of the imaginary part of complex eigenvalues.....	97
Figure 6.22 - Variation of the real part of complex eigenvalues .....	98
Figure 6.23 - Variation of the imaginary part of complex eigenvalues.....	99
Figure 6.24 - Variation of the real part of complex eigenvalues .....	99

## List of Tables

Table 1.1 - List of longest suspension bridge spans[1] .....	10
Table 1.2 - Record breaking bridges built in the world.....	15
Table 3.1 - Results of modal analysis [22] .....	39
Table 3.2 - Comparisons of critical flutter wind speed between analysis and measurement [22] .....	39
Table 3.3 - The measured modal frequencies and damping ratios from vertical vibration by different methods[23] .....	40
Table 3.4 - The calculated first nine vertical natural frequencies and mode shapes of the Xihoumen Bridge[25].....	44
Table 5.1 - Geometrical and mechanical properties of the Xihoumen Bridge .....	54
Table 5.2 - Geometrical and mechanical properties of the Xihoumen Bridge .....	61
Table 5.3 - Modal frequencies and modal shapes of the Central Span 1-axis Model .....	61
Table 5.4 - Geometrical and mechanical properties of the Xihoumen Bridge .....	65
Table 5.5 - Modal frequencies and modal shapes of the Central Span 2-axis Model .....	65
Table 5.6 - Geometrical and mechanical properties of the Xihoumen Bridge .....	69
Table 5.7 - Modal frequencies and modal shapes of the Complete 1-axis Model .....	69
Table 5.8 - Geometrical and mechanical properties of the Xihoumen Bridge .....	73
Table 5.9 - Modal frequencies and modal shapes of the Complete 2-axis Model .....	73
Table 5.10 – MATLAB Modal frequencies comparison.....	76
Table 5.11 - ANSYS – Central span 1-axis model modal frequencies comparison.....	76
Table 5.12 - ANSYS – Central span 2-axis model modal frequencies comparison.....	77
Table 5.13 - ANSYS – Complete 1-axis model modal frequencies comparison .....	78
Table 5.14 - ANSYS – Complete 2-axis model modal frequencies comparison .....	79
Table 6.1 - MATLAB Flutter Analysis, result comparison.....	87
Table 6.2 - ANSYS Flutter Analysis on Central Span Models, result comparison.....	93
Table 6.3 - ANSYS Flutter Analysis on Complete Models, result comparison.....	100
Table 6.4 - Flutter Analysis on different models, result comparison .....	101

## Chapter 1 - Introduction

Suspension bridges represent a pinnacle of modern engineering, blending aesthetic elegance with structural efficiency. Developed through centuries of innovation, these structures use flexible cables and lightweight materials to span vast distances and overcome obstacles like deep gorges and waterways. Their evolution reflects a persistent quest for engineering solutions that integrate safety, durability, and economic efficiency, making them the optimal choice for long spans, especially in areas where placing pillars is challenging.

In Table 1.1, the ten longest suspension bridges in the world are summarized.

Table 1.1 - List of longest suspension bridge spans[1]

Bridge	Main Span Length [m]	Location	Year opened
1915 Çanakkale Bridge	2023	Turkey	2022
Akashi Kaikyo Bridge	1991	Japan	1998
Yangsigang Yangtze River Bridge	1700	China	2019
Nansha Bridge	1688	China	2019
Shenzhen-Zhongshan Bridge	1666	China	2024
Xihoumen Bridge	1650	China	2009
Great Belt Bridge	1624	Denmark	1998
Ningyang Yangtze River Bridge	1560	China	2025
Osman Gazi Bridge	1550	Turkey	2016
Yi Sun-sin Bridge	1545	South Korea	2012

### 1.1 Structural characteristics of suspension bridges

The structural components of a suspension bridge include the deck-girder, main cables, towers, anchorages and hanger ropes [2].

The main girder is the longitudinal member of the deck that supports and distributes vertical live load, as vehicle, pedestrian and, in some cases, train traffic. The stiffening girder can either be a separate truss or consist of plate stiffening girders combined with lateral bracing systems, or it can be integrated into the deck structure as a shallow box girder with a low-drag shape to minimize wind loading. Its aerodynamic design is crucial to mitigate the effects of wind, avoiding phenomena such as flutter and vortex shedding.

The towers, generally constructed of steel or reinforced concrete, are the vertical intermediate structures that support the main cables and transfer the external loads to bridge foundations. Their height is designed according to the span of the bridge, ensuring that the cables maintain an optimal angle for load distribution. The towers must withstand enormous compressive loads and horizontal forces generated by wind or earthquakes. In recent decades, more aerodynamic designs and advanced composite materials have been introduced to improve strength and reduce weight.

An anchorage is generally a massive concrete block, which secures the main cables to the ground or solid structures, balancing the enormous tensile forces generated by the loads shared by the deck and the main cables. Furthermore, it acts as end supports of a bridge against movement in the horizontal direction. In recent years, the use of advanced materials and monitoring techniques has significantly improved the reliability of anchorages.

The suspension main cables, composed of thousands of twisted high-strength steel wires, support the traffic-carrying stiffening girder through hanger ropes and transfer loads by direct tension to towers and anchorages. As illustrated in Figure 1.1, axial forces dominate the stress scheme of a suspension bridge. These cables efficiently transmit vertical loads from the deck and evenly distribute the weight, thereby reducing the bridge's deadweight and enabling longer spans. Moreover, their flexibility enables them to adapt to dynamic stresses from traffic, wind, and earthquakes.

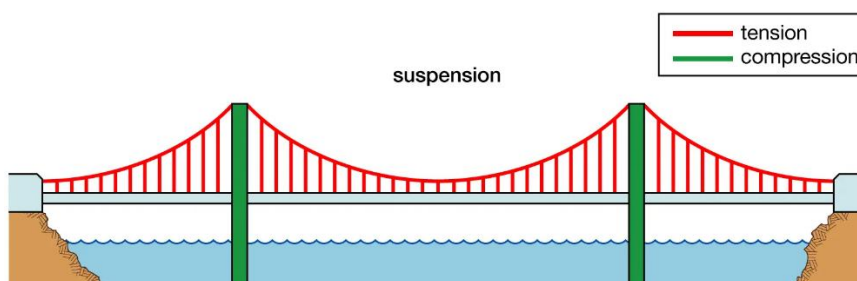


Figure 1.1 - Suspension bridge stress scheme [3]

Vertical suspenders (or hanger ropes) are the cables connecting the stiffening girder with the main cables, which are mainly used to transfer the live load applied on the deck to the main cable. Their arrangement follows a regular pattern to ensure the stability of the structure. Each hanger rope is designed to carry a specific load, considering dynamic fluctuations caused by traffic and weather conditions.

The structural components of a typical suspension bridge are shown in Figure 1.2.

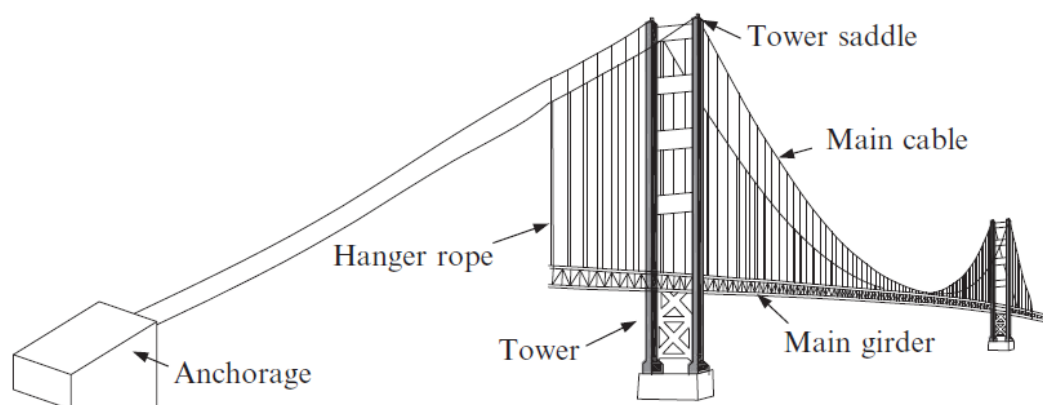


Figure 1.2 - Suspension bridge components[2]

## 1.2 History evolution and records

The evolution of suspension bridges is closely linked to the advancement of construction technologies and materials. From primitive rope structures to majestic modern works, the history of suspension bridges is a testimony to human engineering genius. This section analyses the main historical milestones and innovations that led to the current records. [3]

In the late 18th and early 19th century, British, French, American and other engineers faced serious problems of stability and resistance to wind forces and heavy loads, with the risk of collapse due to storms, heavy snowfall and large herds of cattle. The main credit for solving these problems goes to John Augustus Roebling, a German American engineer, who introduced mesh beams on the sides of the roadways. This innovation allowed the construction of extremely rigid structures, capable of crossing difficult places such as the Niagara Gorge, the Ohio to Cincinnati and, above all, the iconic Brooklyn Bridge connecting Brooklyn to Manhattan.

A further key development for modern suspension bridges was the pneumatic caisson, which made it possible to build pier foundations at great depths. This innovation permitted the designers to realize higher towers, and so consequently longer span length. This was initially adopted by French, British and American engineers, including Washington Roebling, who completed the Brooklyn Bridge begun by his father.

The first suspension bridge to exceed 1,000 metres in length was the George Washington Bridge (USA, 1931) with a main span of 1,067 metres [4].

In the 1930s, American engineers experimented with the use of a narrow solid girder instead of the web truss to stiffen the roadway. However, the collapse of the Tacoma Narrows Bridge in 1940 (Figure 1.3), caused by aerodynamic forces, led to a return to the use of the web truss. The bridge experienced dramatic wind-induced oscillations that escalated into destructive aeroelastic flutter due to the excessive slenderness of the deck along with a particularly

inefficient cross-section from an aerodynamic perspective. This collapse exposed critical flaws in aerodynamic design, reshaping future bridge engineering. In the aftermath, a new phase of suspension bridge design emerged, with a greater focus on understanding the aerodynamic phenomena resulting from the interaction between the deck and wind action.

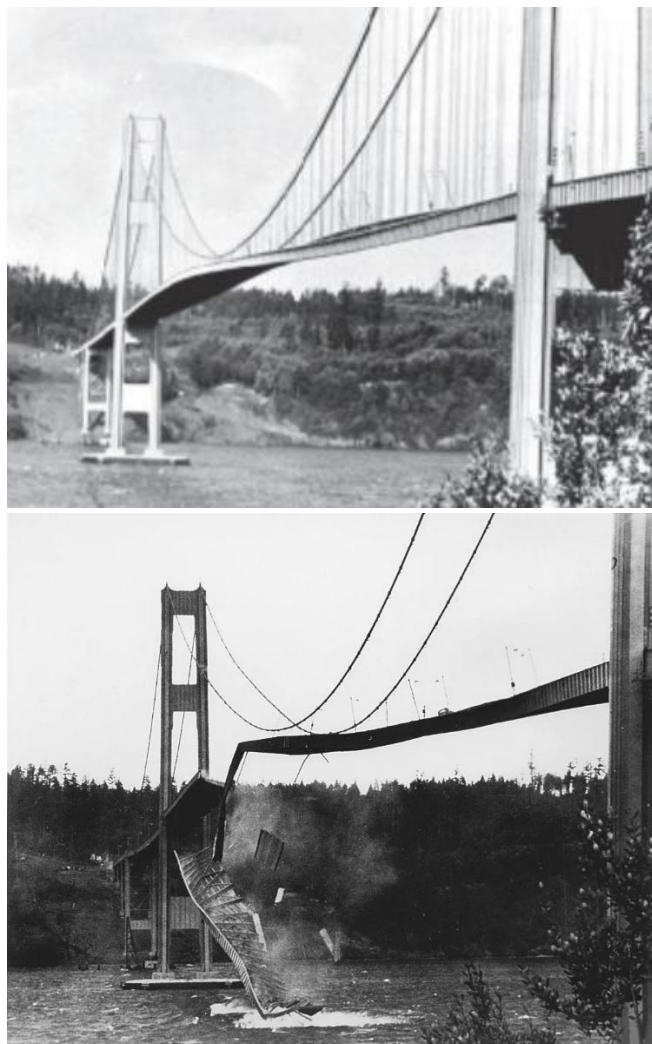


*Figure 1.3 – Collapse of the Tacoma Narrows Bridge*

During these years, Golden Gate Bridge (USA, 1937) was constructed. This bridge, with a main span of 1,280 metres, was for years the longest in the world. Its construction represented an unprecedented technical and logistical challenge and became a symbol of American engineering.

In the 1960s, the use of prefabricated cables in the workshop was introduced to reduce construction time.

Over the years, many suspension bridges were built, each breaking the previous records. Verrazzano-Narrows Bridge (USA, 1964), with a main span of 1,298 metres, held the world record for the longest span for more than a decade. Then, Humber Bridge (UK, 1981), with a main span of 1,410 metres, has been the longest suspension bridge in the world for 16 years, an icon of British engineering. Following the construction of Denmark's Great Belt Bridge in 1998



(with a main span of 1,624 meters), the record was only briefly surpassed before being reclaimed with the opening of the Akashi Kaikyō Bridge (Japan, 1998) [5]. This innovative structure, with a main span of 1,991 metres, was designed to withstand typhoons and earthquakes. It is a masterpiece of engineering and safety. Its construction required significant innovations, including ultra-strong steel main cables and a design based on advanced seismic analysis models. It held the world record for span length for all the two first decades of this millennium.

With the structural innovations and the discovery of modern steel alloys, modern suspension bridges are capable to cover greater spans.

In 2009, the Xihoumen Bridge opened with a main span of 1,650 m. Its innovative twin box-girder deck replaced the traditional truss system, playing a crucial role in enhancing the structure's aerodynamic stability. In line with this trend, in 2022, the multi-box girder 1915 Çanakkale Bridge [6] was inaugurated with a main span of 2,023 m, making it the longest suspension bridge in the world. It was designed to commemorate the centenary of the Republic of Turkey and stands as a remarkable blend of modern technology and historical significance.

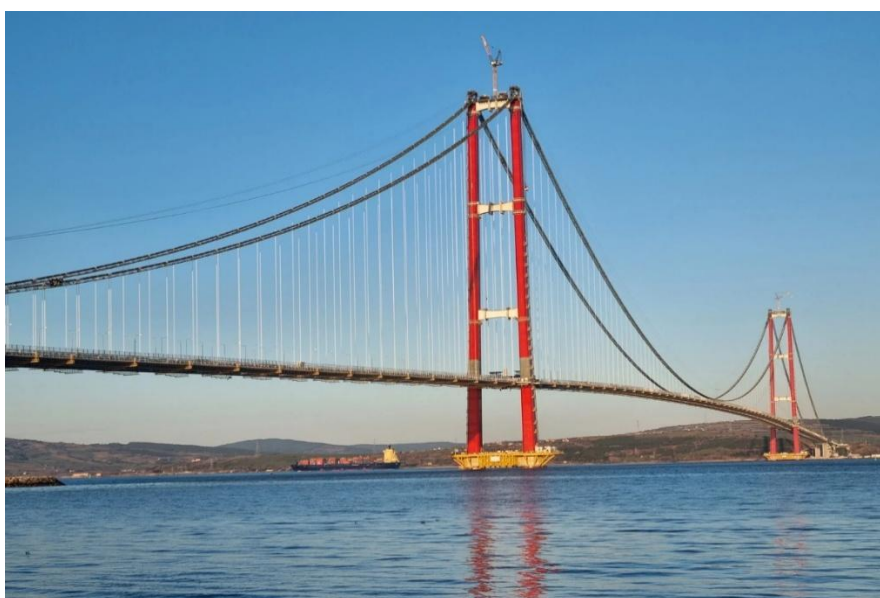


*Figure 1.4 - 1915 Çanakkale Bridge in Turkey [7]*

It is worth noting that nowadays many bridges are under construction. In particular two of these, in China, are going to break the 1915 Çanakkale Bridge's record.

The historical records of suspension bridges' span length are shown in Table 1.2, starting from the Brooklyn Bridge.

*Table 1.2 - Record breaking bridges built in the world*

<b>Bridge</b>	<b>Location</b>	<b>Year opened</b>	<b>Main Span Length [m]</b>
Brooklyn Bridge	New York, USA	1883	486
George Washington Bridge	New York, USA	1931	1067
Golden Gate Bridge	San Francisco, USA	1937	1280
Verrazzano Narrows Bridge	New York, USA	1964	1298
Humber Bridge	United Kingdom	1981	1410
Great Belt East Bridge	Denmark	1998	1624
Akashi Kaikyo Bridge	Japan	1998	1991
1915 Çanakkale Bridge	Turkey	2022	2023
Shiziyang Bridge	China	2028*	2180
Zhangjiagang-Jingjiang-Rugao Yangtze River Bridge (South Span)	China	2028*	2300
*(Under construction)			

Finally, it is relevant to also report the Bridge over the Straits of Messina (Italy, project) [8]. Although still in the planning stage, this bridge promises to be one of the longest and most ambitious suspension bridges in the world, with a planned span of approximately 3,300 metres. The complexity of the project stems from the seismic and climatic conditions of the area, which require state-of-the-art engineering solutions.

Today, suspension bridges represent a perfect combination of functionality, aesthetics and technological innovation. Their continuous development pushes the limits of engineering, opening up new possibilities for the future of global infrastructure.

## Chapter 2 - Notes on flutter instability of suspension bridges

Suspension bridges, due to their flexibility, are structures typically susceptible to wind-induced problems. Larger deck deformations are allowed by a change of configuration in the main cables. Therefore, generally suspension bridges are more flexible and prone to wind effects than cable-stayed bridges.[9]



Figure 2.1 - Suspension bridge scheme[9]

Wind may induce instability or excessive vibration in long-span bridges. Aeroelastic instability, caused by the interaction between airflow and an elastic structure, includes torsional divergence, galloping, and flutter. To ensure stability, the maximum expected wind speed at the site should remain lower than the critical value. On the other hand, wind-induced vibrations, such as vortex shedding and buffeting, are cyclic motions due to dynamic forcing and may cause fatigue or serviceability issues. Design requires analysing the structural response under dynamic loads to ensure reliability.

These instability and vibration phenomena may occur alone or in combination. Modern bridge design integrates computer analysis and wind tunnel testing. Computer models, whether analytical, semi-analytical, or numerical, require parameters typically obtained through experiments.

The interaction between bridge vibration and wind flow is usually idealized as consisting of two kinds of forces: motion dependent and motion independent. The former vanishes if the structures are rigidly constrained. The latter, being purely dependent on the wind characteristics and section geometry, exists whether or not the bridge is moving. According to this schematization, the equation of motion in the presence of the aerodynamic forces can be expressed in the following general form:

$$[M]\{\ddot{\delta}\} + [C]\{\dot{\delta}\} + [K]\{\delta\} = \{F(\delta, \dot{\delta})\}_{md} + \{F\}_{mi} \quad (2.1)$$

Where:

- $[M]$  is the mass matrix
- $[C]$  is the damping matrix

- $[K]$  is the stiffness matrix
- $\{\delta\}$  is the displacement vector
- $\{F(\delta, \dot{\delta})\}_{md}$  is the motion-dependent aerodynamic force vector
- $\{F\}_{mi}$  is the motion-independent wind force vector

While both motion-independent and motion-dependent forces cause deformation, aeroelastic instability is only due to the motion-dependent part. This is also responsible for the difference between short span and long-span bridges. For the former, the motion-dependent part is minor and there is less concern about aeroelastic instability. For the latter, however, both instability and vibration need to be carefully investigated. Aeroelastic phenomena are characterized by the peculiarity that the elastic structure and the air flow combine together to form a single dynamic system with proper features that differ from those of the two components taken separately.

## 2.1 Steady aerodynamic forces

Let us consider a static condition of the bridge with the application of plane forces in x and y directions, torque moment, generated by the wind flow approaching the deck in the horizontal direction transversal to the longitudinal axis.

Stability is evaluated with respect to the deformed shape of the deck under wind action and its instability.[9]

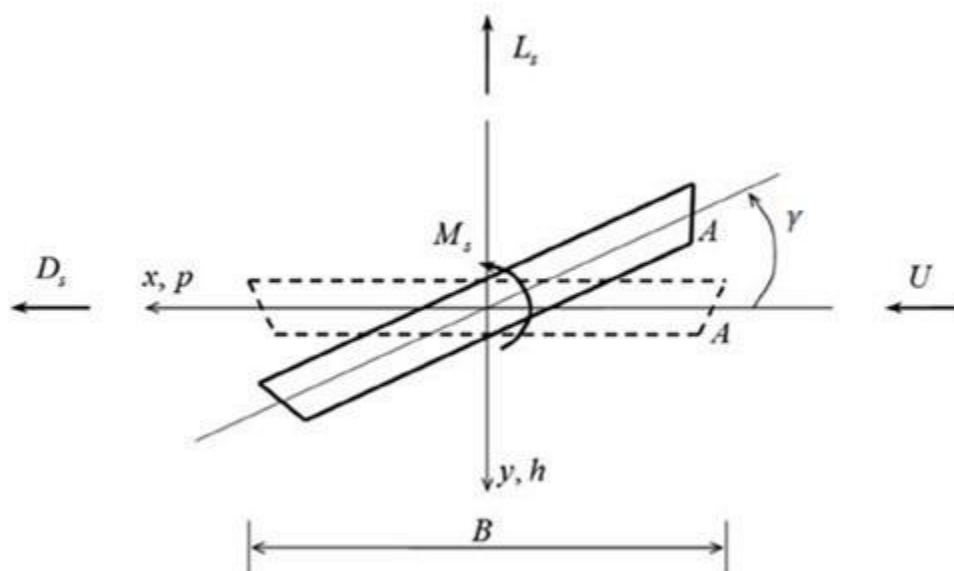


Figure 2.2 - Steady aerodynamic model[10]

According to the strip theory, for a unit span length, drag force in x direction, lift force in y direction and moment around z axis are expressed by the following equations:

$$D_S = \frac{1}{2} \rho U^2 B C_D(\gamma) \quad (2.2)$$

$$L_S = \frac{1}{2} \rho U^2 B C_L(\gamma) \quad (2.3)$$

$$M_S = \frac{1}{2} \rho U^2 B^2 C_M(\gamma) \quad (2.4)$$

Where:

- $\rho$  is the air density [ $\text{kg}/\text{m}^3$ ];
- $U$  is the average wind speed [ $\text{m}/\text{s}$ ];
- $B$  is the deck width [ $\text{m}$ ];
- $C_D(\gamma), C_L(\gamma), C_M(\gamma)$  are the non-dimensional static aerodynamic coefficients of drag, lift and moment that are dependent on the angle of attack of the wind  $\gamma$  [ $\text{deg}$ ];

The aerodynamic coefficients can be evaluated with a test in a scaled section in wind tunnel. In this way it is possible to control the wind forces and the angle of attack  $\gamma$ .

In Figure 2.3 there are examples of steady aerodynamic coefficients for different bridge deck's section.

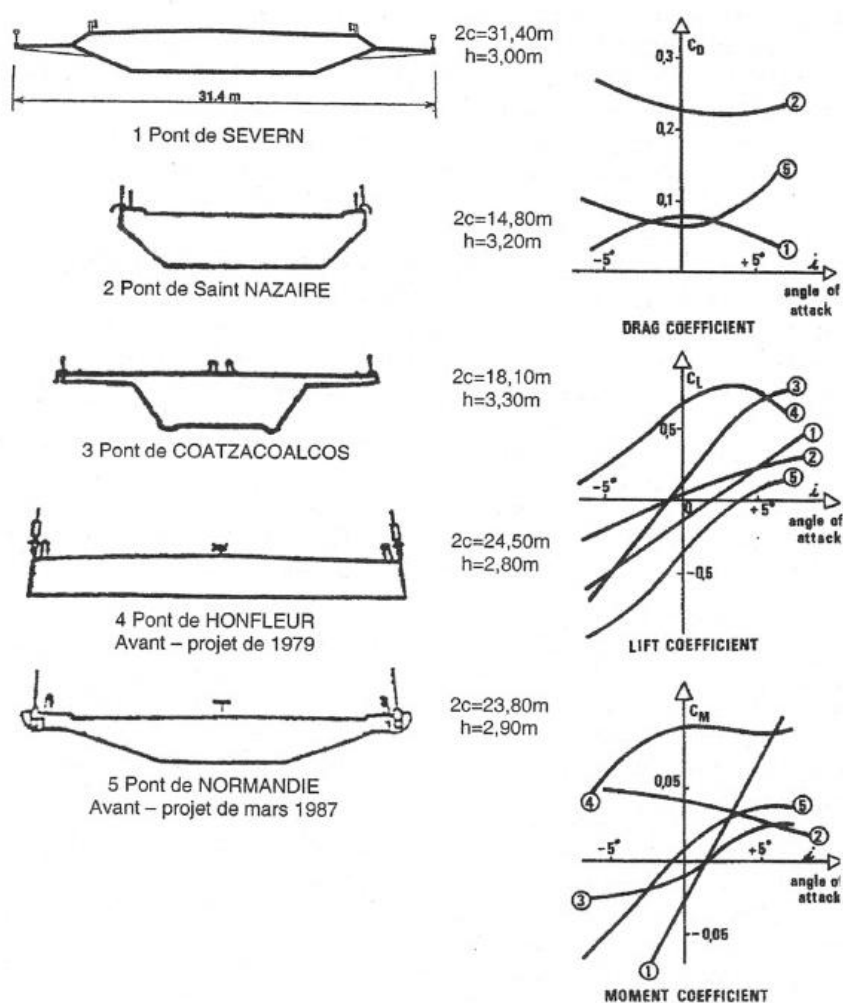


Figure 2.3 - Examples of aerodynamic coefficients [10]

The drag coefficient ( $C_D$ ) is always positive, generally having zero slope in the origin.  $C_L$  and  $C_M$  can attain positive, negative and nil values, as well as they can show both positive and negative slope. A negative slope in the lift coefficient ( $C_L$ ) indicates a tendency towards instability in the vertical motion (galloping), whereas a positive slope is stabilising. Conversely, a positive slope in the moment coefficient ( $C_M$ ) has a destabilizing effect in the torsion degree of freedom (torsional divergence); a negative slope has in this case a stabilising effect.

For a small values of  $\gamma$  the aerodynamic coefficients can be linearized around the null angle of attack and the Equations 2.2, 2.3 and 2.4 become:

$$D_S = \frac{1}{2} \rho U^2 B C_D(0) \quad (2.5)$$

$$L_S = \frac{1}{2} \rho U^2 B \left( C_L(0) + \left( \frac{dC_L}{d\gamma} \right) \gamma \right) \quad (2.6)$$

$$M_S = \frac{1}{2} \rho U^2 B^2 \left( C_M(0) + \left( \frac{dC_M}{d\gamma} \right) \gamma \right) \quad (2.7)$$

## 2.2 2-DoF flutter

Aeroelastic flutter is a dynamic instability phenomenon that originates from the mutual interaction of elastic, inertial and self-excited aerodynamic forces, which provides that at a certain wind speed the structure oscillates in a divergent, destructive manner.

If a system immersed in a wind flow is given a small perturbation, its motion will either decay or diverge, depending on whether the energy extracted from the flow is smaller or larger than the energy dissipated by mechanical damping. The critical condition that separates decay from divergent motions occurs at a wind speed known as the flutter speed. At this speed, the structure undergoes oscillations with a constant frequency, known as the flutter frequency, while the amplitude continuously increases.[9]

The analyses usually performed combines both experimental and analytical procedures. The analysis aims to determine the minimum wind speed that triggers instability in the proposed bridge deck configuration, ensuring it remains significantly higher than the meteorological wind speeds at the bridge site.

In a linear flutter analysis, only the onset instability condition is normally examined for the design of bridge structures. Under the assumption of small oscillations perturbing the flow, the structure can be modelled as a damped linear oscillator with two-degree-of-freedom:

$$m\ddot{h}(t) + c_h\dot{h}(t) + k_h h(t) = L_{se}(t, K) \quad (2.8)$$

$$I\ddot{\alpha}(t) + c_\alpha\dot{\alpha}(t) + k_\alpha\alpha(t) = M_{se}(t, K) \quad (2.9)$$

Where:

- $h$  and  $\alpha$  are the vertical bending and the torsional angle;

- $m$  and  $I$  are the mass and the polar mass moment of inertia per unit length;
- $c_h$  and  $c_\alpha$  are the mechanical damping coefficients;
- $k_h$  and  $k_\alpha$  are the stiffness in the heaving and pitching modes, respectively;

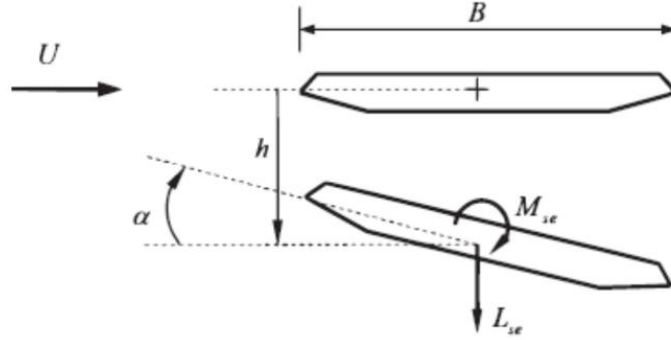


Figure 2.4 - 2-DoFs simplified model[9]

- $L_{se}$  and  $M_{se}$  are the self-excited lift and moment per unit length, depending on time  $t$  and on the deck oscillation through non-dimensional aeroelastic parameter  $K = \frac{\omega B}{U} = \frac{2\pi f B}{U}$ , called the reduced frequency of oscillation.
- $\omega$  is the angular frequency frequency of oscillation;
- $U$  is the undisturbed mean wind speed.

Figure 2.4 shows the self-excited aerodynamic forces acting on a deck which is subjected to a constant wind flow  $U$ , and in this two-degree-of-freedom simplified model only the vertical deflection  $h$  and the torsional rotation  $\alpha$  are considered.

A closed-form expression for the unsteady aerodynamic forces acting on oscillating bridge decks cannot be obtained. To solve the problem, Scanlan and Tomko [11] extended the solution developed by Theodorsen [12] for the thin airfoil to bridge sections, well explained in Section 4. They proposed a semiempirical model, in which the aerodynamic forces are expressed in terms of some unsteady coefficients, the so-called flutter (or aeroelastic) derivatives that are experimentally determined in the wind tunnel. According to Scanlan and Tomko, the self-excited forces can be assumed as linear functions of structural displacements and velocities, parametrically dependent on the reduced frequency of oscillation:

$$L_{se}(t, K) = \frac{1}{2} \rho U^2 B \left[ KH_1^*(K) \frac{\dot{h}(t)}{U} + KH_2^*(K) \frac{B\dot{\alpha}(t)}{U} + K^2 H_3^*(K) \alpha(t) + K^2 H_4^*(K) \frac{h(t)}{B} \right] \quad (2.10)$$

$$M_{se}(t, K) = \frac{1}{2} \rho U^2 B^2 \left[ KA_1^*(K) \frac{\dot{h}(t)}{U} + KA_2^*(K) \frac{B\dot{\alpha}(t)}{U} + K^2 A_3^*(K) \alpha(t) + K^2 A_4^*(K) \frac{h(t)}{B} \right] \quad (2.11)$$

Where:

- $H_i^*$  and  $A_i^*$  ( $i = 1 - 4$ ) are the flutter derivatives



Flutter derivatives are functions of the reduced frequency of oscillation  $K$ , as well as the mean angle of attack. The coefficients that multiply generalized displacements are intended as aerodynamic stiffness, while those which multiply generalized velocities represent aerodynamic damping. Equations 2.10 and 2.11 do not explicitly include additional mass terms in  $\ddot{h}$  and  $\ddot{\alpha}$ , which are considered to be negligible in wind engineering applications.

The flutter derivatives are usually plotted as a function of the reduced velocity:

$$U_r = \frac{U}{fB} = \frac{2\pi}{K} \tag{2.12}$$

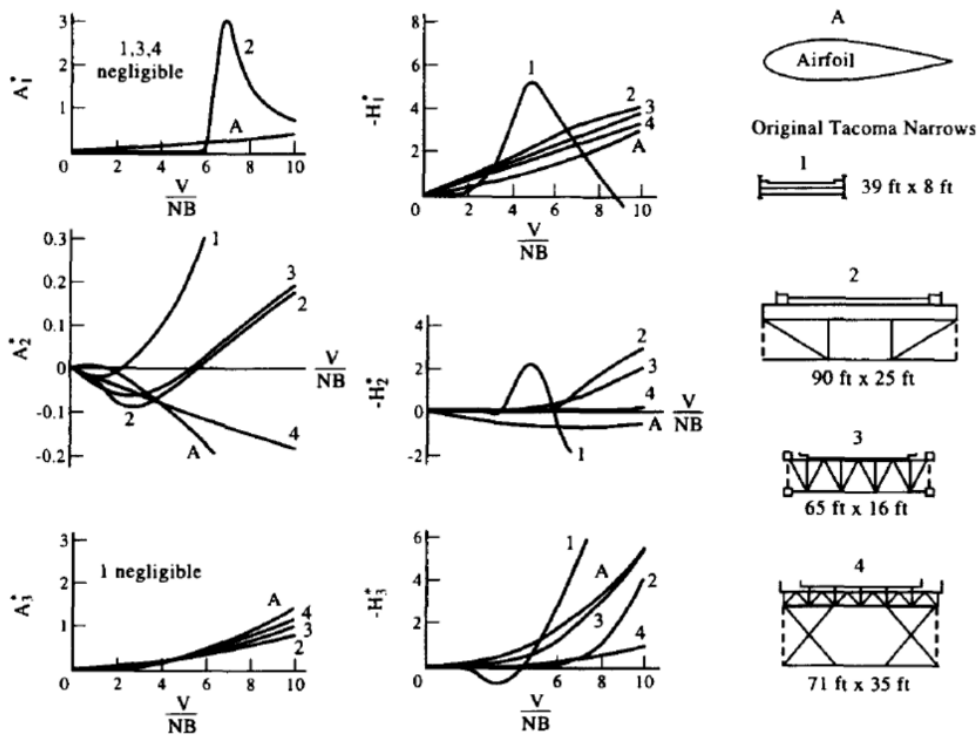


Figure 2.5 - Examples of flutter derivatives[9]

In classical flutter, also known as coupled or stiffness-driven flutter, the two modes coalesce into a single flutter frequency that originates a motion which introduces energy into the system, leading to divergent or large-amplitude oscillations.

Considering a harmonic solution to Equations 2.8 and 2.9 in the form [9]:

$$h(t) = h_0 e^{i\omega t} \tag{2.13}$$

$$\alpha(t) = \alpha_0 e^{i\omega t} \tag{2.14}$$

By separating the real and imaginary components, two polynomial equations of fourth and third degree in  $K$  are derived. Their common solution yields the reduced frequency  $K_F$ , to which the flutter frequency  $\omega_F$  is associated.

Consequently, the flutter instability speed can be determined as follows:



$$U_F = \frac{B\omega_F}{K_F} \quad (2.15)$$

If more than one intersection point is found in the selected range of  $K$ , the lowest  $U_F$  is the required solution.

Alternatively, the flutter speed can be calculated with the eigenvalues  $\omega_n = \omega_{r,n} + i\omega_{i,n}$  ( $n = 1, 2, 3, \dots$ ) of the system, by increasing the wind speed until the imaginary part of an eigenvalue, which is related to damping, reaches a negative value. The real part of the same eigenvalue represents the flutter frequency.

### 2.3 3-DoF flutter

Although the simplified representation of the bridge deck response with only two degrees of freedom provides excellent results, in very long-span bridges, which are more flexible, the lateral (sway) component of motion cannot be neglected and may play a significant role in flutter instability.[9]

Figure 2.6 shows the self-excited aerodynamic forces acting on a deck which is subjected to a constant wind flow  $U$ . In this three-degree-of-freedom simplified model, also the lateral deflection  $p$  and the self-excited drag  $D_{se}$  are considered, differently from Section 2.2.

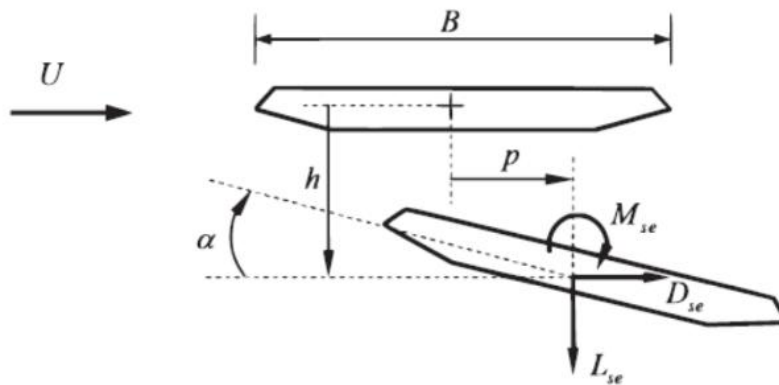


Figure 2.6 - 3-DoFs simplified model[9]

Considering also the along-wind force and displacement, the general expression of the self-excited forces written in matrix form is:

$$\begin{aligned}
\begin{Bmatrix} L_{se} \\ D_{se} \\ M_{se} \end{Bmatrix} &= \frac{1}{2} \rho U^2 B \begin{pmatrix} \frac{K^2 H_4^*}{B} & \frac{K^2 H_6^*}{B} & K^2 H_3^* \\ \frac{K^2 P_6^*}{B} & \frac{K^2 P_4^*}{B} & K^2 P_3^* \\ \frac{K^2 A_4^*}{B} & \frac{K^2 A_6^*}{B} & K^2 A_3^* B \end{pmatrix} \begin{Bmatrix} h \\ p \\ \alpha \end{Bmatrix} + \begin{pmatrix} \frac{KH_1^*}{U} & \frac{KH_5^*}{U} & \frac{KH_2^* B}{U} \\ \frac{KP_5^*}{U} & \frac{KP_1^*}{U} & \frac{KP_2^* B}{U} \\ \frac{KA_1^* B}{U} & \frac{KA_5^* B}{U} & \frac{KA_2^* B^2}{U} \end{pmatrix} \begin{Bmatrix} \dot{h} \\ \dot{p} \\ \dot{\alpha} \end{Bmatrix} \\
&= \frac{1}{2} \rho U^2 B ([F_d] \{q\}) + \frac{1}{U} [F_v] \{\dot{q}\} \quad (2.16)
\end{aligned}$$

Where:

- $L_{se}$ ,  $D_{se}$  and  $M_{se}$  are the self-excited lift force, drag force and pitch moment, respectively;
- $h$ ,  $p$  and  $\alpha$  are the displacements at the centre of the deck section in the directions corresponding to  $L_{se}$ ,  $D_{se}$  and  $M_{se}$ , respectively;
- $H_i^*$ ,  $P_i^*$  and  $A_i^*$  ( $i = 1 - 6$ ) are the generalized derivatives;
- $[F_d]$  and  $[F_v]$  are the aeroelastic stiffness and damping matrices. Namely flutter derivatives matrices corresponding to displacement and velocity, respectively.

In liner analysis, the general aeroelastic motion equations of bridge system are expressed in terms of the generalized modal coordinate vector  $\{\delta\}$ :

$$[M] \{\ddot{\delta}\} + \left( [C] - \frac{1}{2} \rho U^2 B [C^*] \right) \{\dot{\delta}\} + \left( [K] - \frac{1}{2} \rho U^2 B [K^*] \right) \{\delta\} = \{0\} \quad (2.17)$$

Where  $[M]$ ,  $[C]$  and  $[K]$  are the generalized mass, damping and stiffness matrices, respectively;  $[C^*]$  and  $[K^*]$  are the generalized aerodynamic damping and aerodynamic stiffness matrices, respectively.

Matrices  $[M]$ ,  $[C]$  and  $[K]$  are derived in the same way as in the classical dynamic analysis, while matrices  $[C^*]$  and  $[K^*]$ , corresponding to  $[F_v]$  and  $[F_d]$  in Equation 2.16, respectively, are assembled from local aerodynamic forces.

By assuming harmonic oscillation in the form  $\{\delta\} = \{\delta_0\} e^{i\omega t}$ , the following characteristic problem is obtained:

$$\left( -\omega^2 [M] + i\omega \left( [C] - \frac{1}{2} \rho U^2 B [C^*] \right) + [K] - \frac{1}{2} \rho U^2 B [K^*] \right) \{\delta_0\} = \{0\} \quad (2.18)$$

The flutter speed  $U_F$  and the flutter frequency  $\omega_F$  can be derived from the nontrivial solution of Equation 2.18, which is given by the following condition:

$$\det \left( -\omega^2 [M] + i\omega \left( [C] - \frac{1}{2} \rho U^2 B [C^*] \right) + [K] - \frac{1}{2} \rho U^2 B [K^*] \right) = 0 \quad (2.19)$$

## 2.4 Flutter Analysis in MATLAB

A multi-order aeroelastic analysis, incorporating aerostatic nonlinearities, is performed on a one-dimensional continuum model of the suspension bridge using an analytical code implemented in MATLAB.

$$\begin{aligned} \mu_g \frac{\partial^2 v(z, t)}{\partial t^2} + c_v \frac{\partial v(z, t)}{\partial t} + EI_x \frac{\partial^4 v(z, t)}{\partial z^4} - H \frac{\partial^2 v(z, t)}{\partial z^2} + \frac{\partial^2 (m_y(z) \vartheta(z, t))}{\partial z^2} \\ + \left( \frac{8f}{l} \right)^2 \frac{E_c A_c}{L_c} \int_0^l v(z, t) dz = L_{se} \end{aligned} \quad (2.20)$$

$$\begin{aligned} I_\vartheta \frac{\partial^2 \vartheta(z, t)}{\partial t^2} + c_\vartheta \frac{\partial \vartheta(z, t)}{\partial t} + EI_\omega \frac{\partial^4 \vartheta(z, t)}{\partial z^4} - (GI_t + Hb^2) \frac{\partial^2 \vartheta(z, t)}{\partial z^2} + m_y(z) \frac{\partial^2 v(z, t)}{\partial z^2} \\ + b^2 \left( \frac{8f}{l} \right)^2 \frac{E_c A_c}{L_c} \int_0^l \vartheta(z, t) dz = M_{se} \end{aligned} \quad (2.21)$$

Where:

- $v$  and  $\vartheta$  are the vertical and torsional displacement of the deck cross-section;
- $\mu_g$  and  $I_\vartheta$  are the bridge mass and mass moment of inertia per unit length;
- $c_v = 2\mu_g \xi_v \omega_v$  and  $c_\vartheta = 2I_\vartheta \xi_\vartheta \omega_\vartheta$  are damping coefficients, being  $\xi_v$ ,  $\xi_\vartheta$  damping ratios and  $\omega_v$ ,  $\omega_\vartheta$  angular frequencies;
- $EI_x$ ,  $EI_\omega$  and  $GI_t$  respectively the vertical bending rigidity, warping and primary torsional rigidity;
- $H$  is the horizontal component of the main cables tension;  $l$  is the main span length;  $b$  is half the distance between cables;
- $f$ ,  $A_c$ ,  $L_c$  and  $E_c$  are the sag, cross-section area, length and Young's modulus of the main cable;
- $L_{se}$ ,  $M_{se}$  are the aeroelastic self-excited lift and moment;
- $m_y(z)$  is the horizontal bending moment due to the steady drag force.

Equations 2.20 and 2.21, which are based on classical linearized theory but are improved by including wind-related geometric nonlinearities, such as stiffening/softening caused by the lift force and a second-order Prandtl-like effect caused by the drag force, govern the vertical and torsional oscillations of a suspension bridge subjected to aeroelastic loads. In [13], this procedure was first implemented.

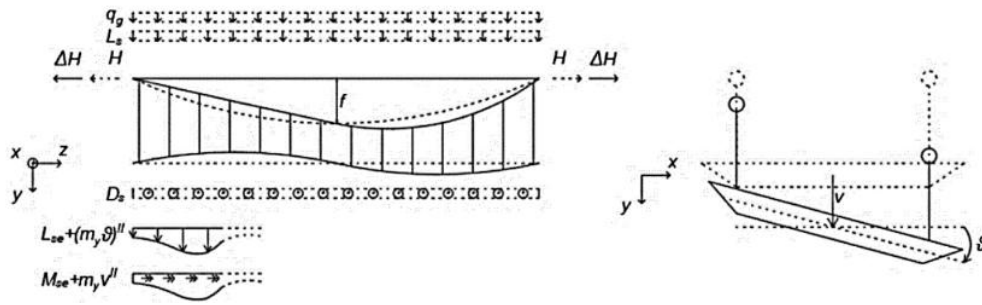


Figure 2.7 - Perturbed configuration of 1D continuum model[14]

Differential Equations (2.20 and 2.21) account for aeroelastic nonlinearities. These equations state that the projection of the horizontal bending moment in the perturbed configuration results in additional (2nd order) terms that have geometric nonlinearities and affect the vertical and torsional equilibrium (Figure 2.7). Analysing the multimodal framework [14], the solution of differential equations can be considered in harmonic form.

$$v(z, t) = \bar{v}(z)e^{\lambda t}; \vartheta(z, t) = \bar{\vartheta}(z)e^{\lambda t} \quad (2.22)$$

Weighted sums of sinusoids with varying wavelengths are used to represent the spatial functions:

$$\bar{v}(z) = b \sum_{j=1}^n a_{v_j} \sin\left(\frac{j\pi z}{l}\right) \quad (2.23)$$

$$\bar{\vartheta}(z) = \sum_{k=1}^m a_{\vartheta_k} \sin\left(\frac{k\pi z}{l}\right) \quad (2.24)$$

By applying the Galerkin discretization method, an algebraic problem of dimension  $N = n + m$  for the unknowns  $a_{v_j}$  and  $a_{\vartheta_k}$  is obtained from the differential problem of equations 2.20 and 2.21:

$$[A(\lambda, U)]\{a_{v, \vartheta}\} = \{0\} \quad (2.25)$$

The search for nontrivial solutions leads to a quadratic eigenvalue problem.

The eigenvalues and eigenvectors of the quadratic eigenvalue problem with the notation  $r \in [1; 2N]$  are the eigenvalues  $\lambda_r$  and eigenvectors  $\{a_{v, \vartheta}\}_r$  identifying various vibration modes. When the  $2N$  independent eigensolutions are combined linearly, the solution of Equation 2.25 can be written as follows:

$$V(x, t) = \sum_{r=1}^{2N} v_r(z)e^{\lambda_r t} \quad (2.26)$$

$$T(x, t) = \sum_{r=1}^{2N} \vartheta_r(z)e^{\lambda_r t} \quad (2.27)$$

where, for each of the different eigenvectors, Equations 2.26 and 2.27 are used to calculate the vertical and torsional components ( $v_r(z)$  and  $\vartheta_r(z)$ , respectively) of the  $r^{th}$  eigen-solution. It is also possible to write the corresponding eigenvector components in polar form by defining the pair of complex conjugate eigenvalues as  $\lambda_r = \mu_r + i\omega_r$ .

The vertical and torsional displacements are expressed as the sum of  $r$  modal contributions, each defined by the sum of  $N = n + m$  harmonic functions. The imaginary part of the eigenvalues represents the modal frequency, while the real part determines the exponential behaviour of the modal contributions. The system becomes unstable, diverging exponentially over time, if the real part of an eigenvalue is positive.

Iterative complex eigenvalue analyses are performed at each wind speed increment to evaluate changes in natural frequencies and modal shapes. Instability occurs when the real part of an eigenvalue reaches zero, with the corresponding wind speed identified as the critical velocity.

## 2.5 Flutter analysis in ANSYS

The researchers X.G. Hua and Z.Q. Chen [15] [16] proposed a method that allows to perform a flutter analysis using commercial finite element package ANSYS. The method defines the aeroelastic loads using a custom user-defined element, as briefly described in what follows.

The equation of motion for a deck section in the smooth flow can be expressed as:

$$M\ddot{X} + C\dot{X} + KX = F_{ae} \quad (2.28)$$

Where  $M$ ,  $K$  and  $C$  are the global mass, stiffness and damping matrices, respectively;  $\ddot{X}$ ,  $\dot{X}$  and  $X$  represent the nodal acceleration, velocity and displacement vectors, respectively; and  $F_{ae}$  denotes the vector containing the assembled self-excited forces ( $L_{se}$ ,  $D_{se}$  and  $M_{se}$ ) defined in Equations 2.16 and represented in Figure 2.6.

By converting the distributed aeroelastic forces of a generic element  $e$  of bridge girder into equivalent nodal loads acting on member ends, one obtains the equivalent nodal loadings for that element as:

$$F_{ae}^e = K_{ae}^e X^e + C_{ae}^e \dot{X}^e \quad (2.29)$$

Where  $K_{ae}^e$  and  $C_{ae}^e$  are the aeroelastic stiffness and damping matrices for element  $e$ , respectively. Using a lumped formulation, they can be expressed as:

$$K_{ae}^e = \begin{bmatrix} K_{ae1}^e & 0 \\ 0 & K_{ae1}^e \end{bmatrix} \quad (2.30)$$

$$C_{ae}^e = \begin{bmatrix} C_{ae1}^e & 0 \\ 0 & C_{ae1}^e \end{bmatrix} \quad (2.31)$$

$$K_{ae1}^e = a \begin{bmatrix} 0 & 0 & 0 & 0 & 0 & 0 \\ 0 & P_4^* & P_6^* & BP_3^* & 0 & 0 \\ 0 & H_6^* & H_4^* & BH_3^* & 0 & 0 \\ 0 & BA_6^* & BA_4^* & B^2A_3^* & 0 & 0 \\ 0 & 0 & 0 & 0 & 0 & 0 \\ 0 & 0 & 0 & 0 & 0 & 0 \end{bmatrix} \quad (2.32)$$

$$C_{ae1}^e = b \begin{bmatrix} 0 & 0 & 0 & 0 & 0 & 0 \\ 0 & P_1^* & P_5^* & BP_2^* & 0 & 0 \\ 0 & H_5^* & H_1^* & BH_2^* & 0 & 0 \\ 0 & BA_5^* & BA_1^* & B^2A_2^* & 0 & 0 \\ 0 & 0 & 0 & 0 & 0 & 0 \\ 0 & 0 & 0 & 0 & 0 & 0 \end{bmatrix} \quad (2.33)$$

Where  $a = \rho U^2 K^2 L_e / 2$  and  $b = \rho U B K L_e$  and  $L_e$  is the length of the element  $e$ .

Hence it is necessary to represent the elemental stiffness and damping matrices due to motion-dependent aeroelastic forces by element MATRIX27. The user-defined element in ANSYS, MATRIX27, is designed to model either an aeroelastic stiffness matrix or an aeroelastic damping matrix, but not both simultaneously. Consequently, a pair of MATRIX27 elements is assigned to each node of a generic bridge deck element, as illustrated in Figure 2.8.

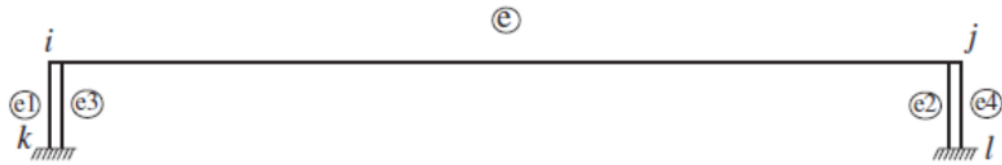


Figure 2.8 - Hybrid finite element model for flutter analysis in ANSYS[4]

The MATRIX27 elements  $e1$  and  $e3$  represent respectively the aeroelastic stiffness and damping of the node  $i$ , as the MATRIX27 elements  $e2$  and  $e4$  represent respectively the aeroelastic stiffness and damping of the node  $j$ . If the length of each bridge deck element is the same, the element matrices are simplified as:

$$K^{e1} = 2K_{ae}^e \quad (2.34)$$

$$C^{e3} = 2C_{ae}^e \quad (2.35)$$

$$K^{e2} = 2K_{ae}^e \quad (2.36)$$

$$C^{e4} = 2C_{ae}^e \quad (2.37)$$

Assembling all elemental matrices into global aeroelastic stiffness and damping matrices leads to:

$$F_{ae} = K_{ae}X + C_{ae}\dot{X} \quad (2.38)$$

Substituting Equation 2.38 in Equation 2.28, the mathematical model of an integrated system is obtained, with the effect of aeroelasticity parametrized by wind velocity and vibration frequency:

$$M\ddot{X} + (C - C_{ae})\dot{X} + (K - K_{ae})X = 0 \quad (2.39)$$

With this equation, complex eigenvalue analysis can be carried out to determine the eigenvalues of the system at specific wind velocity and vibration frequency.

Assuming the conjugate pairs of complex eigenvalues  $\lambda_j = \sigma_j \pm i\omega_j$  and the conjugate pairs of complex eigenvectors  $\phi_j = p_j \pm iq_j$ , the system will be dynamically unstable if the real part of any eigenvalue become positive. Therefore, the condition for the onset of flutter instability is expressed as follows: at a specific wind velocity  $U_f$ , the system exhibits a single eigenvalue  $\lambda_f$  with a real part equal to zero. The corresponding wind velocity  $U_f$  is then considered the critical flutter one, while the imaginary part  $\omega_j$  of the complex eigenvalue  $\lambda_f$  represents the flutter frequency.[6]

It is necessary to provide the variation of both wind velocity and vibration frequency in the complex eigenvalue analysis, so a mode-by-mode tracking method is employed to iteratively search the flutter frequency and the flutter velocity. The procedure is summarized in the following steps [16]:

1. Establish the Finite Element model for the original structure without MATRIX27 elements, perform a modal analysis including the effect of permanent loads computing the natural frequency of the investigated branch  $\omega_i^0$ .
2. Determine the present wind velocity  $U$ .
3. Let the initial oscillation frequency  $\omega_0$  be the frequency  $\omega_i^0$  of the selected natural frequency.
4. Determine the reduced frequency  $K$  and the aeroelastic stiffness and damping matrices in MATRIX27 elements in Equations 2.30, 2.31, 2.32 and 2.33 at the present iteration, and then carry out the complex eigenvalues analysis.
5. Compare the imaginary part of the  $i^{th}$  computed complex eigenvalue  $\lambda_i$  with  $\omega_0$ . If  $|(Im(\lambda_i) - \omega_0)/Im(\lambda_i)| > 10^{-3}$  let  $\omega_0 = Im(\lambda_i)$  and repeat step 4 and 5, otherwise go to step 6.
6. Loop steps 3-5 for the selected natural mode to obtain a complex eigenvalue such that  $|(Im(\lambda_i) - \omega_0)/Im(\lambda_i)| < 10^{-3}$  at the present wind velocity  $U$ .
7. Repeat steps 2-6 for the range of interest of wind velocity in order to obtain the variation of the pairs of complex eigenvalues with wind velocity.
8. Repeat steps 1-7 mode by mode.



## Chapter 3 - Description of the case study: Xihoumen Bridge

### 3.1 General bridge outline

The Zhoushan Xihoumen Bridge, which is located in Zhoushan, in the Zhejiang Province of China, is the fourth mega-scale bridge of the Zhoushan Archipelago-to-Mainland Linking Project with a length up to 50 km. The bridge connects the Cezi and Jintang Islands across the Xihoumen waterway with deep waters and rapid currents. (Figure 3.1).



Figure 3.1 - Zhoushan Archipelago and mainland linking project[17]

It was designed as a two-span continuous steel-box girder suspension bridge with a 1650 m long main span, which is the sixth longest main span in the world and the fourth in China currently. This bridge was also claimed to be the longest box girder suspension bridge in the world until the construction of the 1915 Çanakkale Bridge in Turkey. The total length of the bridge is 2713 m, considering the two lateral spans of 578 m and 485 m. (Figure 3.2)

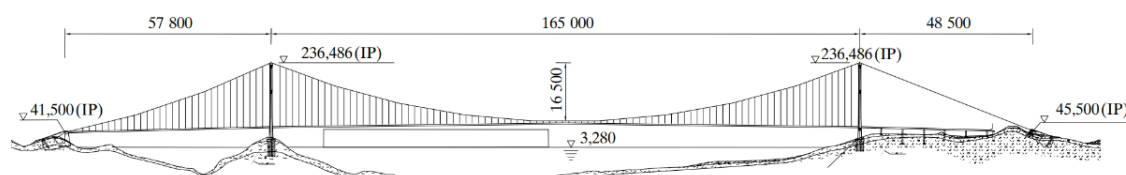


Figure 3.2 - Span arrangement of the Xihoumen Bridge (Units: cm)[17]





Figure 3.3 – Overview of the Xihoumen Bridge[18]

### 3.1.1 Suspended deck with twin box-girders

Based on the experience gained from the Runyang Bridge (1490 m span length) with a flutter speed of 51 m/s and the Great Belt Bridge (1624 m span length) with a flutter speed of 65 m/s, the 1650 m span length of the Xihoumen Bridge may pose challenges related to aeroelastic and aerodynamic instability, especially considering the stricter stability requirement of 78.4 m/s. A streamlined twin-box girder was adopted, measuring 36 m in total width (from end to end) and 3.5 m in height. The central slot between the two enclosed steel boxes is 6 m wide.

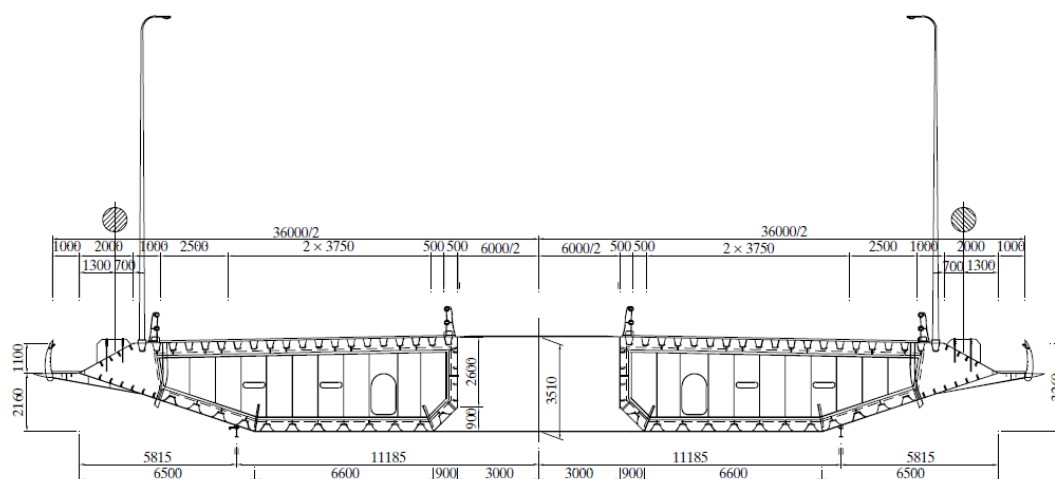


Figure 3.4 - Typical cross section of the twin-box girder (Units: mm)[17]

The two boxes are connected by a box-section beam and an I-shaped beam at intervals of 18 m, corresponding to the spacing of the bridge hangers. The box beam is 3.51 m deep and 3.6 m

wide, while the I-shaped beam is 3.51 m high with flange widths of 0.34 m. Each enclosed steel box is 14 m wide, with plate-type diaphragms placed inside at vertical intervals of 3.6 m. The twin-box girder utilizes orthotropic steel structures, with top plate thicknesses of 14 mm and 16 mm and bottom plate thicknesses of 10 mm and 14 mm. The standard segment length of the stiffened box girder is 18 m, with one box beam and one I-beam provided within each standard segment.[17]



*Figure 3.5 - Particular of the twin-box girder deck[18]*

This is the first time that a twin-box girder is adopted in a long-span suspension bridge for the purpose of wind resistance, in particular for aerodynamic flutter stability.[17]

### **3.1.2 External constraints and expansion joints**

Vertical constraints are implemented at both the north anchor and the crossbeam of the south pylon, with each consists of two bearings allowing horizontal movement. Lateral wind resistance bearings are installed at the north anchor, north pylon, and south pylon (one pair at each site). At the north anchor and south pylon, these bearings are symmetrically arranged along the bridge's centreline, whereas at the north pylon the bearings are placed on the pylon legs on both sides of the stiffened box girder. Additionally, vertical viscous dampers are mounted at the north anchorage and the crossbeam of the south pylon, with two dampers provided at each location.

At both ends of the stiffened box girder, a large movement device accommodates significant displacement and rotation, with expansion capacities of 2160 mm at the north anchor and 2240 mm at the south pylon. [17]

### 3.1.3 Suspension system

#### 3.1.3.1 Main cable

The bridge has two main cables, and each cable is made of high-strength galvanized Prefabricated Parallel Wire Strands (PPWS) with a tensile strength of 1770 MPa. Each strand consists of 127 steel wires. The protection of the main cable is ensured by 4 mm galvanized winding wire and corrosion-protection coating.

The diameter of the main cable in the central span, north side span, and south side span is 0.845 m, 0.860 m, and 0.850 m, respectively. (Figure 3.6)[17]

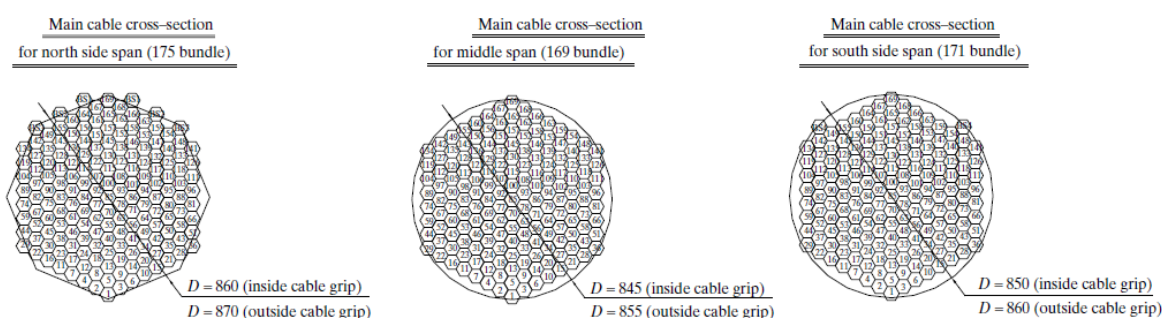


Figure 3.6 - Cross section of the main cable[17]

#### 3.1.3.2 Hangers

The bridge features steel wire rope hangers, each consisting of two cables. The suspension cable and cable grip are connected in a straddle configuration, with a pin-hinged connection to the steel box girder. The pin hinge joint incorporates self-lubricating bearings. The stiffened box girder has  $119 \times 2$  hanging points (lifting points). (Figure 3.7)



Figure 3.7 - Dynamic positioning of carrying boat[19]

The Xihoumen Bridge has a total of 238 vertical hangers, with the length varying from 2.5 to 169 m, and the uniform distance between the two neighbouring hangers is 18 m. The diameter of the cables of the 12 hangers near the pylon is 88 mm, and the rest is 60 mm. The centre-to-centre spacing of the cables of a hanger is 300 mm in the longitudinal direction of the bridge and 600 mm in the transverse direction.[20]



*Figure 3.8 - View of hangers and the north pylon[21]*

### 3.1.4 Towers

The high pylons of the Xihoumen Bridge are a reinforcing concrete frame structure composed of two columns and different crossbeams.



*Figure 3.9 - View of south pylon[18]*

The pylon height is 211.286 m. The north pylon has two crossbeams, one at the top and one at mid-height. The south pylon features an additional crossbeam to accommodate various constraint devices for the stiffening girder. This additional crossbeam is necessary because the southern tower serves as the transition point between the main bridge, which has a suspended deck, and the approach bridge, designed as a continuous beam bridge.





*Figure 3.10 - Particular of cross beam of south pylon[18]*

The bridge pylons are reinforced concrete portal frame structures. Above the top transverse beam, the pylon legs incline inward, while their external side lines exhibit a double inclination. This design increases the conicity of the pylon legs below the deck, enhancing both structural efficiency and aesthetic appeal.

The pylon legs have a rectangular reinforced concrete cross-section, with dimensions varying from  $8.5 \times 6.5$  m at the top to  $12 \times 11$  m at the base. To mitigate Vortex-Induced Vibrations (see Section 3.2.3) and improve the visual appearance of the cable pylons, all four corners of the pylon leg cross-section are chamfered by  $700 \times 700$  mm. The crossbeam is a prestressed concrete structure with a rectangular cross-section.[17][19]

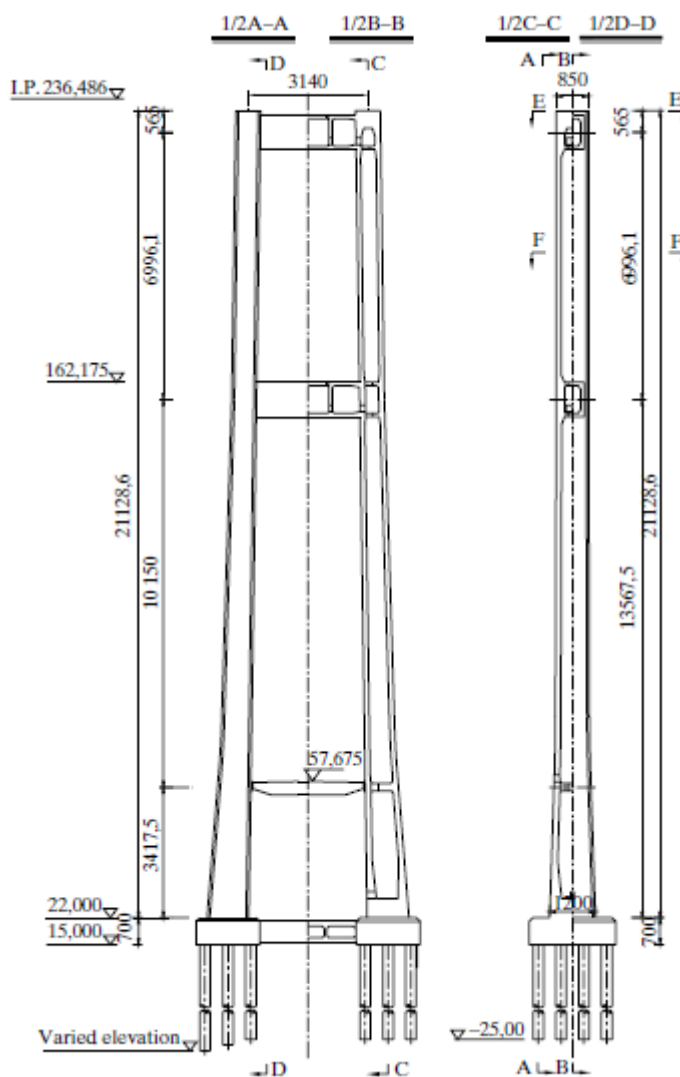


Figure 3.11 - Arrangement of north pylon (Dimension in cm)[17]

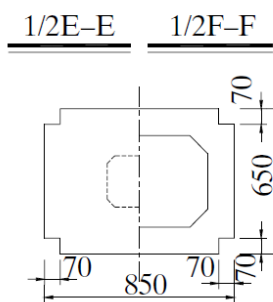


Figure 3.12 - Plan and section of pylon leg[17]

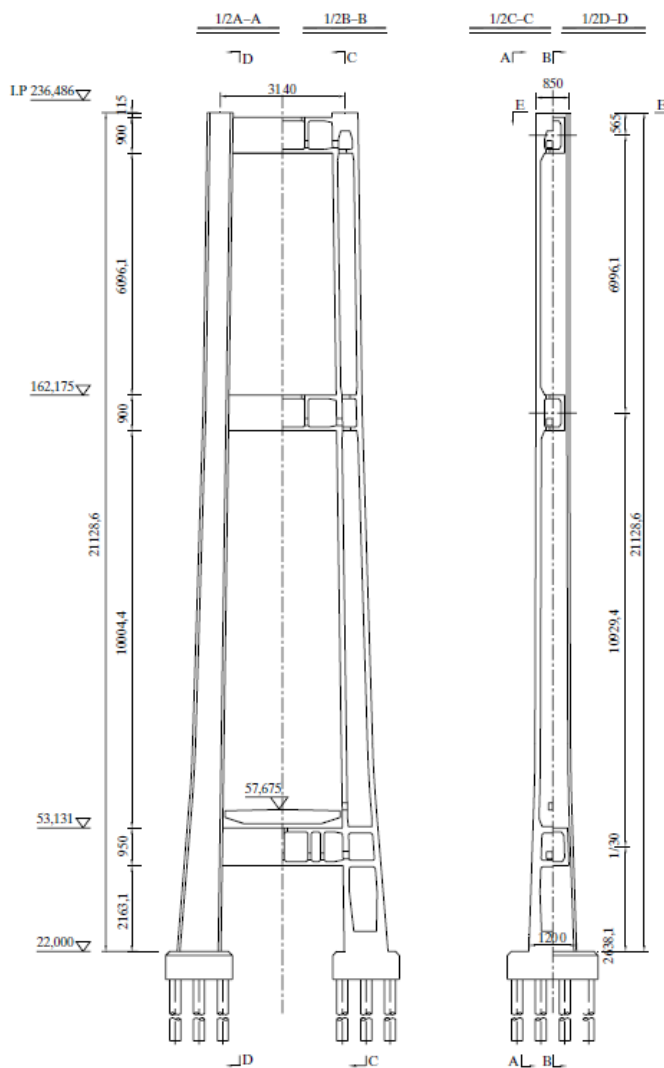


Figure 3.13 - Arrangement of south pylon[17]

### 3.1.5 Foundations

A pile group foundation is utilized, consisting of 12 piles with a 2.8 m diameter beneath each cable pylon leg. These piles are embedded in a slightly weathered rock layer. The pile cap dimensions are 22.8 m x 16.8 m x 7 m. A 10 m x 6 m crossbeam is placed between the two pile caps of the north pylon.[19]



## 3.2 Review of literature results for modal and flutter analysis

The Xihoumen Bridge, having been the longest multiple deck suspension bridge in the world for years, has attracted considerable interest from the scientific and engineering community. Numerous studies have been conducted to analyse its dynamic behaviour, with particular focus on modal response and aeroelastic phenomena, given the complexity of its multi-box girder structure.

The research available in the literature includes both experimental and numerical analyses, often based on wind tunnel models or advanced FEM simulations. In particular, the effects of deck configuration on aeroelastic stability have been explored, with investigations of flutter derivatives and critical values of flutter velocity and frequency.

The articles presented below have been the subject not only of an in-depth literature review but also of a comparison with the results obtained and presented in Chapters 5 and 6.

### 3.2.1 Yu *et al.* studies

In this study [22], the aeroelastic performance of the Xihoumen Bridge was investigated through both wind tunnel tests and analytical methods. The experimental campaign included a scaled aeroelastic model of the entire bridge (1:124 scale) and two simplified section models (1:40 and 1:60 scale). From these tests, the so-called “flutter derivatives” of the bridge decks were obtained, which are essential for evaluating wind-induced responses.

A three-dimensional finite element model was developed to support the analyses. In this model, the main beam was idealized as a single-girder structure, while the towers were represented by space beam elements. The main cables were modelled using hanger bar elements, accounting for geometric stiffness due to axial forces. Each joint in the model had six degrees of freedom (three translational and three rotational) and every cable was further divided into multiple two-node elements, each also with six degrees of freedom.

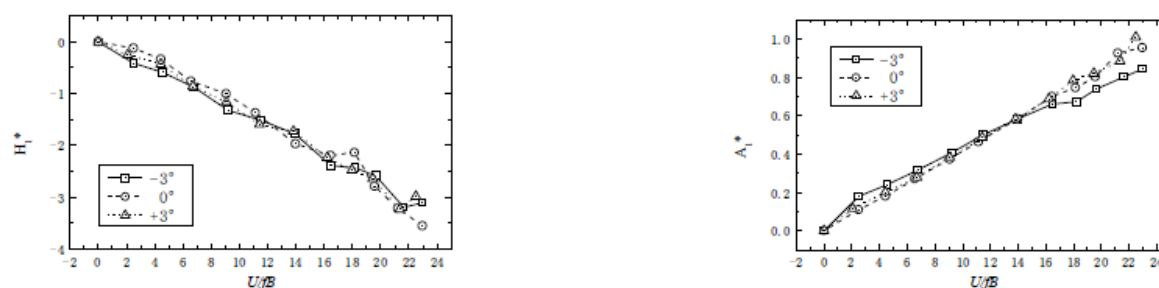
The results of the modal analysis are illustrated in Table 3.1.

Table 3.1 - Results of modal analysis [22]

Mode no.	Frequency (Hz)	Mode no.	Frequency (Hz)	Mode no.	Frequency (Hz)
1	0.0482	11	0.2000	21	0.2709
2	0.0776	12	0.2045	22	0.3077
3	0.1029	13	0.2094	23	0.3197
4	0.1090	14	0.2112	24	0.3205
5	0.1107	15	0.2179	25	0.3255
6	0.1336	16	0.2278	26	0.3352
7	0.1774	17	0.2281	27	0.3366
8	0.1809	18	0.2335	28	0.3481
9	0.1880	19	0.2540	29	0.3692
10	0.1900	20	0.2541	30	0.3702

In this work, a 1:60-scaled section model was studied in the uniform flow conditions to extract all flutter derivatives.

As an example, the flutter derivatives  $H_1^*$  and  $A_1^*$  of the completed stage for different wind attack angles are reported in Figure 3.14.

Figure 3.14 - Flutter derivative  $H_1^*$  and  $A_1^*$ 

To assess flutter stability, both two-dimensional and multi-mode coupled (three-dimensional) flutter analyses were conducted. In the latter approach, the first 30 lower vibration modes were considered, and the measured unsteady aerodynamic derivatives were included to evaluate the bridge's response more comprehensively. The critical flutter speeds obtained from wind tunnel experiments and analytical predictions are summarized in Table 3.2[22].

Table 3.2 - Comparisons of critical flutter wind speed between analysis and measurement [22]

analytical method		flutter speed (m/s)	flutter frequency (HZ)
analysis	two-dimensional flutter	91.367	0.1456
	multi-mode coupled flutter	89.626	0.1425
measured	section models	85-86	
	aero elastic full model of the bridge	>96.6	

These results show strong agreement, indicating that the numerical models reliably capture the bridge's aeroelastic behaviour.

This article is relevant and useful for the subsequent chapters, particularly due to the data and results derived for different analytical methods.

### 3.2.2 Chu *et al.* studies

This article [23] proposes a linear regression model to derive the probability density function (PDF) of the critical flutter wind speed directly from the PDFs of modal frequencies and damping ratios. This study utilizes field monitoring data from Xihoumen Bridge during 2010-2015, allowing an assessment of how structural properties have evolved over time. Finally, the model enables the calculation of the probability distribution of the critical flutter wind speed for each year, leading to the prediction of time-variant flutter probability. This approach addresses the challenges posed by aging structures and environmental degradation over extended time periods.

This integrated framework is illustrated schematically in Figure 3.15 below.

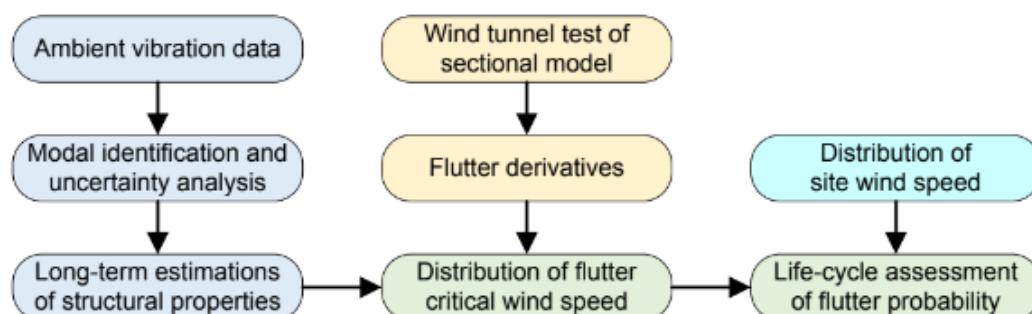


Figure 3.15 - Flow chart of assessment of flutter probability[23]

For this Thesis it is relevant to extract from this study the results of the modal analysis (Table 3.3) and flutter analysis (Figure 3.17), to be able to compare them with those obtained in Chapter 5 and 6. Of utmost importance, this work represents the source of the experimental flutter derivatives used for flutter analyses of Chapter 6.

Table 3.3 - The measured modal frequencies and damping ratios from vertical vibration by different methods[23]

EFDD/SSI Method <sup>[53]</sup>	Frequency(Hz)			EFDD Method <sup>[53]</sup>	SSI Method <sup>[53]</sup>	Damping Ratio(%)		Bayesian Damping Ratio COV (σ/MPV)	Mode Shape
	SSI Method <sup>[52]</sup>	Bayesian Method	Bayesian Frequency COV (σ/MPV)			SSI Method <sup>[52]</sup>	Bayesian Method		
0.095	0.0953	0.0948	0.2279%	1.12~2.64	1.80~2.18	0.57	0.78	32.48%	1-AS-V
0.133	0.1328	0.1330	0.1080%	0.84~2.32	0.90~1.46	0.52	0.47	32.57%	2-S-V
0.183	0.1825	0.1828	0.0547%	0.18~1.02	0.37~0.61	0.50	0.32	32.15%	2-AS-V
0.229	0.2301	0.2302	0.0963%	0.21~0.59	0.23~0.62	0.51	0.29	37.54%	1-S-T
0.233	\	0.2383	0.0801%	0.25~0.41	0.77~0.95	\	0.31	44.55%	1-AS-T
0.276	0.2767	0.2767	0.0820%	0.34~1.14	0.43~0.83	0.39	0.30	26.99%	3-AS-V

As examined in [24], vortex-induced vibration would occur at a low wind velocity (6-10 m/s). Therefore, there will exist aberrant values at certain low reduced velocities in  $A_4^*$ ,  $H_1^*$  and  $H_4^*$ , where abnormal points are excluded to improve the fitting accuracy.

All flutter derivatives are fitted by quadratic polynomial except  $H_2^*$ , which is fitted by quartic polynomial.

In Figure 3.16, measured values of flutter derivatives are reported with the polynomial model.

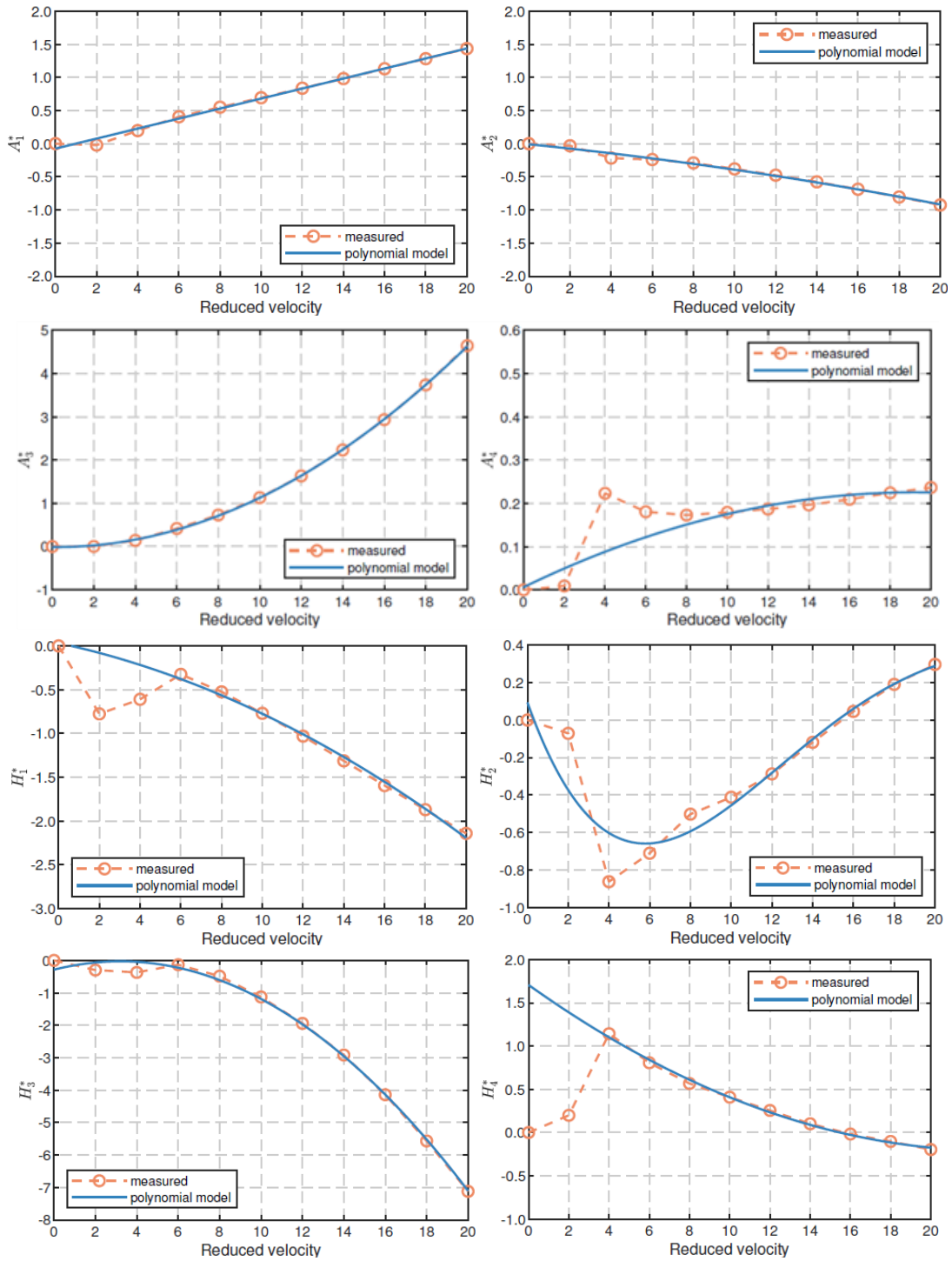


Figure 3.16 - Flutter derivatives of the Xihoumen Bridge section model[23]

For this thesis, the polynomial model is extracted and used for the flutter analysis in Chapter 6. It is worth noting the comparison between these experimental derivatives and those obtained with simplified calculations in Chapter 4.

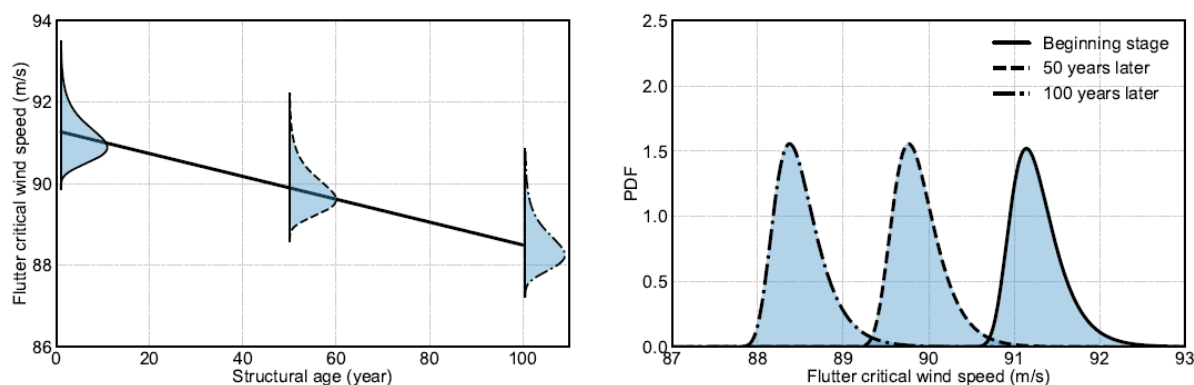


Figure 3.17 - Distributions of the flutter critical wind speed in 100-year structural age[23]

As shown in Figure 3.17, the mean value of the flutter critical wind speed in the long term tends to decrease in the structural life cycle, due to the deterioration effects of modal frequencies.

For further analysis in this Thesis, it is relevant to note that the flutter critical wind speed at the beginning stage is around 91 m/s.

### 3.2.3 Jiang et al. studies

The article [25] addresses the problem of Vortex-Induced Vibration (VIV) in a long-span bridges. This self-excited vibration, caused by the interaction of bridge motion with incoming wind, may induce fatigue damage to crucial structural components. The identification of Vortex-Induced Force becomes essential to predict the bridge response and to avoid the damage previously described.

To monitor the performance and safety of the Xihoumen Bridge and to identify VIV, a structural health monitoring (SHM) system was installed on the bridge. The SHM system is able to measure wind and acceleration data having several types of sensors, including three-dimensional ultrasonic anemometers and force-balance uniaxial accelerometer.

These data and the updating of a finite element model (Figure 3.18) were used by the authors to identify the generalized VIV time histories of the bridge.

For this Thesis, it is relevant to focus on the FEM modelling of the bridge and the subsequent Modal Analysis.

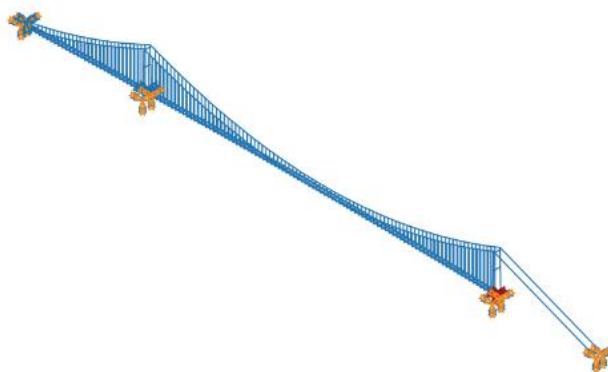











Figure 3.18 - Three-dimensional FE model of the Xihoumen Bridge[25]

The three-dimensional finite element model was established for the Xihoumen Bridge according to the bridge design drawings using the software ANSYS, as shown in Figure 3.18. The twin-box deck was idealized as two parallel beams connected by cross beams at 3.6 m intervals. Towers, longitudinal box girders and transversal cross beams were modelled with 3D elastic beam elements with tension, compression, torsion, and bending capacities. Main cables and hangers were modelled with cable elements. The profile of the main cable was determined by catenary function, and the spacing distance between two suspenders was 18 m. The connection between main cables and towers is managed with coupled translational degree of freedom. The bottom of the towers and the anchorages of the main cables were modelled as fixed ends.

In this work of Thesis, a similar FEM model was built in ANSYS, referred to as “Complete 2-axis model” and presented in Section 5.2.5.

Through an eigenvalue analysis on this FE model, the modal properties of the Xihoumen Bridge were found. The calculated first nine vertical natural frequencies and mode shapes of the bridge are given in Table 3.4.

Table 3.4 - The calculated first nine vertical natural frequencies and mode shapes of the Xihoumen Bridge[25]

Vertical mode	Mode shapes	Natural frequencies (Hz)
1 <sup>st</sup>		0.097
2 <sup>nd</sup>		0.101
3 <sup>th</sup>		0.133
4 <sup>th</sup>		0.178
5 <sup>th</sup>		0.182
6 <sup>th</sup>		0.228
7 <sup>th</sup>		0.260
8 <sup>th</sup>		0.269
9 <sup>th</sup>		0.323

This article is relevant and useful for the subsequent chapters, particularly due the representation of the mode shapes of the first vertical natural frequency of the structure. This is important for a good comparison between these results of the modal analysis and the others obtained in Section 5.2.

## **Chapter 4 - Approximate calculation of flutter derivatives**

This chapter focuses on the approximate calculation of flutter derivatives, a crucial aspect in the dynamic analysis of suspension bridges, especially when experimental data are limited or unavailable. The two methodologies presented in this chapter allow us to estimate these derivatives through analytical and numerical approaches.

In addition, the chapter presents a brief discussion on the gap-width sensitivity in multi-box girder suspension bridges. This analysis is fundamental to understand how variations in gap dimensions between the individual boxes affect the overall aerodynamic characteristics and stability of the bridge deck.

Finally, a comprehensive comparison is made between the results obtained from these simplified methods applied to Xihoumen Bridge and the experimental flutter derivatives.

### **4.1 Flat plate**

One of the first analytical approaches was developed by Theodorsen [12], that addressed the problem of determining the aerodynamic forces on a thin airfoil subjected to harmonic oscillations in a two-dimensional, incompressible, and perfectly inviscid flow.

The unsteady formulation of the lift and moment forces is characterized as the superposition of two contributions: circulatory and non-circulatory. The circulatory component depends on the oscillation frequency and captures unsteady flow effects, while the non-circulatory component is independent of frequency and accounts for the inertial effects of the displaced fluid mass. It must be noticed that circulatory contributions to lift and moment are function of both time and frequency. [26]

The complex expressions for the motion dependent unsteady forces can be converted in the 8 complex derivatives given in Equations 4.1 – 4.8:

$$H_1^* = -2\pi \frac{F(k)}{k} \quad (4.1)$$

$$H_2^* = -\pi \left[ \frac{1}{2k} + \frac{F(k)}{k} \left( \frac{1}{2} - a \right) + 2 \frac{G(k)}{k^2} \right] \quad (4.2)$$



$$H_3^* = -\pi \left[ \frac{a}{4} + 2 \frac{F(k)}{k^2} - \frac{G(k)}{k} \left( \frac{1}{2} - a \right) \right] \quad (4.3)$$

$$H_4^* = \pi \left[ \frac{1}{2} + 2 \frac{G(k)}{k} \right] \quad (4.4)$$

$$A_1^* = \pi \left( \frac{1}{2} + a \right) \frac{F(k)}{k} \quad (4.5)$$

$$A_2^* = \pi \left[ -\frac{1}{4k} \left( \frac{1}{2} - a \right) + \frac{F(k)}{2k} \left( \frac{1}{4} - a^2 \right) + \frac{G(k)}{k^2} \left( \frac{1}{2} + a \right) \right] \quad (4.6)$$

$$A_3^* = \pi \left[ \frac{1}{8} \left( \frac{1}{8} + a^2 \right) + \frac{F(k)}{k^2} \left( \frac{1}{2} + a \right) - \frac{G(k)}{2k} \left( \frac{1}{4} - a^2 \right) \right] \quad (4.7)$$

$$A_4^* = -\pi \left[ \frac{a}{4} + \frac{G(k)}{k} \left( \frac{1}{2} + a \right) \right] \quad (4.8)$$

Where:

- $k = \omega B/U$  is the reduced frequency of the airfoil, where  $\omega$  is circular frequency;
- $a$  is the distance between the shear centre and the centroid of the airfoil, normalized with respect to the chord  $B$ ;
- $F(k_j)$  and  $G(k_j)$  are the real and the imaginary parts of Theodorsen's complex circulatory function, which is well explained below;

It is normally assumed that the elastic axis and centre of gravity are located at the mid-chord of the deck ( $a = 0$ ) and the flat plate is approached by flow with a small angle of attack ( $\alpha \approx 0$ ), as it can be seen in Figure 4.1. This is frequently used for bridges.

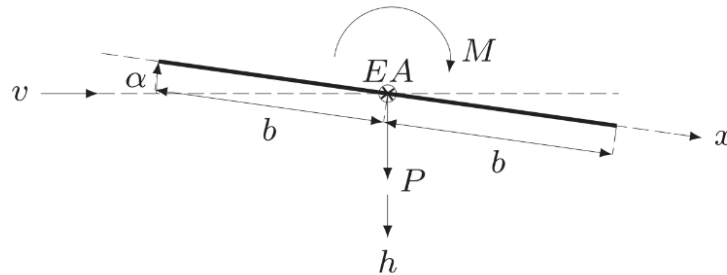


Figure 4.1 - Sign convention following [12] for a single flat plate

Lag effects on the pressure distribution over the flat plate are incorporated into the model through the complex circulatory function,  $C(k) = F(k) + iG(k)$  [12]. The time lag arises from

the temporal and spatial differences between the bound vorticity on the flat plate and the wake vorticity, which is assumed to be carried downstream at the mean wind speed.

The circulatory function,  $C(k)$ , can be expressed by Hankel functions of the second kind or approximated by a rational function:

$$C(k) = F(k) + iG(k) = \frac{H_1^{(2)}(k)}{H_1^{(2)}(k) + iH_0^{(2)}(k)} \approx 1 - \frac{0.165k}{k - i0.0455} - \frac{0.335k}{k - i0.3} \quad (4.9)$$

Where:  $i = \sqrt{-1}$

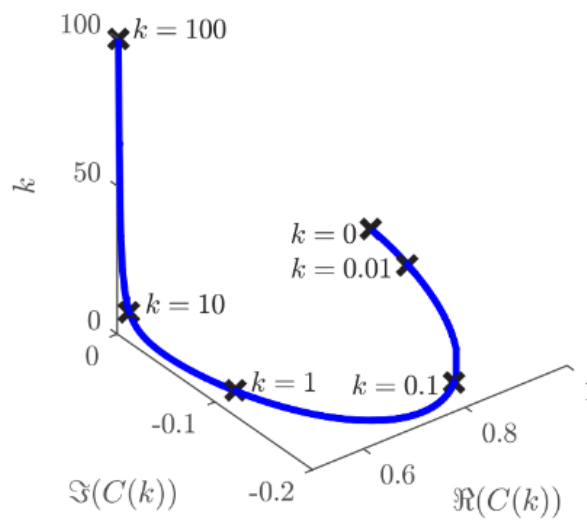


Figure 4.2 – Real,  $\Re(C(k))$ , and Imaginary,  $\Im(C(k))$ , part of Theodorsen's circulatory function,  $C(k)$  [27]

## 4.2 Superposition of flat plates

In [27] the authors present a two-dimensional model based on the superposition of Theodorsen's flat plate theory, with the aim of approximating the aeroelastic effects on an arbitrary multi-box bridge girder.

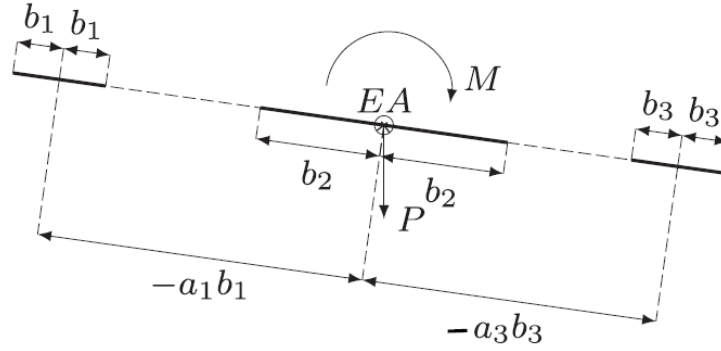


Figure 4.3 - Example of multi-box bridge girder

The flat plates have a common elastic axis (of the total deck), which means that the mid-chord of each plate is positioned at a specific location relative to this axis (as it can be seen in Figure 4.3). The spans between them introduce extra terms into the aerodynamic damping and stiffness matrices.

The gap-width between boxes will cause shed vorticity from each box and consequently unsteadiness in the lift forces on all boxes. If it is assumed that the circulation around each box is only affected by its own wake and that the box is hypothesized as a flat plate, it is possible to use Theodorsen's unsteady formulations [12] to model the aeroelastic effects. Thus, the mutual induction between the bound circulations on each of the interconnected flat plates are not included in the model.

For  $n$  flat plates oscillating in phase around the same elastic axis, flutter derivatives can be expressed by the sum of contributions from each flat plate, as consequently reported in Equations 4.10 – 4.17:

$$H_1^*(v, \omega) = -4\pi \frac{q}{v} \sum_{j=1}^n b_j F(k_j) \quad (4.10)$$

$$H_2^*(v, \omega) = -2\pi \frac{q}{v} \sum_{j=1}^n b_j^2 \left( 1 + 2 \left( \frac{1}{2} - a_j \right) F(k_j) + \frac{2G(k_j)}{k_j} \right) \quad (4.11)$$

$$H_3^*(v, \omega) = -2\pi q \sum_{j=1}^n b_j (a_j k_j^2 + 2F(k_j) - (1 - 2a_j)G(k_j)k_j) \quad (4.12)$$

$$H_4^*(v, \omega) = 2\pi q \sum_{j=1}^n (k_j^2 + G(k_j)2k_j) \quad (4.13)$$

$$A_1^*(v, \omega) = 4\pi \frac{q}{v} \sum_{j=1}^n b_j^2 F(k_j) \left( \frac{1}{2} + a_j \right) \quad (4.14)$$

$$A_2^*(v, \omega) = -2\pi \frac{q}{v} \sum_{j=1}^n b_j^3 \left( \frac{1}{2} - a_j + 2F(k_j) \left( a_j^2 - \frac{1}{4} \right) - \frac{2G(k_j) \left( a_j + \frac{1}{2} \right)}{k_j} \right) \quad (4.15)$$

$$A_3^*(v, \omega) = 2\pi q \sum_{j=1}^n b_j^2 \left( k_j^2 \left( a_j^2 + \frac{1}{8} \right) + 2F \left( a_j + \frac{1}{2} \right) + 2k_j G(k_j) \left( a_j^2 - \frac{1}{4} \right) \right) \quad (4.16)$$

$$A_4^*(v, \omega) = -2\pi q \sum_{j=1}^n b_j \left( a_j k_j^2 + 2k_j G(k_j) \left( a_j + \frac{1}{2} \right) \right) \quad (4.17)$$

Where:

- $b_j$  is the half-width of the  $j$ -th box;
- $a_j$  is the non-dimensional distance between the box chord midpoint and the global rotation axis (elastic axis);
- $k_j = \omega b_j / U$  is the reduced frequency of the  $j$ -th box, where  $\omega$  is the same for all boxes;
- $F(k_j)$  and  $G(k_j)$  are the real and the imaginary parts of Theodorsen's complex circulatory function;
- $q = \rho/2v$  is the dynamic pressure, where  $\rho$  and  $v$  are the density of air and the incoming mean wind speed, respectively.

#### 4.2.1 Gap-width sensitivity

In the calculations of flutter derivatives through the Andersen's simplified approach [27], the gap width, which refers to the physical separation between the individual box elements in a multi-box girder configuration, plays a significant role on the flutter analysis.

In [27] it is investigated how variations in the gap width affect the aerodynamic flutter derivatives, particularly those associated with torsional behaviour. To do this, a simple model for interconnected flat plates was proposed and applied to a multi-box section, featuring a typical box-shaped girder at the centre with two flat-plate-like boxes laterally positioned.

The authors, then, modified the theoretical model by introducing a scaling factor,  $\nu$ , that will multiply the non-dimensional distance  $a_j$  to reduce it. This adjustment compensates the overestimation of the critical flutter wind speed given by the approximation of a bridge girder with a flat plate and the ignorance of the aerodynamic interference among the girders.

In the examples provided by the authors [27], introducing  $\nu$  allowed to predict critical flutter wind speed to more accurately match the values observed in wind tunnel tests, ensuring a more reliable assessment of the bridge's aeroelastic stability.

Since no terms with  $a_j$  is present for the complex expressions for  $H_1^*$  and  $H_4^*$  in Equations 4.10 - 4.17, these are not affected by  $\nu$ . Furthermore, since the boxes are symmetric around the elastic axis of the total deck, the complex  $H_2^*$ ,  $H_3^*$ ,  $A_1^*$  and  $A_4^*$  are unaffected by the value of the gap-width. It was observed that the gap-width mainly affects the real valued flutter derivatives  $A_2^*$  and  $A_3^*$ , with a decrease of the former and an increase of the latter. The superposition of flat plate derivatives successfully captures the reduction in  $A_2^*$ , but it does not reflect the observed increase in  $A_3^*$ . Furthermore, the sum of chord-widths seems to affect  $H_1^*$  and  $A_1^*$ . [27]

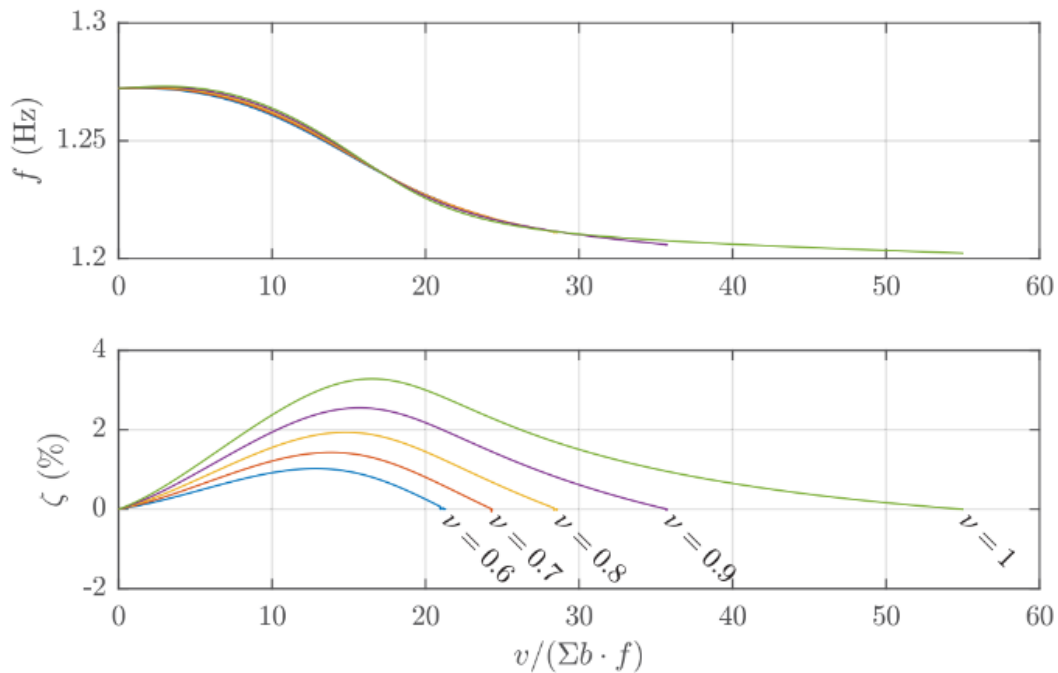


Figure 4.4 - Frequencies ( $f$ ) and damping ratios ( $\zeta$ ) for the torsional dominated mode of the case-study analysed in [27], for different values of the gap-width scaling factor ( $\nu$ )

The damping ratio shown in the graph below in Figure 4.4 represents the real part of the eigenvalue for the torsional branch, which is mainly influenced by  $A_2^*$ , but also by  $A_3^*$  (and the other flutter derivatives). The graph shows a decrease in the damping ratio when the gap-width scaling factor is introduced, due to the increase in  $A_2^*$  (aerodynamic torsional damping) and  $A_3^*$  (aerodynamic torsional stiffness), which can also be seen in Figure 4.5 for the case study analyzed.

The increase of these two flutter derivatives contributes with a destabilizing effect, but with different scale. It is worth to highlight the predominant contribution of  $A_2^*$  over  $A_3^*$ , noting that

the frequencies (which are known to be affected by  $A_3^*$  but not by  $A_2^*$ ) remain unchanged by the corrective factor (Figure 4.4). Therefore, the damping is more strongly affected by the gap-width scaling factor than the frequencies (and so than the stiffness).

The application of the scaling factor to a real case study [27] allows us to use the same  $\nu$  ( $\nu=0.7$ ) value in the calculations of the flutter derivatives for the Xihoumen Bridge, as shown in the next section. This hypothesis is adopted considering that the case studies differ from each other, so the results might not be entirely realistic. The primary aim is to study the gap-width sensitivity on the Xihoumen Bridge, which for years has been the longest multi-box girder suspension bridge in the world.

### 4.3 Application to the case study

In this section, the flutter derivatives, obtained through the previously discussed approximate calculations, are applied to the case study and plotted with the goal of comparing them to those obtained experimentally in wind tunnel tests. The aim is to evaluate the accuracy of the theoretical predictions and identify areas for further refinement.

Andersen's flutter derivatives will be used for 1-axis models (see Sections 5.2.2 and 5.2.4). The non-dimensional distance  $a_j$  is defined as the gap between the total deck's centroid and the single box's barycentre; this distance is reduced when the gap-width scaling factor ' $\nu$ ' is applied (see Section 4.3.1).

On the other hand, Theodorsen's flutter derivatives will be applied to both axis of the 2-axis models (see Sections 5.2.3 and 5.2.5), each considered as a flat plate that spans the width of the single box.

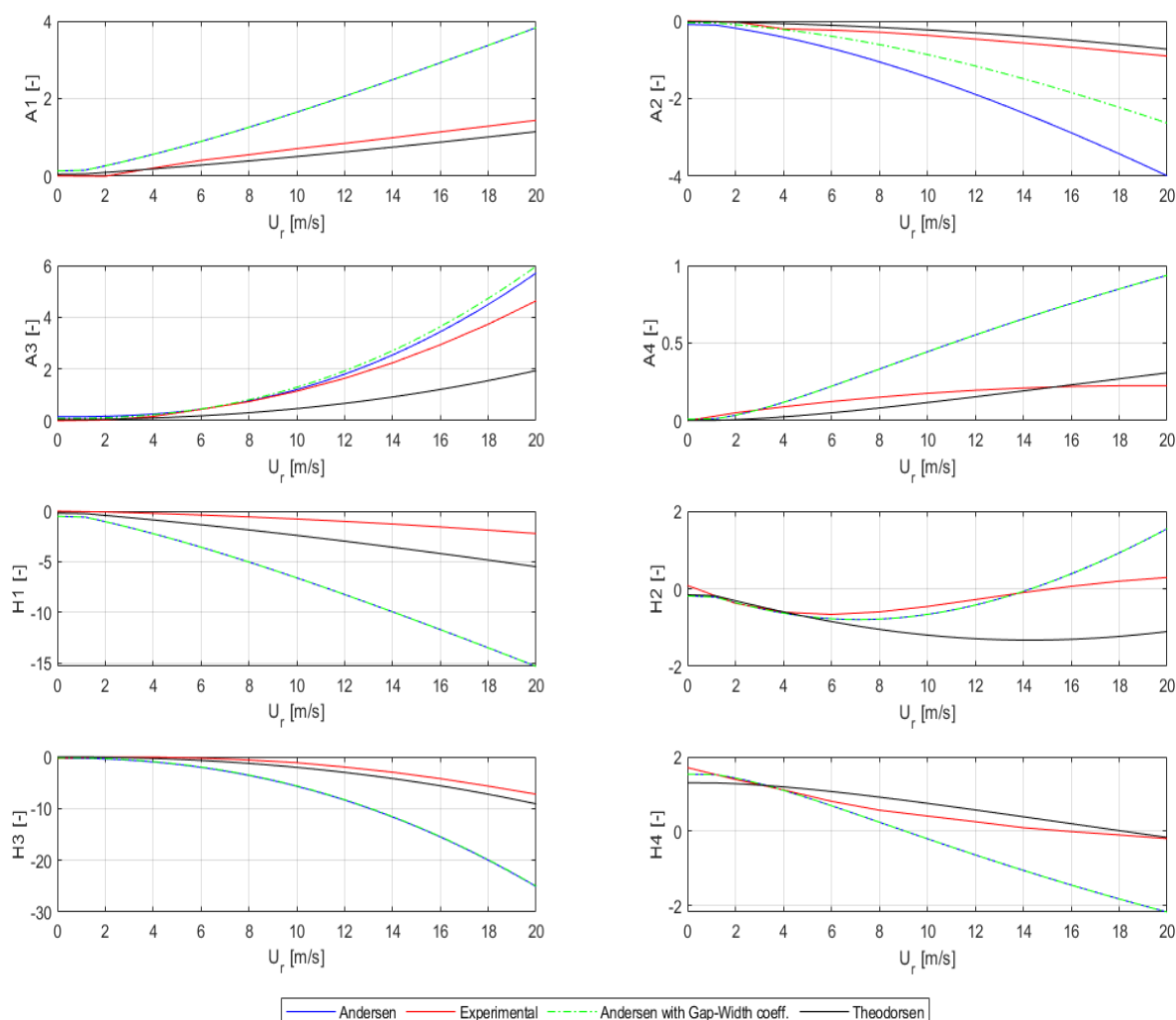


Figure 4.5 - Flutter derivatives of the Xihoumen Bridge

Andersen's methods provide a good estimation for  $A_3^*$  flutter derivative, which describes the aerodynamic torsional stiffness and plays a fundamental role in flutter prediction. In fact, in the range of reduced velocity, where bridge scaled model were tested in wind tunnel, the trend of the Andersen's flutter derivative could approximate in a good way the experimental one, in particular when applying the gap-width scaling factor.

In the same way, the gap-width scaling factor improves the estimation of the  $A_2^*$  flutter derivative (even if not perfectly), which describes the aerodynamic torsional damping.

On the other hand, the flutter derivatives  $H_1^*$ ,  $H_4^*$ ,  $A_1^*$ ,  $A_4^*$ ,  $H_2^*$  and  $H_3^*$  show no variation regardless of whether the gap-width scaling factor is applied, because the first two do not include the  $a_j$  term, while the others are unaffected due to the symmetry of the boxes about the elastic axis of the total deck.

Overall, Theodorsen's method provides a good agreement for  $A_1^*$ ,  $A_2^*$ ,  $A_4^*$ ,  $H_3^*$  and  $H_4^*$  flutter derivatives. In contrast, it significantly underestimates  $A_3^*$  that is the aerodynamic torsional stiffness, and it is crucial in stiffness-driven flutter (classical flutter).

The comparisons shown in the Figure 4.5 do not allow us to conclude that Andersen's formula yields significantly better results than Theodorsen's formula. This may be ascribed to the relatively small air gap featured by the Xihoumen bridge with respect to those of the multi-box tested in the work of Andersen.

In general, the differences observed in Figure 4.5, and in experiments reported in the literature, suggest that the presence of gap-width reduces  $A_2^*$  (a stabilizing contribution) while increasing  $A_3^*$  (a destabilizing contribution). Andersen's formulas, through his multi-plates model, capture this phenomenon, generally leading to an increase on the flutter critical speed compared to Theodorsen's method, due to the predominant effect of  $A_2^*$ . This is one reason why multi-box girders are inherently more stable than single-box ones.



## Chapter 5 - Structural models and modal analysis results

### 5.1 Analytic model (MATLAB)

As described in Section 2.5, in this paragraph, the Modal Analysis is performed considering the main features of the case study summarized in Table 5.1.

*Table 5.1 - Geometrical and mechanical properties of the Xihoumen Bridge*

Span length	$l$ [m]	1650
Sag	$f$ [m]	165
Cable length	$l_{\text{cable}}$ [m]	1692.9
Total deck width	$B$ [m]	36
Distance between cables	$b$ [m]	31.4
Deck density	$\rho_{\text{deck}}$ [kg/m <sup>3</sup> ]	19165
Cable density	$\rho_{\text{cable}}$ [kg/m <sup>3</sup> ]	6827.8
Deck area	$A_{\text{deck}}$ [m <sup>2</sup> ]	1
Cable area	$A_{\text{cable}}$ [m <sup>2</sup> ]	1.1216
Polar mass moment of inertia per unit length	$I_0$ [kgm <sup>2</sup> /m]	3851136
Equivalent vertical moment of inertia	$I_z$ [m <sup>4</sup> ]	10
Sectorial moment of inertia	$I_\omega$ [m <sup>4</sup> ]	0
Equivalent torsion constant	$I_t$ [m <sup>4</sup> ]	6
Young's modulus of the deck	$E_{\text{deck}}$ [N/m <sup>2</sup> ]	2.1E+11
Young's modulus of the main cables	$E_{\text{cable}}$ [N/m <sup>2</sup> ]	1.1E+11
Poisson's ratio	$\nu$	0.3

In this analytic model, the contribution of the lateral spans and the towers is considered through a reduction in the main cables' elastic modulus. In fact, in this way, it is evaluated the flexibility of the towers, reducing the error done by using the fixed restraints at the edge of the main cables. The equivalent modulus is thus one of the parameters used to fit the natural vibration frequencies of the bridge.

Note that the equivalent torsion constant  $I_t$  is used to fit the natural frequencies also; in fact, it is considered 6 [m<sup>4</sup>] instead of 4.628 [m<sup>4</sup>] to reach more realistic results in terms of modal analysis.

Considering the equations 2.30 and 2.31, eight sinusoidal functions ( $n = m = 8$ ,  $N = n + m$ ) were chosen to describe the vertical and torsional displacement components. Consequently, the first eight modes are reported in Figure 5.1.

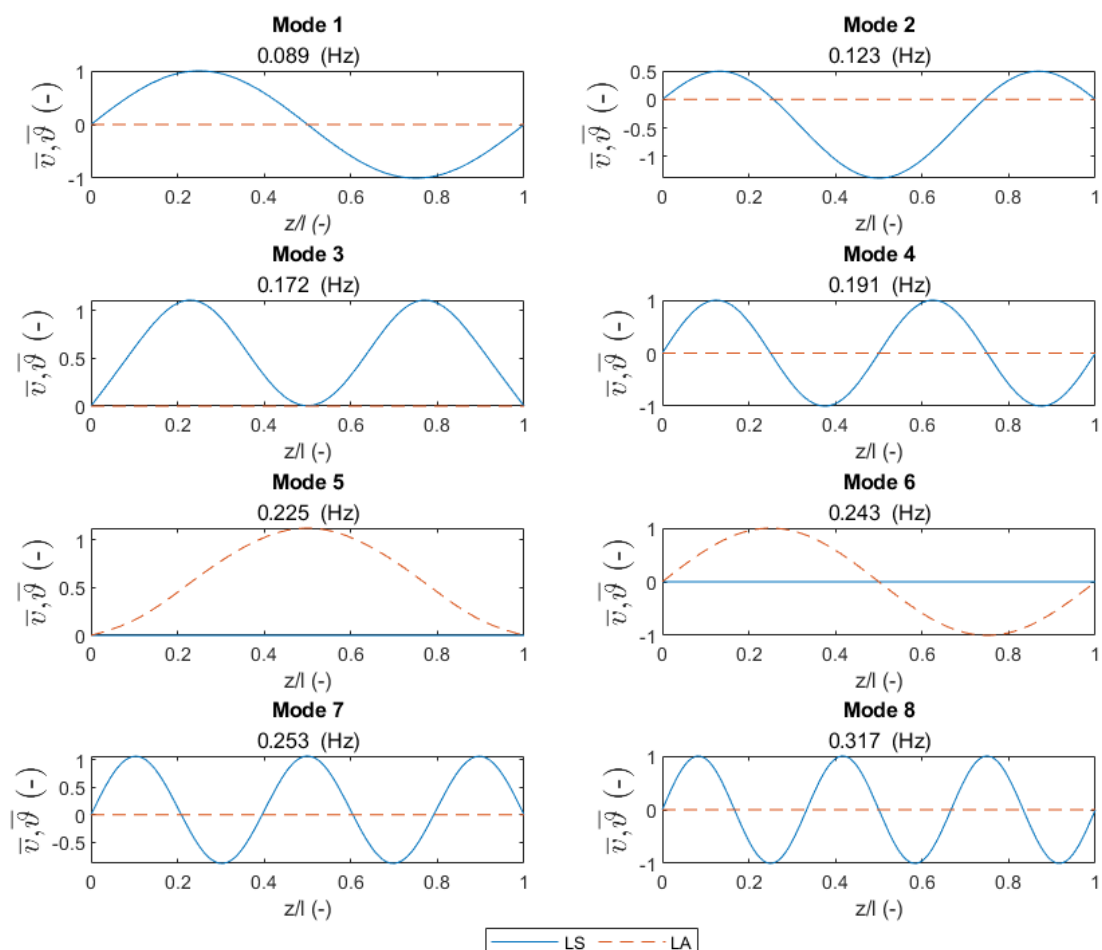


Figure 5.1 - Xihoumen Bridge modal shapes in wind-free condition

In the wind-free condition, the mode shapes are distinct, either torsional or vertical. In fact, in Figure 5.1, the blue line represents the vertical displacement component, while the orange line depicts the torsional one.

## 5.2 Finite Element Models

Given the scale and complexity of the bridge selected as a case study, several 3D finite element models were developed in ANSYS. This is done to obtain results that align with those of other researchers. The extensive information available on the Xihoumen Bridge made possible to build a comprehensive model that includes towers, the designed twin box girder deck, the main span, and the lateral ones. For the numerical simulation of the mechanical behaviour, three distinct types of finite elements were employed [28]

1. The BEAM188 element is based on Timoshenko beam theory. It is a three-dimensional, two-node beam element with six degrees of freedom at each node: translations and rotations along the three axes.
2. The LINK180 element is a 3D element used for hangers. It is a uniaxial tension-compression element with three translational degrees of freedom per node.
3. The MASS21 element is a point element with up to six degrees of freedom, used to model structural mass properties. In this case, it was employed exclusively to adjust the deck's mass moment of inertia, as the weight of the elements was defined through a combination of sectional properties and material models assigned to the beam elements.[4]

Given the extensive and complex availability of data on the geometric and mechanical properties of the structure, the models developed and validated in ANSYS APDL are the result of an iterative calibration process of key parameters governing the structural behaviour, such as the moments of inertia, the torsional modulus of the deck section, and the elastic modulus of the main cable.

A total of four different numerical models of the bridge were developed, which are presented in the following sections. Models can be distinguished by their approach to deck modelling. Some employ a two-axis configuration while others use a single-axis design, and they differ in whether side spans and towers are incorporated.

### 5.2.1 Deck Polar moment of inertia

In this Section, the calculation of the polar mass moment of inertia is presented for the 1-axis and 2-axis models.

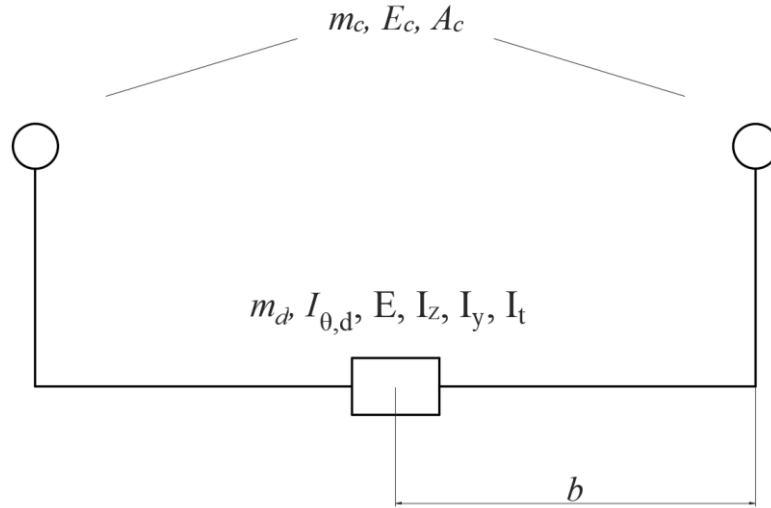


Figure 5.2 - Scheme of 1-axis equivalent deck and cables

For the 1-axis model, the polar mass moment of inertia around the deck longitudinal axis can be expressed by the sum of the deck and cables contributions as:

$$I_{\vartheta} = I_{\vartheta,d} + 2 \left( \frac{m_c}{2} b^2 \right) \quad (5.1)$$

Where  $m_c$  is the cable mass per unit length,  $I_{\vartheta,d}$  is the polar mass moment of inertia of the deck. Neglecting the polar moment of inertia of cables around their longitudinal axis and considering their parallel axis terms defined by the Huygens-Steiner theorem, the deck polar moment of inertia is given by the contributions of beam and mass elements as:

$$I_{\vartheta,d} = (I_z + I_y) \frac{m_d}{A_d} + I_{xx} \quad (5.2)$$

The first term of the right-hand side represents the polar moment of inertia which ANSYS APDL associates with the deck beam elements, having mass  $m_d$ , transversal area  $A_d$  (considered equal to 1 in these calculations), and geometric moments of inertia  $I_z$  and  $I_y$ .  $I_{xx}$  represents the polar moment of inertia per unit length span associated with the nodal mass element (MASS21).  $I_{xx}$  is used to fit the polar moment of inertia  $I_{\vartheta}$ , which is a given data, and is calculated as:

$$I_{xx} = I_{\vartheta} - (I_z + I_y) \frac{m_d}{A_d} - 2 \left( \frac{m_c}{2} b^2 \right) \quad (5.3)$$

and accounting for the discrete distributions of mass elements:

$$I_{xx,M21} = I_{xx} \frac{l}{n_{M21}^{\circ}} \quad (5.4)$$

where  $n_{M21}^{\circ}$  is the number of mass elements attached to deck nodes and  $l$  is the length of the span.

For the 2-axis model, MASS21 elements are attached to both deck girders.

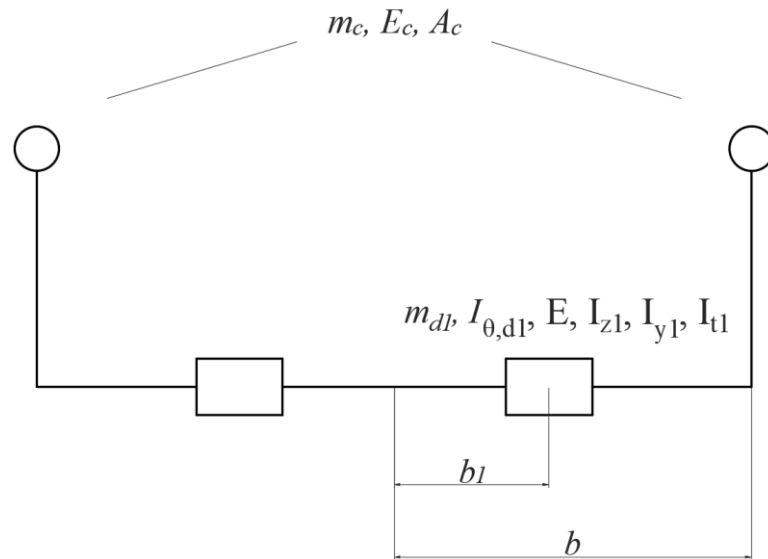


Figure 5.3 - Scheme of 2-axis equivalent deck and cables

The polar mass moment of inertia around the deck longitudinal axis can be expressed, considering the symmetry around the centre axis, by the sum of the two box girders and cables contributions as:

$$I_{\theta} = \left[ 2 \left( I_{xx} + \frac{m_{d,1}}{A_{d,1}} (I_{z1} + I_{y1}) + \frac{m_{d,1}}{A_{d,1}} b_1^2 \right) \right] + [2(m_c b^2)] \quad (5.5)$$

Where subscript “1” refers to the single deck, as shown in Figure 5.3.

For the calculus of the deck polar moment of inertia  $I_{\theta,d1}$ , the polar moment of inertia of cables around their longitudinal axes are neglected: only their parallel axis terms defined by the Huygens-Steiner theorem are considered.

The first term of the right-hand side, excluding  $I_{xx}$ , represents the polar moment of inertia which ANSYS APDL associates with the deck beam elements (including parallel axis terms). It is

considered for each box-girder the mass  $m_{d,1}$ , transversal area  $A_{d,1}$  (considered equal to 1 in these calculations), and geometric moments of inertia  $I_{z1}$  and  $I_{y1}$ .  $I_{xx}$  represents the polar moment of inertia per unit length span associated with the nodal mass element.

Also in this model,  $I_{xx}$  is used to fit the polar moment of inertia  $I_{\theta}$ , and is calculated as:

$$I_{xx} = \frac{I_{\theta}}{2} - m_c b^2 - m_{d,1}(I_{z1} + I_{y1}) - m_1 b_1^2 \quad (5.6)$$

and accounting for the discrete distributions of mass elements:

$$I_{xx,M21} = I_{xx} \frac{l}{n^{\circ}_{M21}} \quad (5.7)$$

where  $n^{\circ}_{M21}$  is the number of mass elements attached to the deck nodes of a single girder.

## 5.2.2 Central span 1-axis model

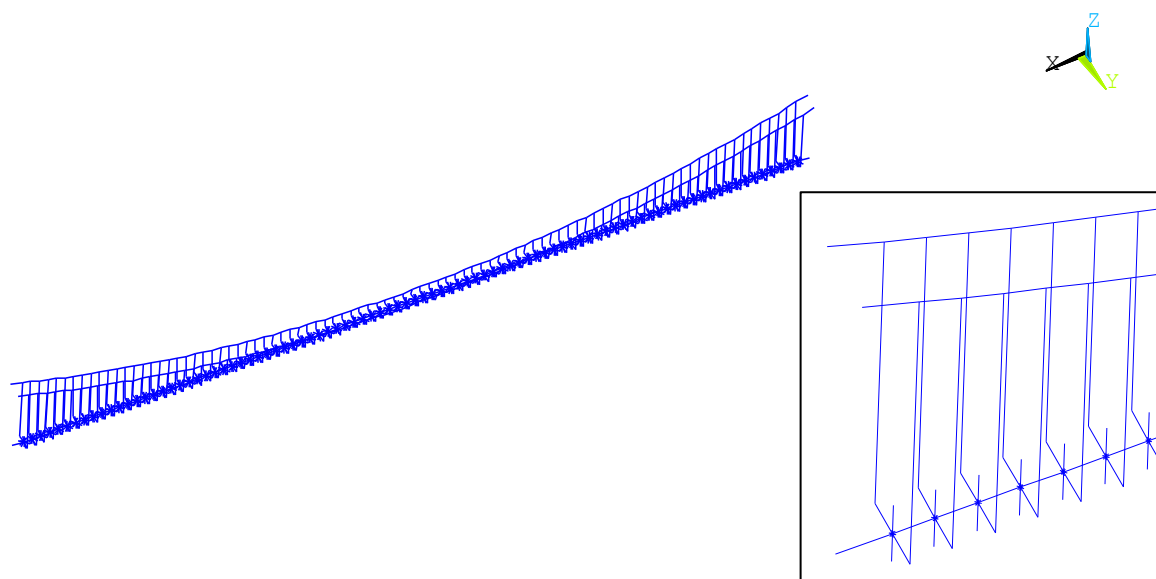


Figure 5.4 – Central span 1-axis FE model with a detail on the right

In this model, the two cables are characterised by an equivalent diameter of 0.845 metres. The bridge deck is schematised by means of a single central axis, which is assigned equivalent properties considering both longitudinal box girders. This axis is connected to the hangers through rigid links.

The deck is constrained by means of hinges that allow rotation in all directions, while rotation around the longitudinal axis is prevented for the main cables and deck's axis. The equivalent deck beams and main cables are modelled using BEAM188 elements, which are assigned the appropriate geometric and mechanical properties. Rigid connections are defined with high inertia to ensure rigid flexural behaviour, while their weight is set to zero. The hangers, on the other hand, are modelled with LINK180 elements, which are only capable of transmitting tensile forces between the deck and the main cables.

In analogy to the analytical model implemented in MATLAB, an equivalent elastic module for the cables is used to correctly reproduce the natural vibration frequencies of the bridge. This allows to account for the towers and side spans contribution which are excluded in the Finite Element Model [29].

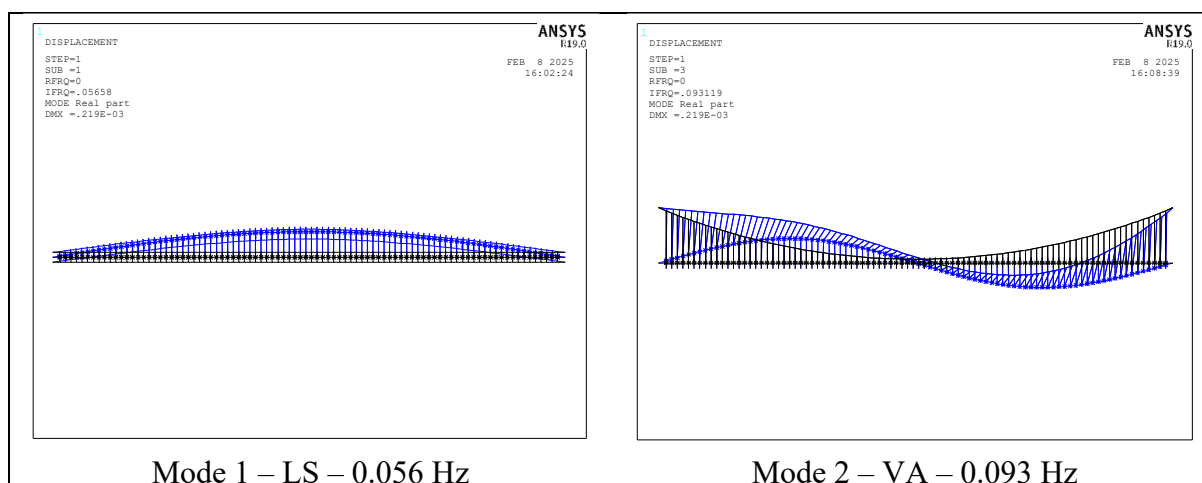
In particular, same geometric and mechanical properties used in the analytical model are considered, but with the adding of equivalent lateral moment of inertia:

Table 5.2 - Geometrical and mechanical properties of the Xihoumen Bridge

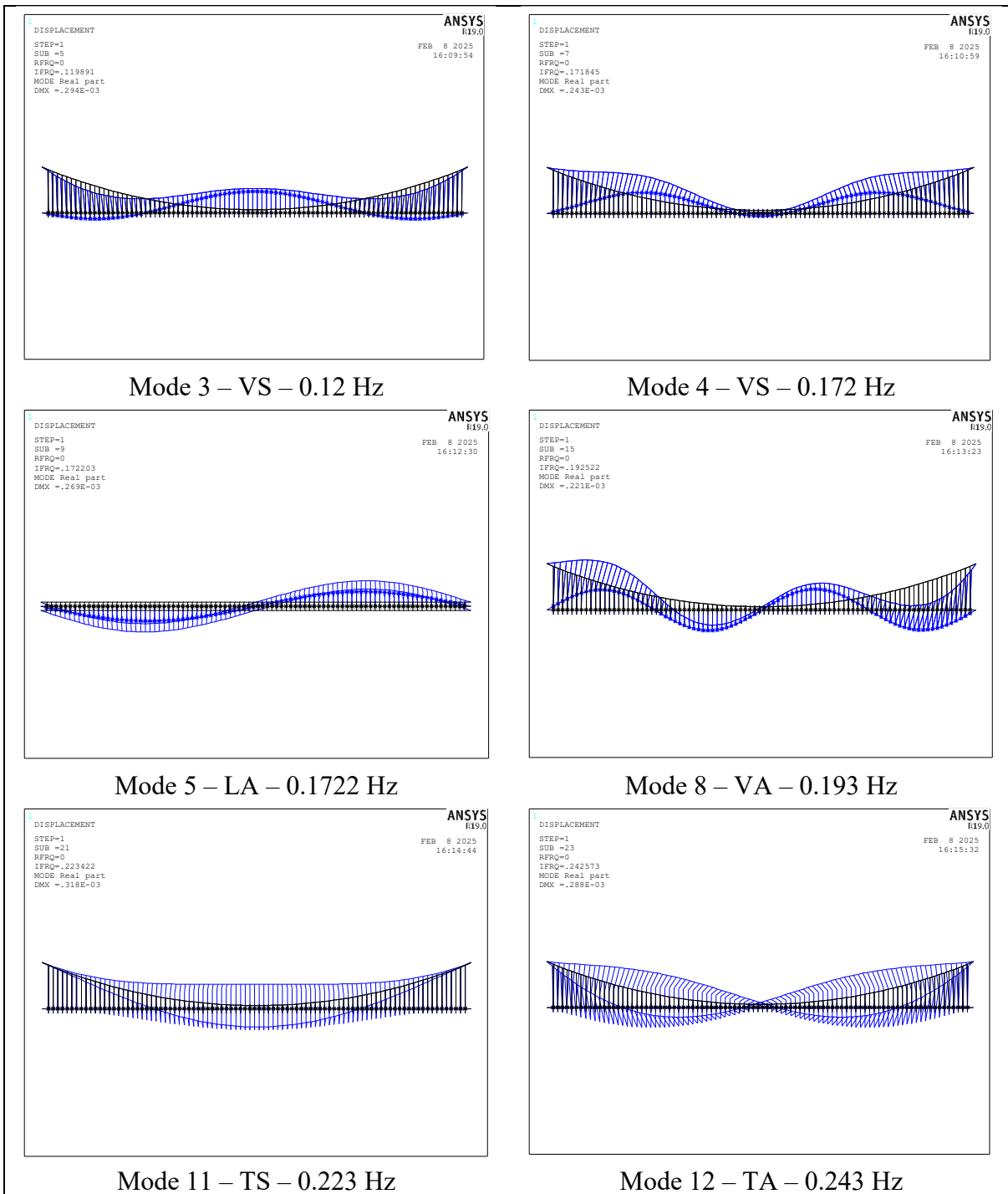
Central span length	$l$ [m]	1650
Sag	$f$ [m]	165
Cable length	$l_{\text{cable}}$ [m]	1692.9
Total deck width	$B$ [m]	36
Distance between cables	$b$ [m]	31.4
Deck density	$\rho_{\text{deck}}$ [kg/m <sup>3</sup> ]	19165
Cable density	$\rho_{\text{cable}}$ [kg/m <sup>3</sup> ]	6827.8
Hanger density	$\rho_{\text{hanger}}$ [kg/m <sup>3</sup> ]	0
Deck area	$A_{\text{deck}}$ [m <sup>2</sup> ]	1
Cable area	$A_{\text{cable}}$ [m <sup>2</sup> ]	1.1216
Polar mass moment of inertia per unit length	$I_0$ [kgm <sup>2</sup> /m]	3851136
Equivalent vertical moment of inertia	$I_z$ [m <sup>4</sup> ]	10
Equivalent lateral moment of inertia	$I_y$ [m <sup>4</sup> ]	566
Sectorial moment of inertia	$I_{\omega}$ [m <sup>4</sup> ]	0
Equivalent torsion constant	$I_t$ [m <sup>4</sup> ]	6
Polar mass moment of inertia attributed to M21 elements	$I_{xx, \text{MASS21}}$ [kgm <sup>2</sup> ]	-1.66E+08
Young's modulus of the deck	$E_{\text{deck}}$ [N/m <sup>2</sup> ]	2.1E+11
Young's modulus of the main cables	$E_{\text{cable}}$ [N/m <sup>2</sup> ]	1.1E+11
Poisson's ratio of steel	$\nu_{\text{steel}}$	0.3

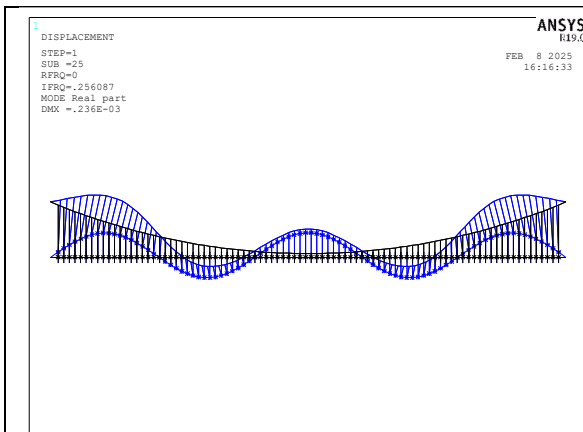
In the following table (Table 5.3), the most significant mode shapes of the considered model are shown. It can be seen the deformed shape over the undeformed one, underlining the values of the natural frequencies and the typologies of the mode shape. In this table, and onwards, L, V, T denote respectively lateral, vertical and torsional modes, whereas S and A stand for Symmetric and Antisymmetric, respectively.

Table 5.3 - Modal frequencies and modal shapes of the Central Span 1-axis Model

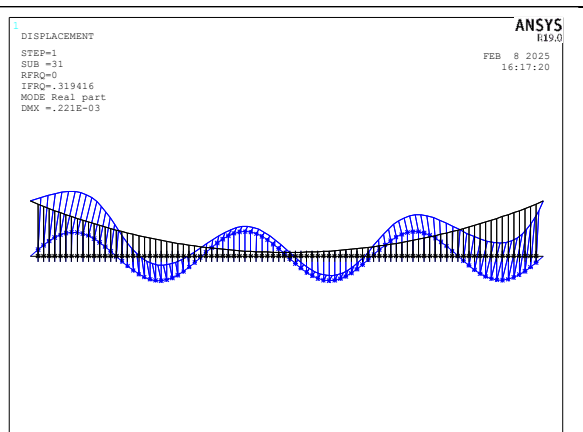








Mode 13 – VS – 0.256 Hz



Mode 16 – VA – 0.319 Hz

### 5.2.3 Central span 2-axis model

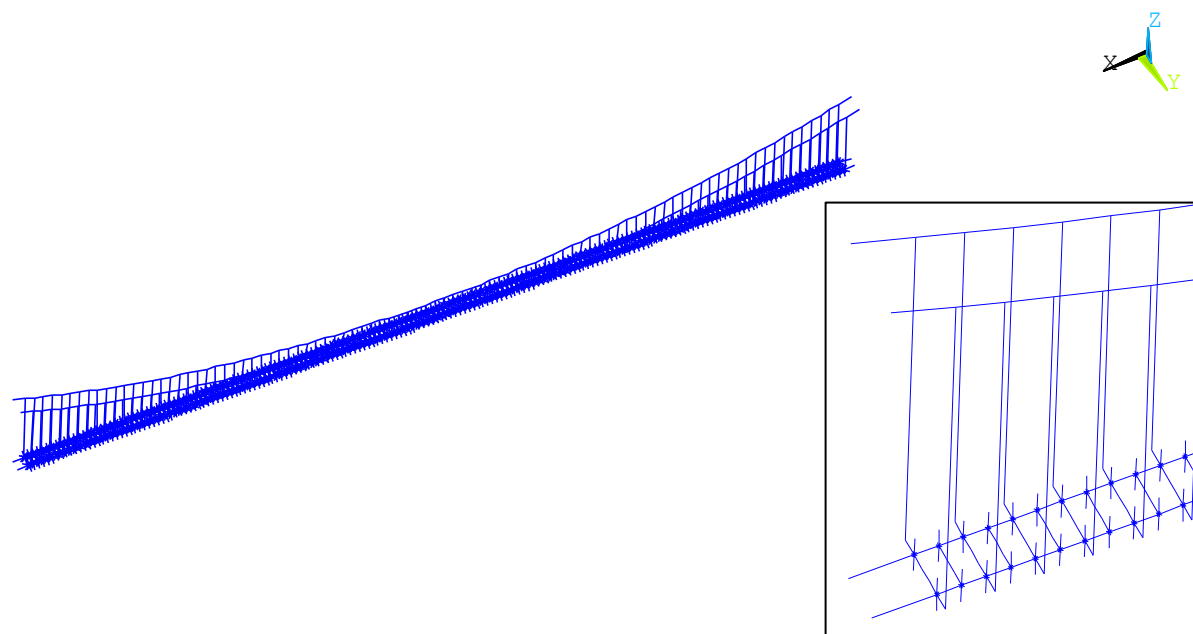


Figure 5.5 - Central span 2-axis FE model with a detail on the right

To achieve a more realistic model, the two longitudinal boxes of the deck are modelled (Figure 5.5) by BEAM188 elements, to which are assigned the geometrical and mechanical properties listed in Table 5.4.

Since the literature provides the inertias for the entire deck, this model calculates them for an individual box girder. Specifically, the vertical and torsional moments of inertia for each single box are assumed to be half of the total deck's values, while the lateral moment of inertia is determined through AutoCAD modelling of the boxes. With the known deck's overall moment of inertia about its central axis, the moment of inertia of a single box about its centre of mass can be readily computed using the Huygens-Steiner theorem.

In particular, in this model the two longitudinal axes are set on the barycentre of the box section. The cross beams are modelled with the geometric parameters described in the Section 3.1.1 with the unknown thickness of the Box and I-section that is hypothesized to fit the first two torsional frequency. They are connected to the equivalent deck axis through rigid links, just like the connection between the box girder axes and the hangers.

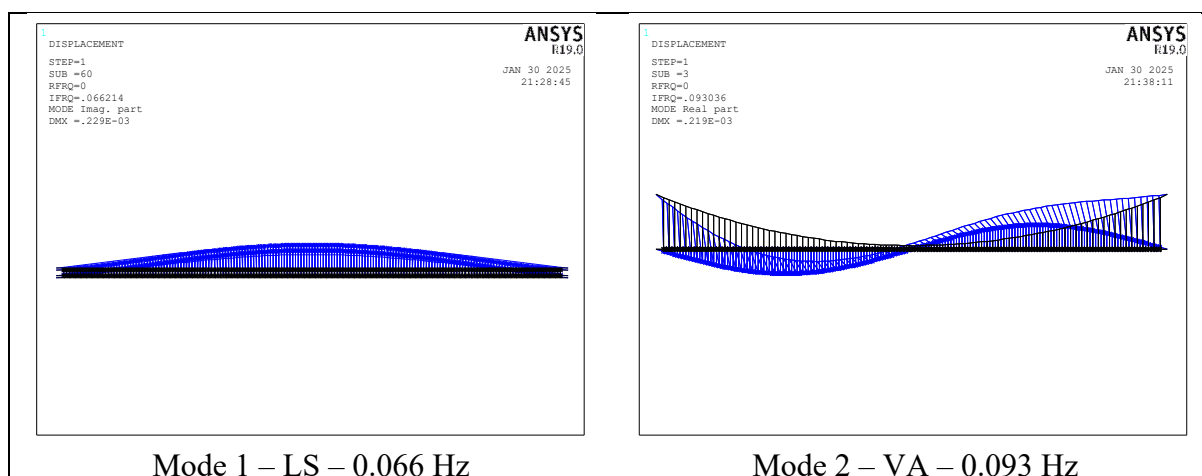
The boundary condition of this model remains unaltered from the previous one (see Section 5.2.2).

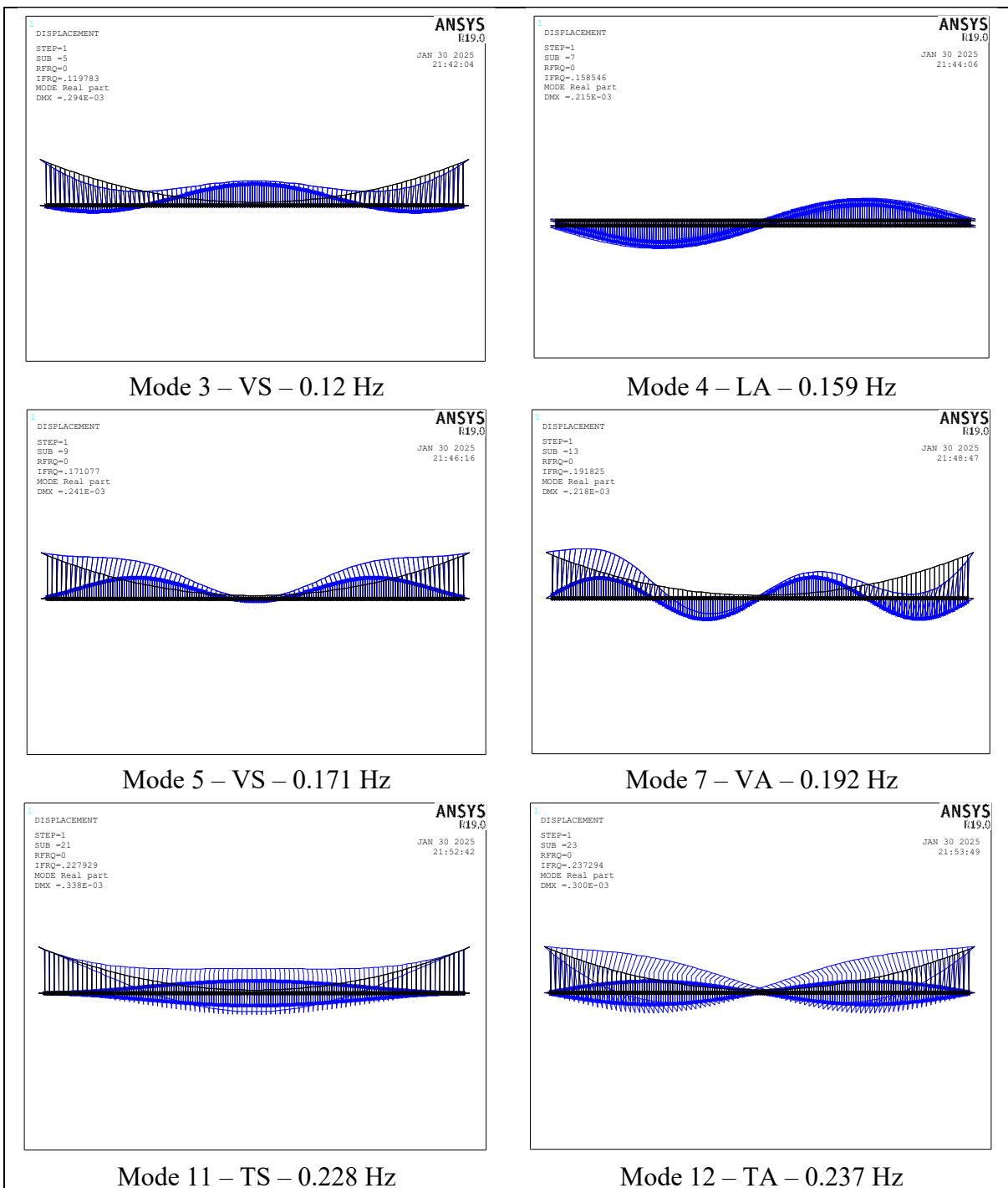
Table 5.4 - Geometrical and mechanical properties of the Xihoumen Bridge

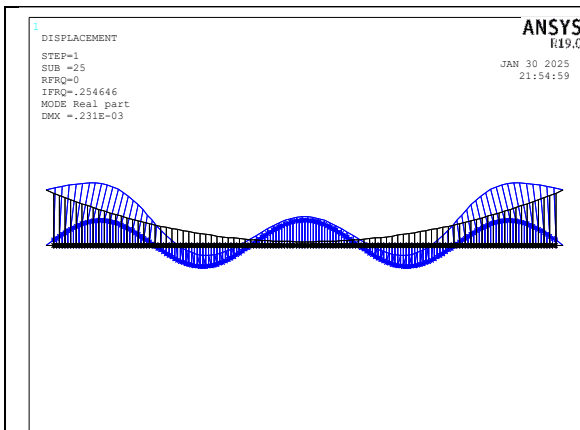
Central span length	$l$ [m]	1650
Sag	$f$ [m]	165
Cable length	$l_{\text{cable}}$ [m]	1692.9
Total deck width	$B$ [m]	36
Distance between cables	$b$ [m]	31.4
Deck density	$\rho_{\text{deck}}$ [ $\text{kg}/\text{m}^3$ ]	19165
Cable density	$\rho_{\text{cable}}$ [ $\text{kg}/\text{m}^3$ ]	6827.8
Hanger density	$\rho_{\text{hanger}}$ [ $\text{kg}/\text{m}^3$ ]	0
Deck area	$A_{\text{deck}}$ [ $\text{m}^2$ ]	1
Cable area	$A_{\text{cable}}$ [ $\text{m}^2$ ]	1.1216
Polar mass moment of inertia per unit length	$I_0$ [ $\text{kgm}^2/\text{m}$ ]	3851136
Equivalent vertical moment of inertia	$I_{z1}$ [ $\text{m}^4$ ]	5
Equivalent lateral moment of inertia	$I_{y1}$ [ $\text{m}^4$ ]	66
Sectorial moment of inertia	$I_{\omega}$ [ $\text{m}^4$ ]	0
Equivalent torsion constant	$I_{t1}$ [ $\text{m}^4$ ]	2.314
Polar mass moment of inertia attributed to M21 elements	$I_{xx, \text{MASS21}}$ [ $\text{kgm}^2$ ]	-6.42E+06
Young's modulus of the deck	$E_{\text{deck}}$ [ $\text{N}/\text{m}^2$ ]	2.1E+11
Young's modulus of the main cables	$E_{\text{cable}}$ [ $\text{N}/\text{m}^2$ ]	1.1E+11
Poisson's ratio of steel	$\nu_{\text{steel}}$	0.3

In the following table (Table 5.5), the most significant mode shapes of the considered model are shown. It can be seen the deformed shape over the undeformed one, underlining the values of the natural frequencies and the typologies of the mode shape.

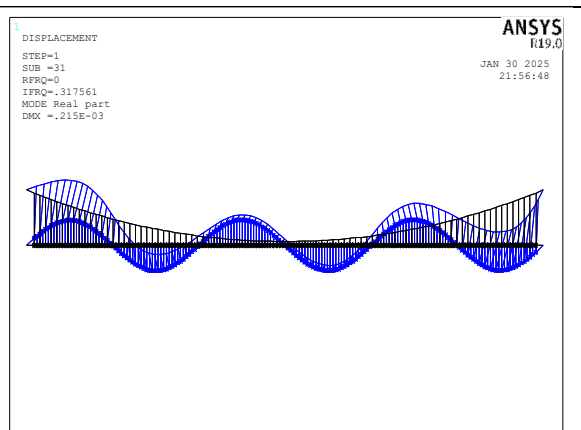
Table 5.5 - Modal frequencies and modal shapes of the Central Span 2-axis Model







Mode 13 – VS – 0.255 Hz



Mode 16 – VA – 0.318 Hz

### 5.2.4 Complete 1-axis model

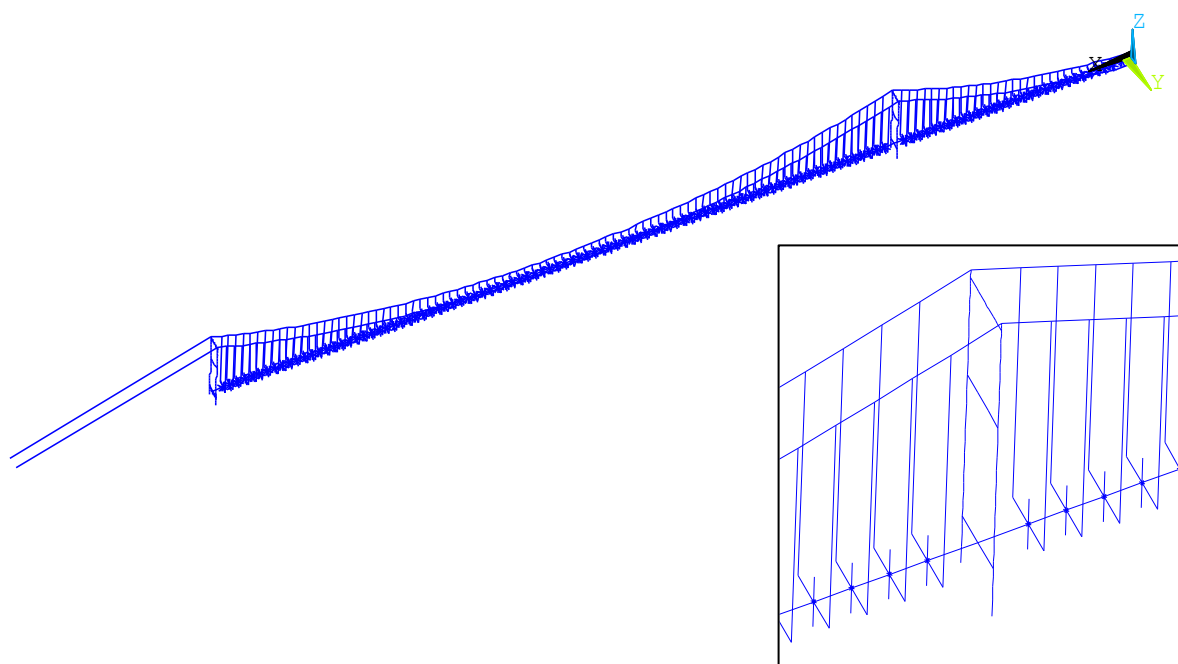


Figure 5.6 - Complete 1-axis FE model with a detail on the right

This model includes lateral spans and towers, with the aim of implementing a more realistic scheme. In particular, with these updates, the external restraints can be removed to the deck and at the connection between main cables and towers. This is because the restraints of the main cables are provided by the inherent rigidity of the towers.

Main cables are connected to the anchors through external hinges.

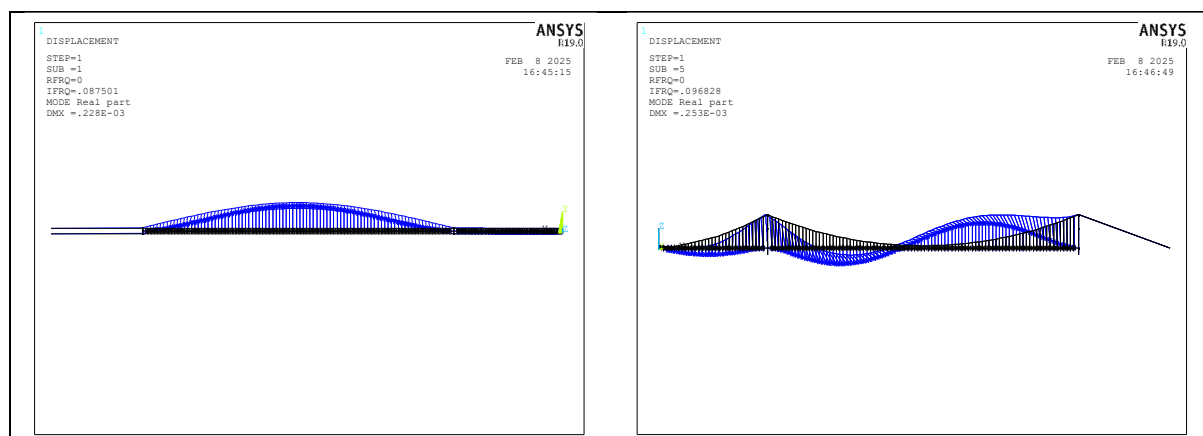
The model was built considering the geometric and mechanical properties of the towers described in Section 3.1.4 as well as the extension of the suspended deck on the northern side span.

Table 5.6 - Geometrical and mechanical properties of the Xihoumen Bridge

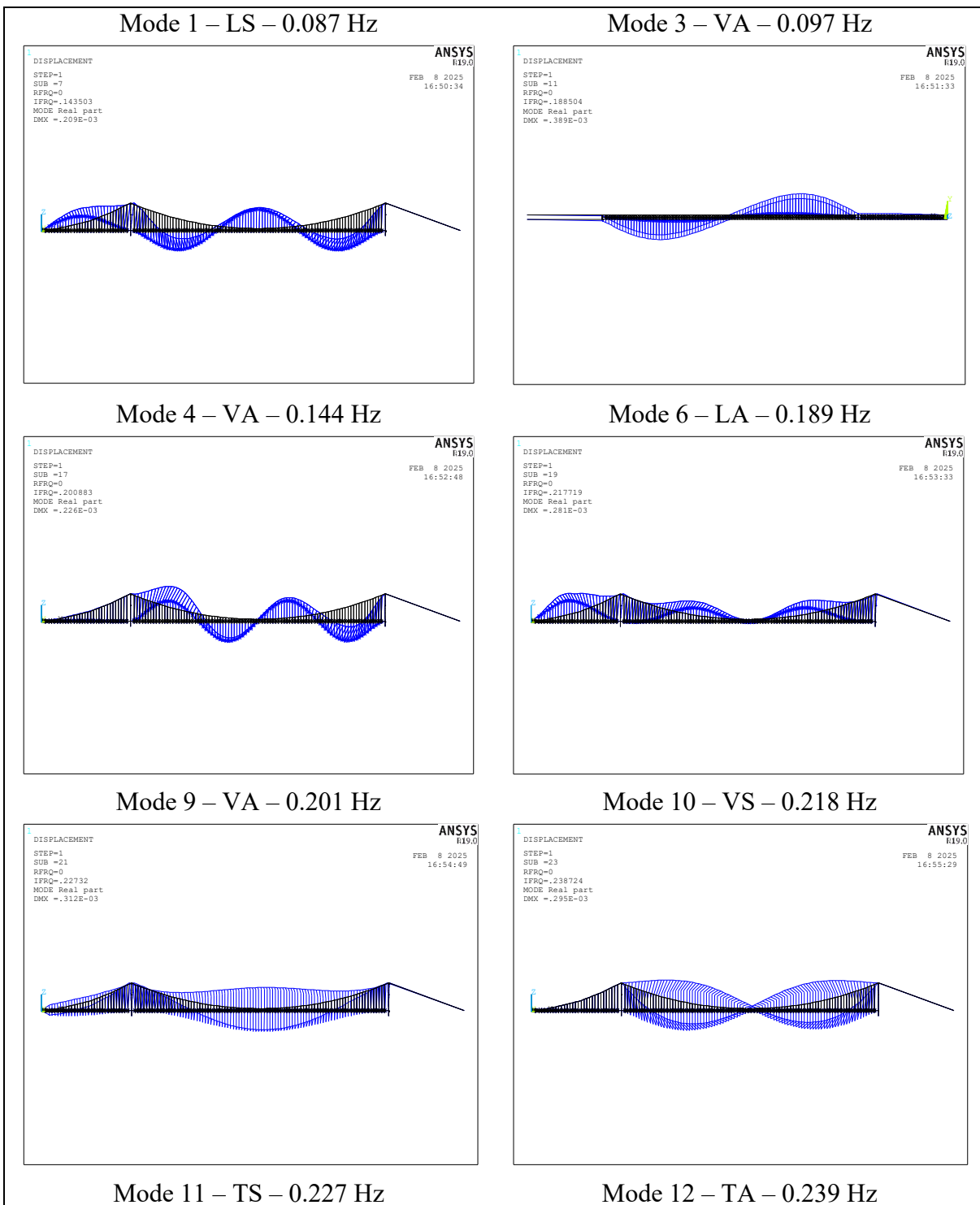
Central span length	$l$ [m]	1650
Lateral nord span length	$l_n$ [m]	578
Sag	$f$ [m]	165
Cable length	$l_{cable}$ [m]	1692.9
Tower height	$h_{tower}$ [m]	211.3
Total deck width	$B$ [m]	36
Distance between cables	$b$ [m]	31.4
Deck density	$\rho_{deck}$ [kg/m <sup>3</sup> ]	19165
Cable density	$\rho_{cable}$ [kg/m <sup>3</sup> ]	6827.8
Tower density	$\rho_{tower}$ [kg/m <sup>3</sup> ]	2549.3
Hanger density	$\rho_{hanger}$ [kg/m <sup>3</sup> ]	0
Deck area	$A_{deck}$ [m <sup>2</sup> ]	1
Cable area (central span)	$A_{cable}$ [m <sup>2</sup> ]	1.1216
Cable area (north span)	$A_{cable,north}$ [m <sup>2</sup> ]	1.1618
Polar mass moment of inertia per unit length	$I_0$ [kgm <sup>2</sup> /m]	3851136
Equivalent vertical moment of inertia	$I_z$ [m <sup>4</sup> ]	10
Equivalent lateral moment of inertia	$I_y$ [m <sup>4</sup> ]	566
Sectorial moment of inertia	$I_\omega$ [m <sup>4</sup> ]	0
Equivalent torsion constant	$I_t$ [m <sup>4</sup> ]	6
Polar mass moment of inertia attributed to M21 elements (central span)	$I_{xx,MASS21}$ [kgm <sup>2</sup> ]	-1.66E+08
Polar mass moment of inertia attributed to M21 elements (north span)	$I_{xx,MASS21,north}$ [kgm <sup>2</sup> ]	-1.76E+08
Young's modulus of the deck	$E_{deck}$ [N/m <sup>2</sup> ]	2.1E+11
Young's modulus of the main cables	$E_{cable}$ [N/m <sup>2</sup> ]	1.9E+11
Young's modulus of the towers	$E_{towers}$ [N/m <sup>2</sup> ]	3.70E+10
Poisson's ratio of steel	$\nu_{steel}$	0.3
Poisson's ratio of concrete	$\nu_{concrete}$	0.2

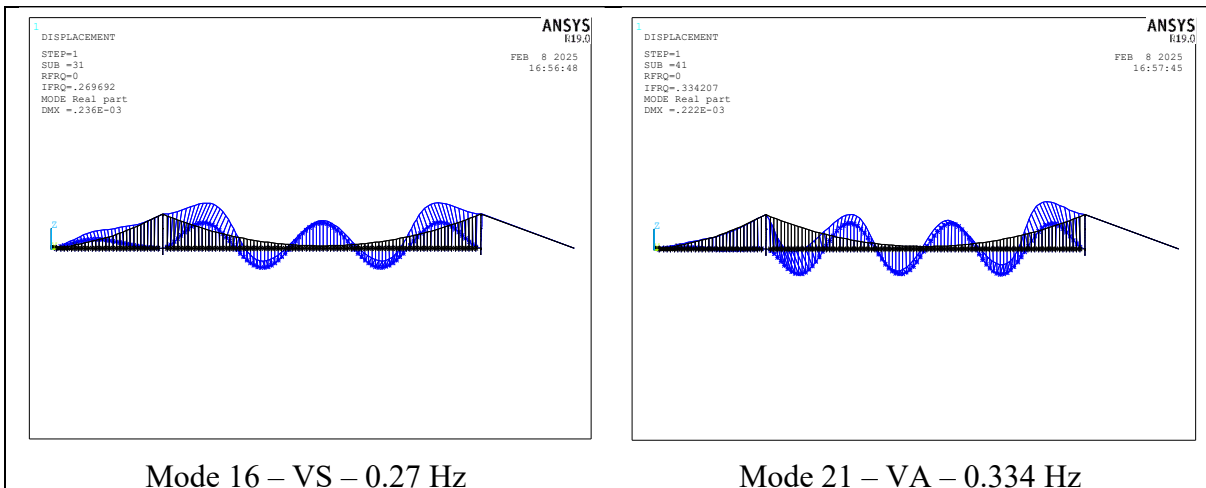
In the following table (Table 5.7) the most significant mode shapes of the considered model are shown. It can be seen the deformed shape over the undeformed one, underlining the values of the natural frequencies and the typologies of the mode shape.

Table 5.7 - Modal frequencies and modal shapes of the Complete 1-axis Model









### 5.2.5 Complete 2-axis model

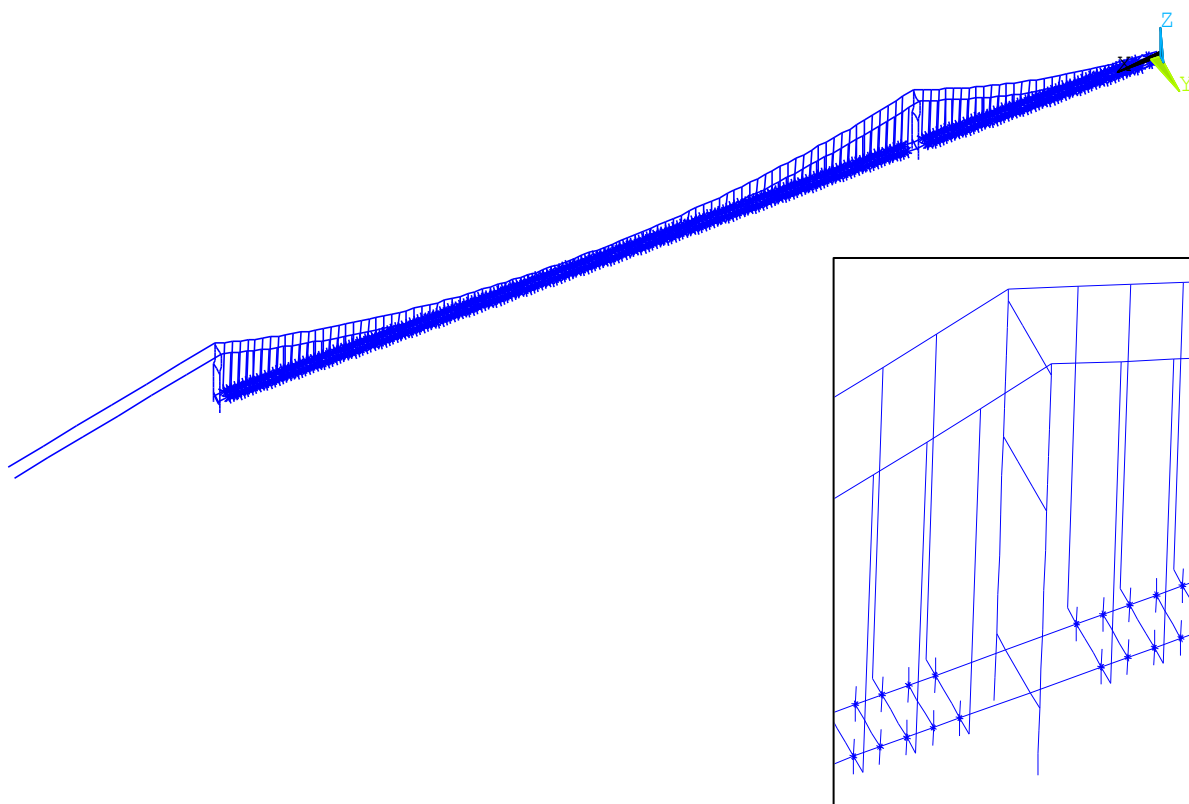


Figure 5.7 - Complete 2-axis FE model with a detail on the right

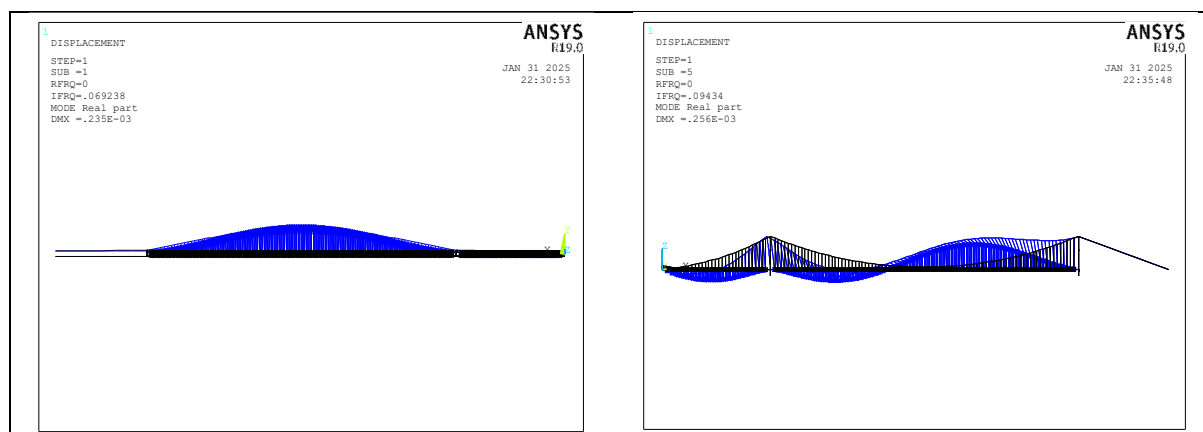
The difference between this model and the one presented in the previous Section (Section 5.2.4) lies in the deck model: instead of a single axis, a two-axis modelling approach is adopted (as done for the central-span model in Section 5.2.2). The boundary conditions of this model remain unaltered from the previous one.

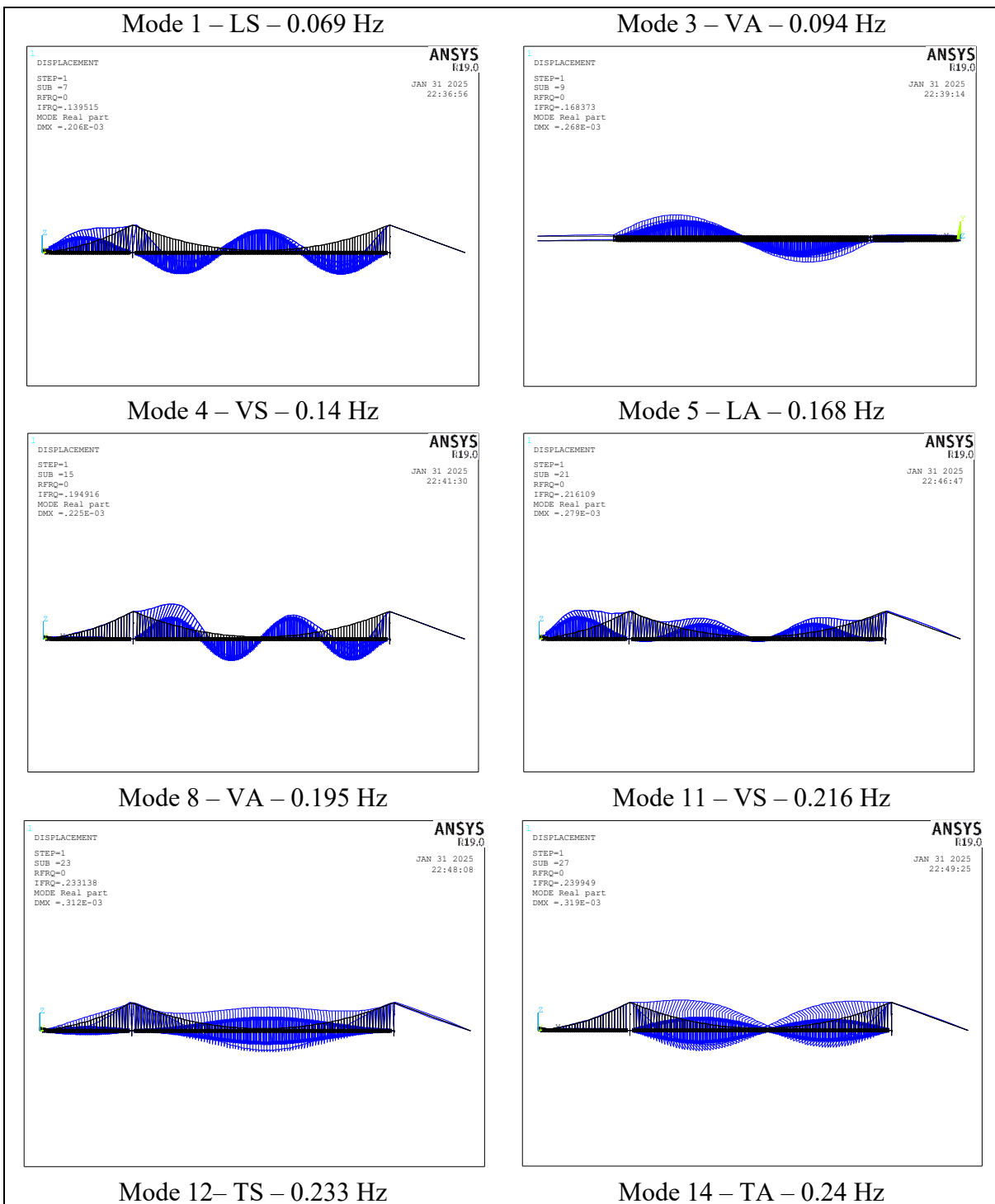
Table 5.8 - Geometrical and mechanical properties of the Xihoumen Bridge

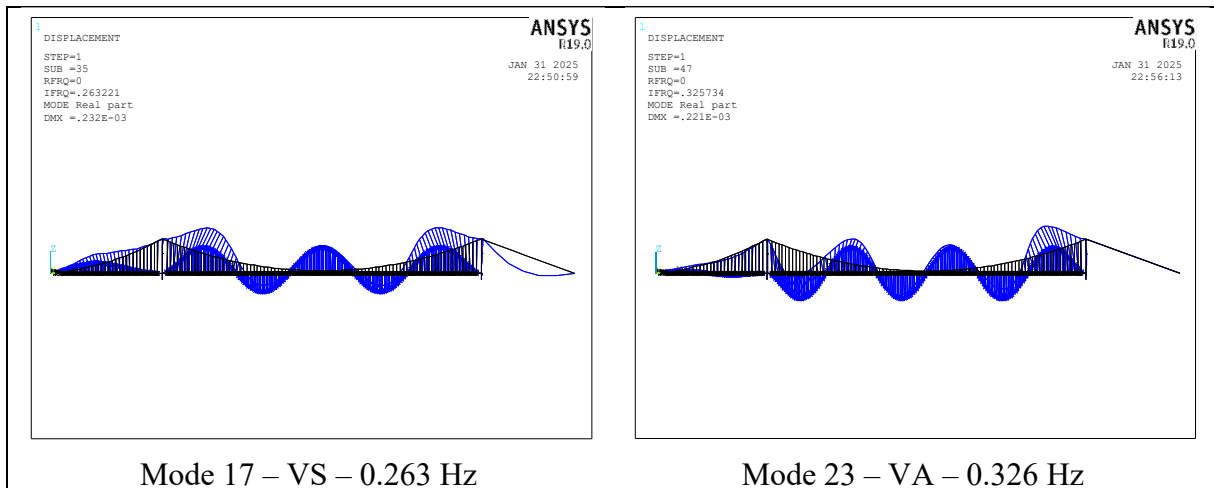
Central span length	$l$ [m]	1650
Lateral nord span length	$l_n$ [m]	578
Sag	$f$ [m]	165
Cable length	$l_{\text{cable}}$ [m]	1692.9
Tower height	$h_{\text{tower}}$ [m]	211.3
Total deck width	$B$ [m]	36
Distance between cables	$b$ [m]	31.4
Deck density	$\rho_{\text{deck}}$ [kg/m <sup>3</sup> ]	19165
Cable density	$\rho_{\text{cable}}$ [kg/m <sup>3</sup> ]	6827.8
Tower density	$\rho_{\text{tower}}$ [kg/m <sup>3</sup> ]	2549.3
Hanger density	$\rho_{\text{hanger}}$ [kg/m <sup>3</sup> ]	0
Deck area	$A_{\text{deck}}$ [m <sup>2</sup> ]	1
Cable area (central span)	$A_{\text{cable}}$ [m <sup>2</sup> ]	1.1216
Cable area (north span)	$A_{\text{cable,north}}$ [m <sup>2</sup> ]	1.1618
Polar mass moment of inertia per unit length	$I_0$ [kgm <sup>2</sup> /m]	3851136
Equivalent vertical moment of inertia	$I_{z1}$ [m <sup>4</sup> ]	5
Equivalent lateral moment of inertia	$I_{y1}$ [m <sup>4</sup> ]	66
Sectorial moment of inertia	$I_{\omega}$ [m <sup>4</sup> ]	0
Equivalent torsion constant	$I_{t1}$ [m <sup>4</sup> ]	2.314
Polar mass moment of inertia attributed to M21 elements (central span)	$I_{xx,\text{MASS21}}$ [kgm <sup>2</sup> ]	-6.42E+06
Polar mass moment of inertia attributed to M21 elements (north span)	$I_{xx,\text{MASS21,north}}$ [kgm <sup>2</sup> ]	-7.28E+06
Young's modulus of the deck	$E_{\text{deck}}$ [N/m <sup>2</sup> ]	2.1E+11
Young's modulus of the main cables	$E_{\text{cable}}$ [N/m <sup>2</sup> ]	1.9E+11
Young's modulus of the towers	$E_{\text{towers}}$ [N/m <sup>2</sup> ]	3.70E+10
Poisson's ratio of steel	$\nu_{\text{steel}}$	0.3
Poisson's ratio of concrete	$\nu_{\text{concrete}}$	0.2

In the following table (Table 5.9) the most significant mode shapes of the considered model are shown. It can be seen the deformed shape over the undeformed one, underlining the values of the natural frequencies and the typologies of the mode shape.

Table 5.9 - Modal frequencies and modal shapes of the Complete 2-axis Model







### 5.3 Comparison with literature results

In this section, the outcomes obtained from the modal analysis performed on the different models previously discussed are compared with literature results. The aim is to evaluate the accuracy and reliability of the proposed models as well as the influence of various modelling approaches on the dynamic properties of the bridge, focusing on natural frequencies and mode shapes.

#### 5.3.1 MATLAB

Table 5.10 – MATLAB Modal frequencies comparison

MATLAB						
Mode	Frequency [Hz]	Type	Jiang <i>et al.</i> [Hz]	Chu <i>et al.</i> [Hz]	%Δ Jiang	%Δ Chu
1	0.089	VA	0.097	0.095	-8.2%	-6.3%
2	0.123	VS	0.133	0.133	-7.5%	-7.5%
3	0.172	VS	0.182	-	-5.5%	-
4	0.191	VA	0.178	0.183	7.3%	4.4%
5	0.225	TS	-	0.229	-	-1.7%
6	0.243	TA	-	0.233	-	4.3%
7	0.253	VS	0.228	-	11.0%	-
8	0.317	VA	0.269	0.276	17.8%	-

In Table 5.10, the natural frequencies obtained with the analytical model in MATLAB are compared with those provided in *Jiang et al.* [25] and *Chu et al.* [23] studies. Errors calculated with respect to the literature results are lower than 10% for the first mode shapes and increase for higher frequencies.

#### 5.3.2 ANSYS – Central span 1-axis model

Table 5.11 - ANSYS – Central span 1-axis model modal frequencies comparison

ANSYS - Central span model 1 axis										
Mode	Frequency [Hz]	Type	MATLAB [Hz]	Jiang <i>et al.</i> [Hz]	Chu <i>et al.</i> [Hz]	Yu <i>et al.</i> [Hz]	%Δ MATLAB	%Δ Jiang	%Δ Chu	%Δ Yu
1	0.056	LS	-	-	-	0.048	-	-	-	16.7%
2	0.093	VA	0.089	0.097	0.095	0.103	4.5%	-4.1%	-2.1%	-9.7%
-	-	VS	-	0.101	-	-	-	-	-	-
3	0.12	VS	0.123	0.133	0.133	-	-2.4%	-9.8%	-9.8%	-
4	0.172	VS	0.172	0.182	-	-	0.0%	-5.5%	-	-
5	0.1722	LA	-	-	-	-	-	-	-	-
6	0.173	local (cable)	-	-	-	-	-	-	-	-
7	0.192	local (cable)	-	-	-	-	-	-	-	-
8	0.193	VA	0.191	0.178	0.183	-	1.0%	8.4%	5.5%	-
9	0.197	local (cable)	-	-	-	-	-	-	-	-
10	0.216	LA	-	-	-	-	-	-	-	-
11	0.223	TS	0.225	-	0.229	0.218	-0.9%	-	-2.6%	2.3%
12	0.243	TA	0.243	-	0.233	-	0.0%	-	4.3%	-
13	0.256	VS	0.253	0.228	-	-	1.2%	12.3%	-	-
14	0.28	LS	-	-	-	-	-	-	-	-
15	0.281	local (cable)	-	-	-	-	-	-	-	-
16	0.319	VA	0.317	0.269	0.276	-	0.6%	18.6%	15.6%	-

In Table 5.11, the results of the first ANSYS model are shown, underlining the differences with literature outcomes. Note that, this model can be compared also to the analytic one, thanks to

the same properties and characteristics of the modelled scheme and external constraints. It can be seen that the results of these two different methods are highly comparable.

Furthermore, the first lateral frequency presents higher error, probably due to the external boundary conditions imposed in the FEM model.

### 5.3.3 ANSYS - Central span 2-axis model

Table 5.12 - ANSYS – Central span 2-axis model modal frequencies comparison

ANSYS - Central span model 2 axis								
Mode	Frequency [Hz]	Type	Jiang <i>et al.</i> [Hz]	Chu <i>et al.</i> [Hz]	Yu <i>et al.</i> [Hz]	%Δ Jiang	%Δ Chu	%Δ Yu
1	0.066	LS	-	-	0.048	-	-	37.5%
2	0.093	VA	0.097	0.095	0.103	-4.1%	-2.1%	-9.7%
-	-		0.101	-	-	-	-	-
3	0.12	VS	0.133	0.133	-	-9.8%	-9.8%	-
4	0.159	LA	-	-	-	-	-	-
5	0.171	VS	0.182	-	-	-6%	-	-
6	0.173	local (cable)	-	-	-	-	-	-
7	0.192	VA	0.178	0.183	-	7.9%	4.9%	-
8	0.194	L+local	-	-	-	-	-	-
9	0.197	local (cable)	-	-	-	-	-	-
10	0.211	L+local	-	-	-	-	-	-
11	0.228	TS	-	0.229	0.218	-	-0.4%	4.6%
12	0.237	TA	-	0.233	-	-	1.7%	-
13	0.255	VS	0.228	-	-	11.8%	-	-
14	0.272	L+local	-	-	-	-	-	-
15	0.281	local (cable)	-	-	-	-	-	-
16	0.318	VA	0.269	0.276	-	18.2%	15.2%	-

This model is realized with the aim of reach more reliability and accuracy according to the presence of twin box girders. Results are pretty similar to the previous model, with errors calculated with respect to literature that are lower than 10-15%, except for higher frequencies. Furthermore, the lateral frequencies have higher differences with literature values; this can be due to the hypothesis done for the cross beams in Section 5.2.2.



### 5.3.4 ANSYS - Complete 1-axis model

Table 5.13 - ANSYS – Complete 1-axis model modal frequencies comparison

ANSYS - Complete model 1 axis								
Mode	Frequency [Hz]	Type	Jiang <i>et al.</i> [Hz]	Chu <i>et al.</i> [Hz]	Yu <i>et al.</i> [Hz]	%Δ Jiang	%Δ Chu	%Δ Yu
1	0.087	LS	-	-	0.048	-	-	81.3%
2	0.094	Asymm	-	-	-	-	-	-
3	0.097	VA	0.097	0.095	0.103	0.0%	2.1%	-5.8%
-	-	VS	0.101	-	-	-	-	-
4	0.144	VS	0.133	0.133	-	8.3%	8.3%	-
5	0.173	local (cable)	-	-	-	-	-	-
6	0.189	LA	-	-	-	-	-	-
7	0.196	LS	-	-	-	-	-	-
8	0.198	local (cable)	-	-	-	-	-	-
9	0.201	VA	0.178	0.183	-	12.9%	9.8%	-
10	0.218	VS	0.182	-	-	19.8%	-	-
11	0.227	TS	-	0.229	0.218	-	-0.9%	4.1%
12	0.239	TA	-	0.233	-	-	2.6%	-
13	0.24	LS (lat. Span)	-	-	-	-	-	-
14	0.248	local (cable)	-	-	-	-	-	-
15	0.265	LA	-	-	-	-	-	-
16	0.27	VS	0.228	-	-	18.4%	-	-
17	0.279	LS	-	-	-	-	-	-
18	0.281	local (cable)	-	-	-	-	-	-
19	0.313	VA (lat. Span)	-	-	-	-	-	-
20	0.328	LA	-	-	-	-	-	-
21	0.334	VA	0.269	0.276	-	24.2%	21.0%	-

With this model, boundary conditions change to reach more reliability in terms of external constraints, in particular between main cables and towers, that now are modelled. Although the errors with respect to literature's values are not too high, the results are different than the previous central models. This may be attributed to the incomplete literature data on the towers' characteristics and their connection with the main cables, which led to formulate several modelling assumptions to compensate for these gaps.

It can be noted that the second symmetric vertical mode has an error that is near to the 20%.

### 5.3.5 ANSYS – Complete 2-axis model

Table 5.14 - ANSYS – Complete 2-axis model modal frequencies comparison

ANSYS - Complete model 2 axis								
Mode	Frequency [Hz]	Type	Jiang <i>et al.</i> [Hz]	Chu <i>et al.</i> [Hz]	Yu <i>et al.</i> [Hz]	%Δ Jiang	%Δ Chu	%Δ Yu
1	0.069	LS	-	-	0.048	-	-	43.8%
2	0.092	Asymm	-	-	-	-	-	-
3	0.094	VA	0.097	0.095	0.103	-3.1%	-1.1%	-8.7%
-	-		0.101	-	-	-	-	-
4	0.14	VS	0.133	0.133	-	5.3%	5.3%	-
5	0.168	LA	-	-	-	-	-	-
6	0.173	local (cable)	-	-	-	-	-	-
7	0.192	L+local	-	-	-	-	-	-
8	0.195	VA	0.178	0.183	-	9.6%	6.6%	-
9	0.198	local (cable)	-	-	-	-	-	-
10	0.214	LA	-	-	-	-	-	-
11	0.216	VS	0.182	-	-	18.7%	-	-
12	0.233	TS	-	0.229	0.218	-	1.7%	6.9%
13	0.239	tors+local	-	-	-	-	-	-
14	0.24	TA	-	0.233	-	-	3.0%	-
15	0.251	local (cable)	-	-	-	-	-	-
16-16a	0.26	local	-	-	-	-	-	-
17	0.263	VS	0.228	-	-	15.4%	-	-
18	0.27	local	-	-	-	-	-	-
19	0.281	local	-	-	-	-	-	-
20	0.289	local	-	-	-	-	-	-
21	0.314	local	-	-	-	-	-	-
22	0.324	local	-	-	-	-	-	-
23	0.326	VA	0.269	0.276	-	21%	18.1%	-

It should be noted that this is the most complex and accurate model, requiring a larger amount of data, some of which was not available in the literature.

In this model, as in the previous one, the difference between results is marked.

As is possible to see in all models, the lateral frequencies have greater deviations with respect to the others. This can be due to the external lateral restraints assumed for the model. Nevertheless, these errors will not generate too much randomness in flutter analysis since, in the analysed case study, flutter is expected to be triggered by the interaction between vertical and torsional modes.

### 5.3.6 Results summary

In conclusion, it is noticed that the best models used to fit the natural frequencies of the bridge, and in general to perform the modal analysis, are the central span ones. This is due to fewer hypotheses and assumptions done and for the higher assurance in the input data.

In particular, the 1-axis central span model gives more certainty due to the non-presence of hypothesized cross beams and due to the use of literature data of the moment of inertia.

## Chapter 6 - Xihoumen Bridge flutter analysis

### 6.1 Flutter analysis in MATLAB

As described in Section 2.5, in this paragraph the flutter analysis is performed considering the different sets of flutter derivatives presented in Chapter 4.

#### 6.1.1 Experimental flutter derivatives

In the graphs below (Figures 6.1 and 6.2), curves of the real part of the eigenvalues (related to the modal damping) and the imaginary ones (related to the modal frequency) are plotted for increasing values of wind speed.

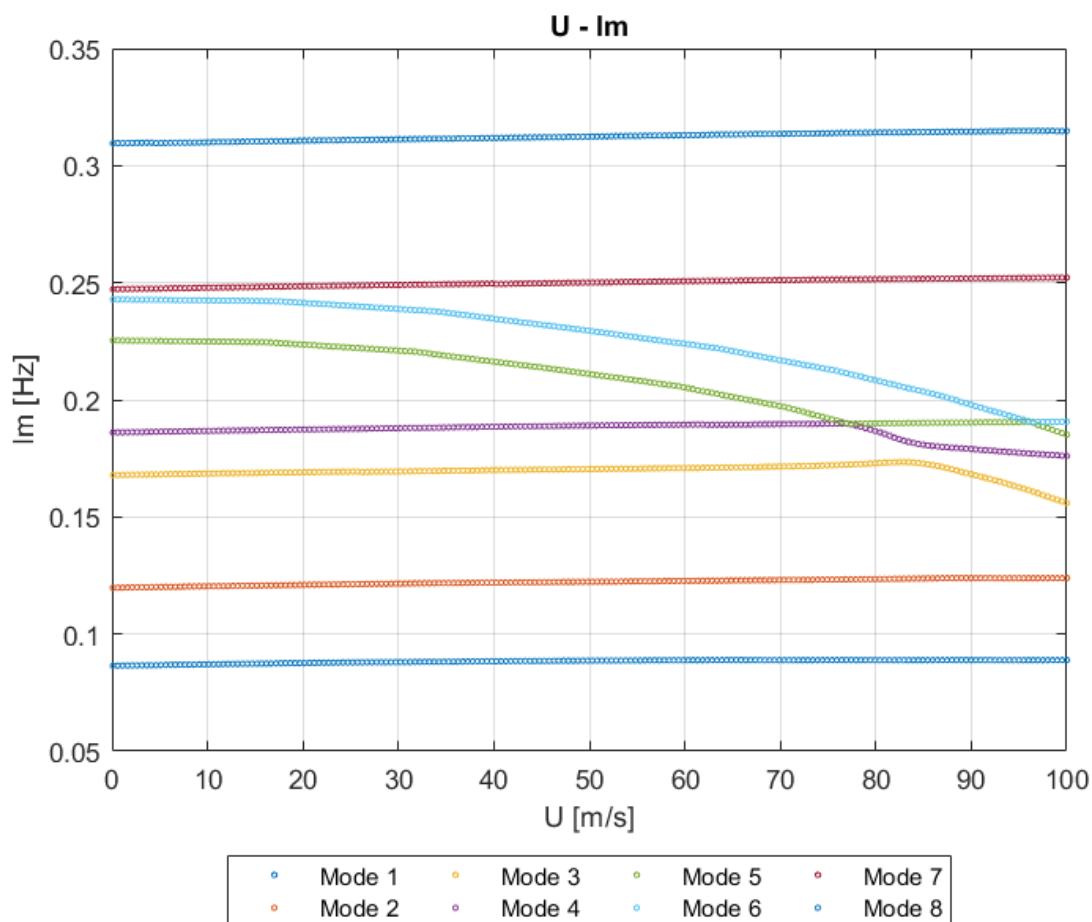


Figure 6.1 - Variation of the imaginary part of complex eigenvalues

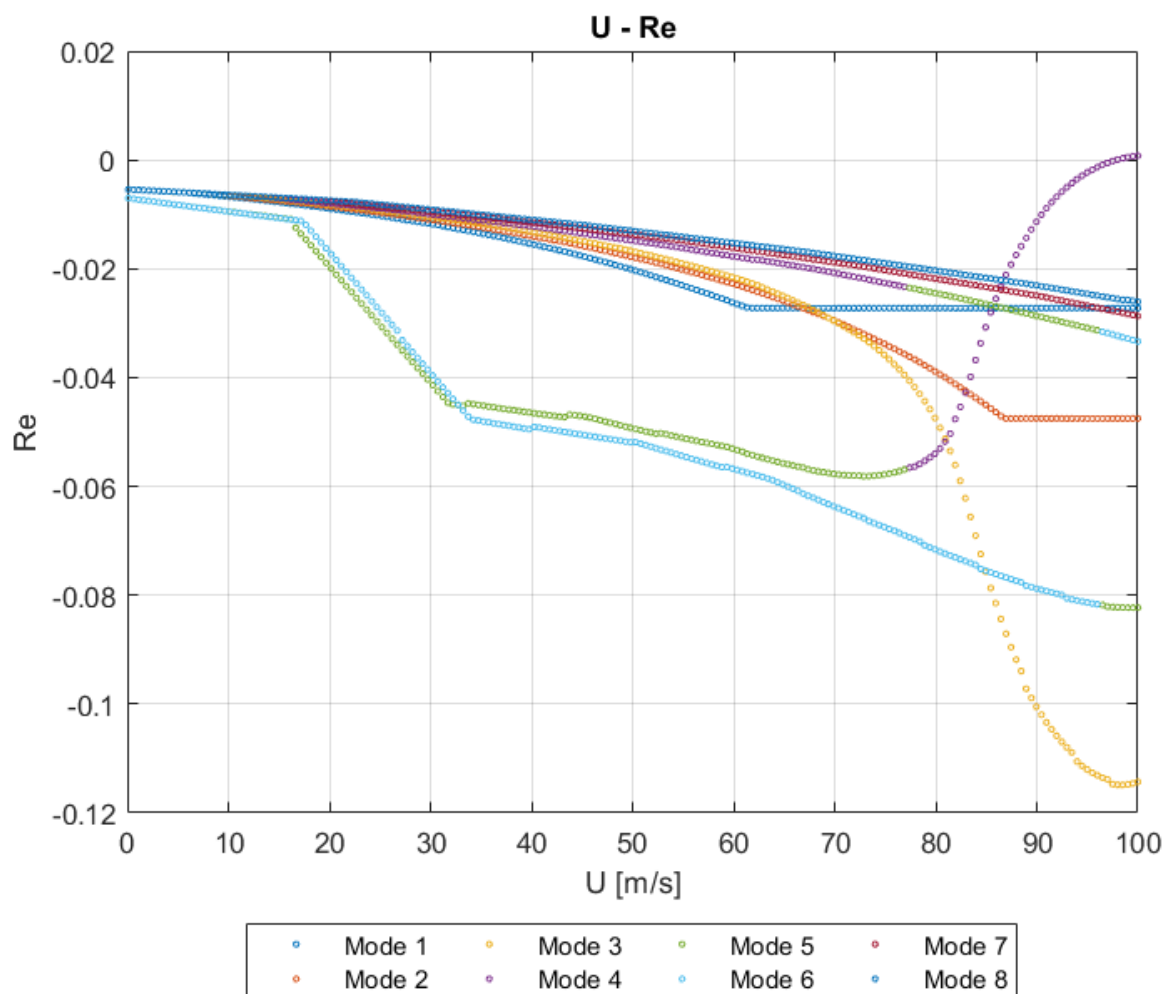


Figure 6.2 - Variation of the real part of complex eigenvalues

The real part of the eigenvalue corresponding to the fifth mode (at the free-wind condition) becomes positive at the critical wind speed of 97.5 m/s and at a flutter frequency of 0.177 Hz. This mode is the one that at null wind velocity has purely torsional symmetric deformed shape. But, contrary to what one might think by looking at graphs, the flutter phenomenon is not only activated by the torsional mode. As the wind speed increases, the modal shape changes along with the eigenvalues; in fact, the interaction between vertical and torsional degrees of freedom (as it can be seen in Figure 6.3) is what leads to flutter instability: in this case due to the interaction between the second symmetric vertical mode and the first symmetric torsional one.

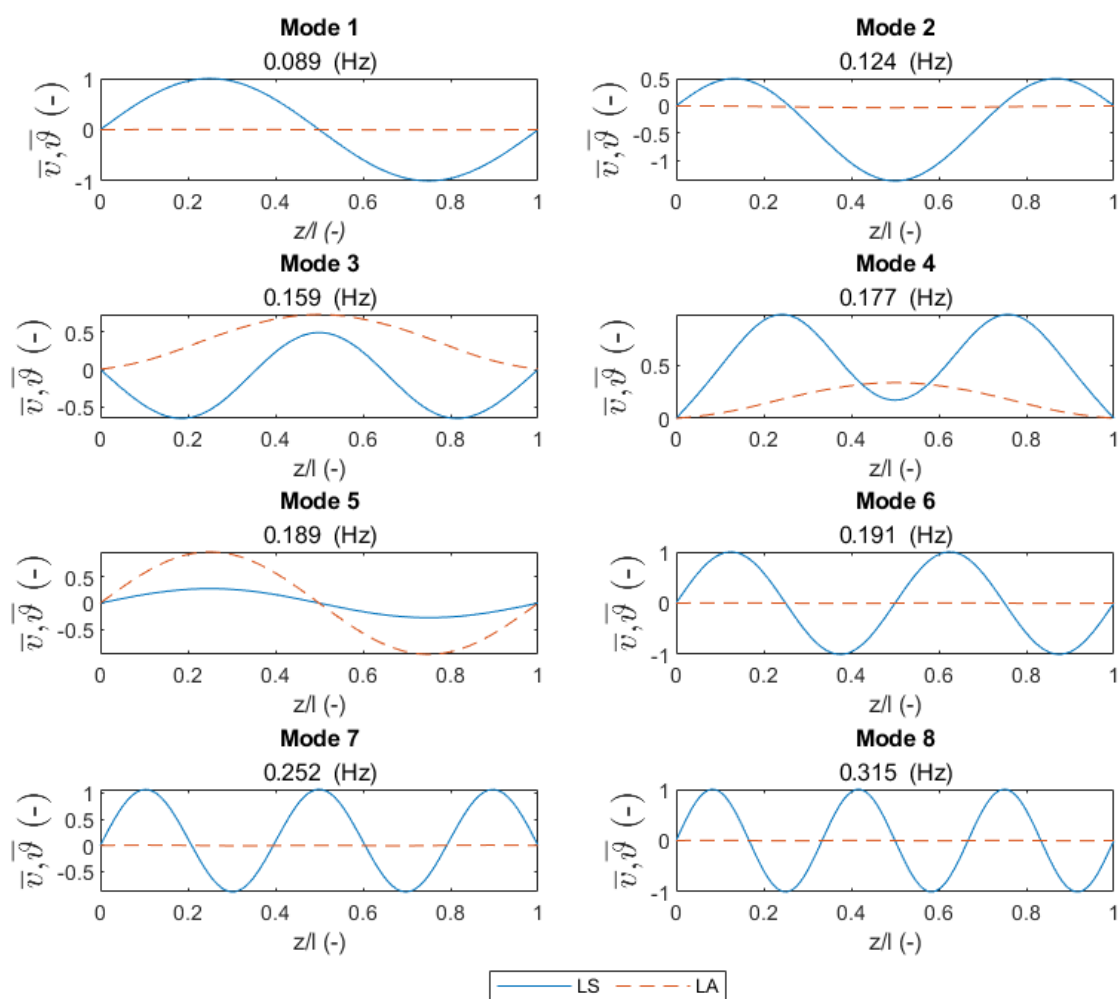


Figure 6.3 - Xihoumen Bridge modal shapes in critical flutter condition

### 6.1.2 Andersen's flutter derivatives

In this analysis, analytical flutter derivatives obtained with the superposition of flat plates method (Section 4.2) are used to estimate the critical value of wind speed and structural frequency. The results of flutter analysis are shown in Figures 6.4 and 6.5.

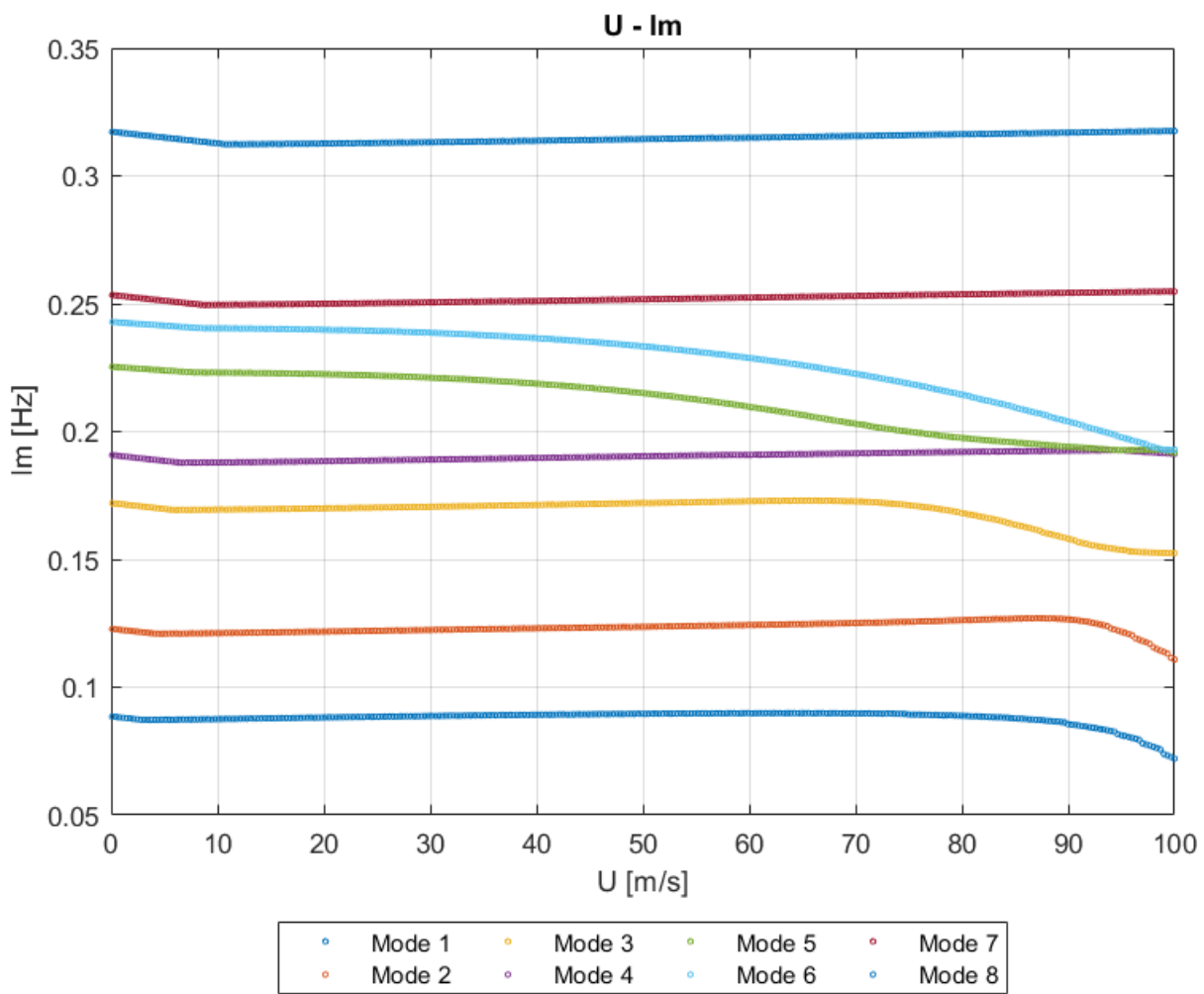


Figure 6.4 - Variation of the imaginary part of complex eigenvalues

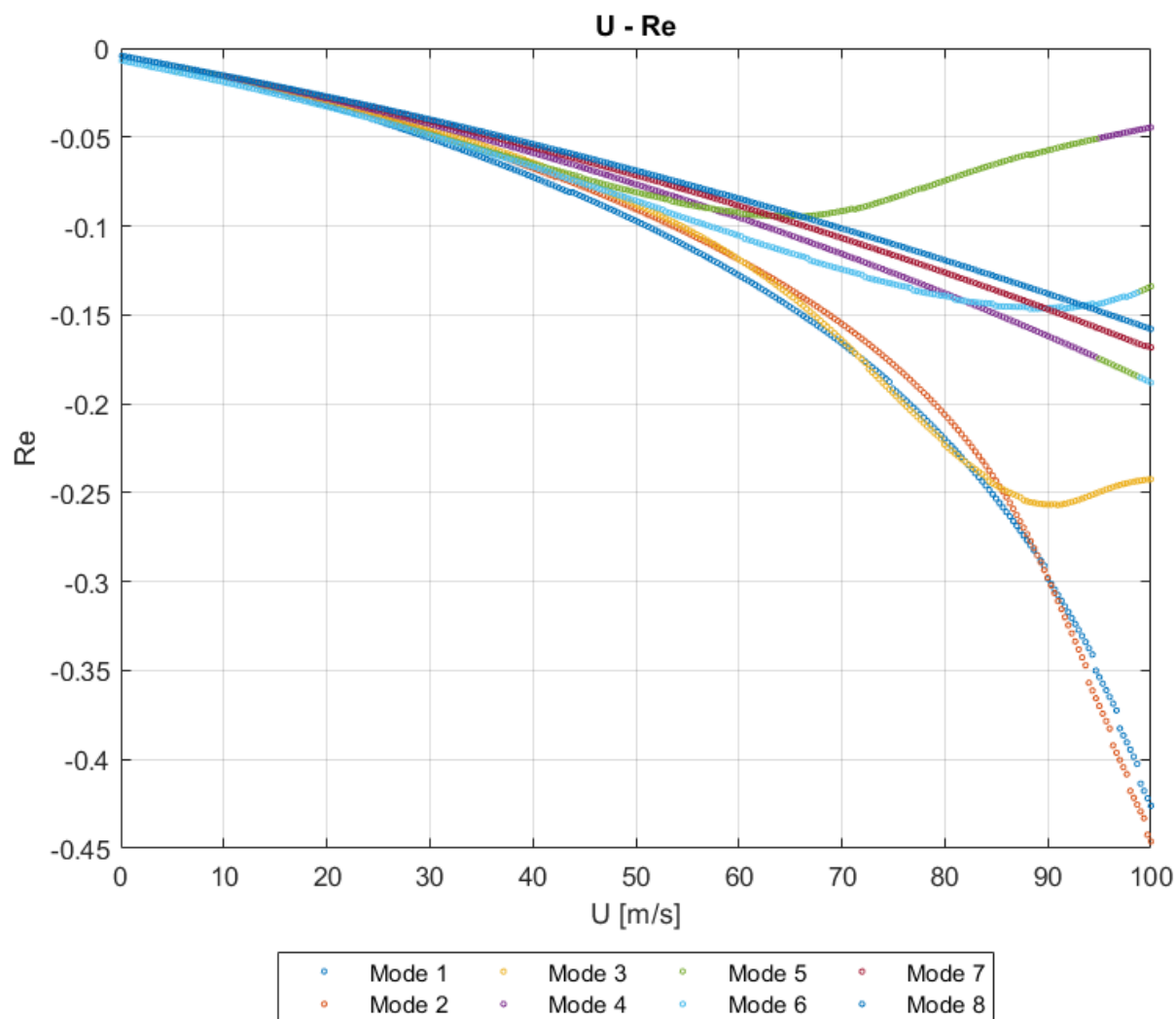


Figure 6.5 - Variation of the real part of complex eigenvalues

As it could be expected, the analysis did not produce a critical flutter wind speed in the speed range investigated. In fact, as pointed out by the authors [27], the use of this analytical derivatives without the correction factor tends to overestimate the critical values of flutter instability.

### 6.1.3 Andersen's flutter derivatives with gap-width scaling factor

The analysis is performed considering the coefficient discussed in Section 4.2.1, with the aim of contrasting the overestimation of the previous case.

Results are shown in Figures 6.6 and 6.7.

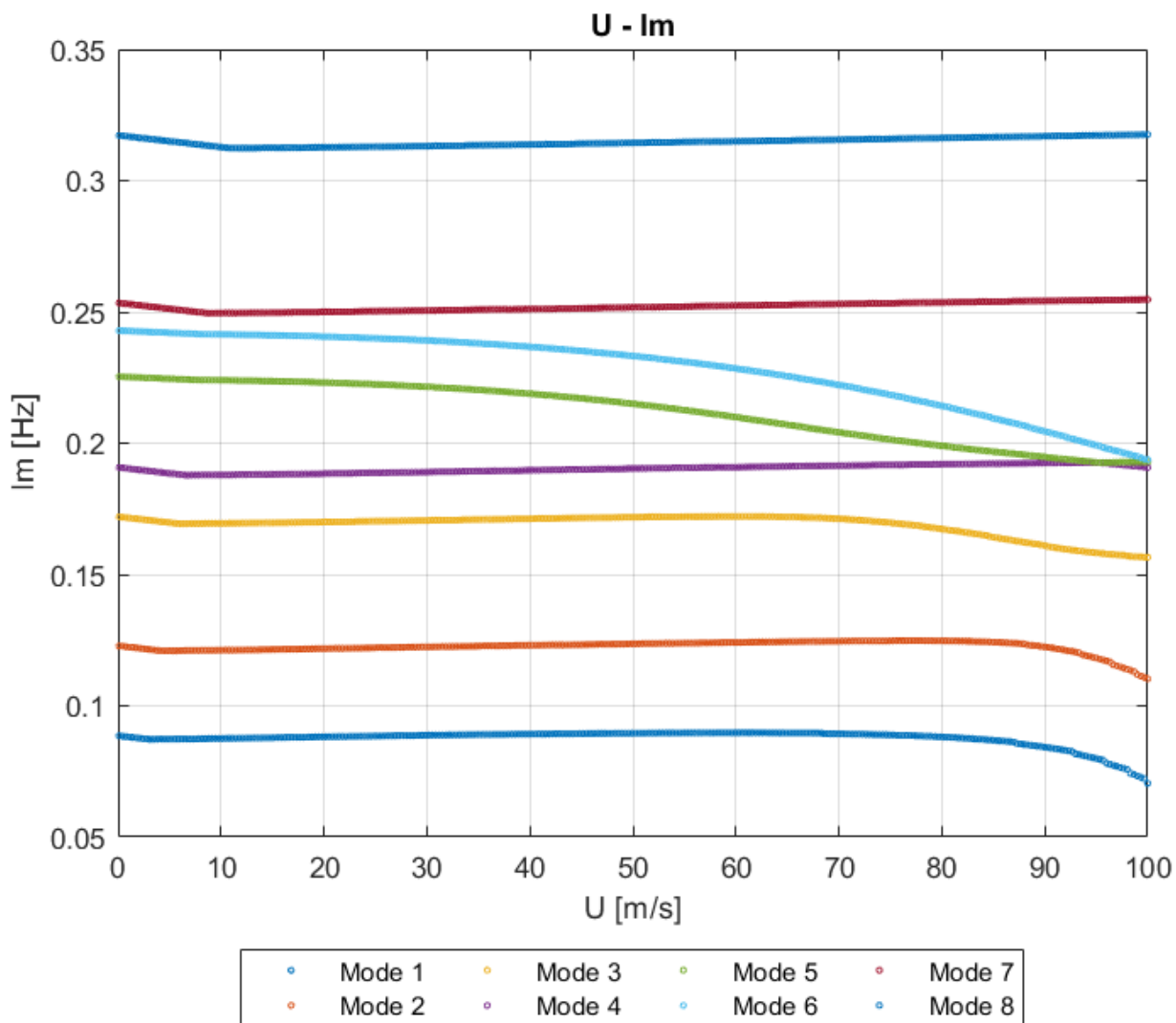


Figure 6.6 - Variation of the imaginary part of complex eigenvalues



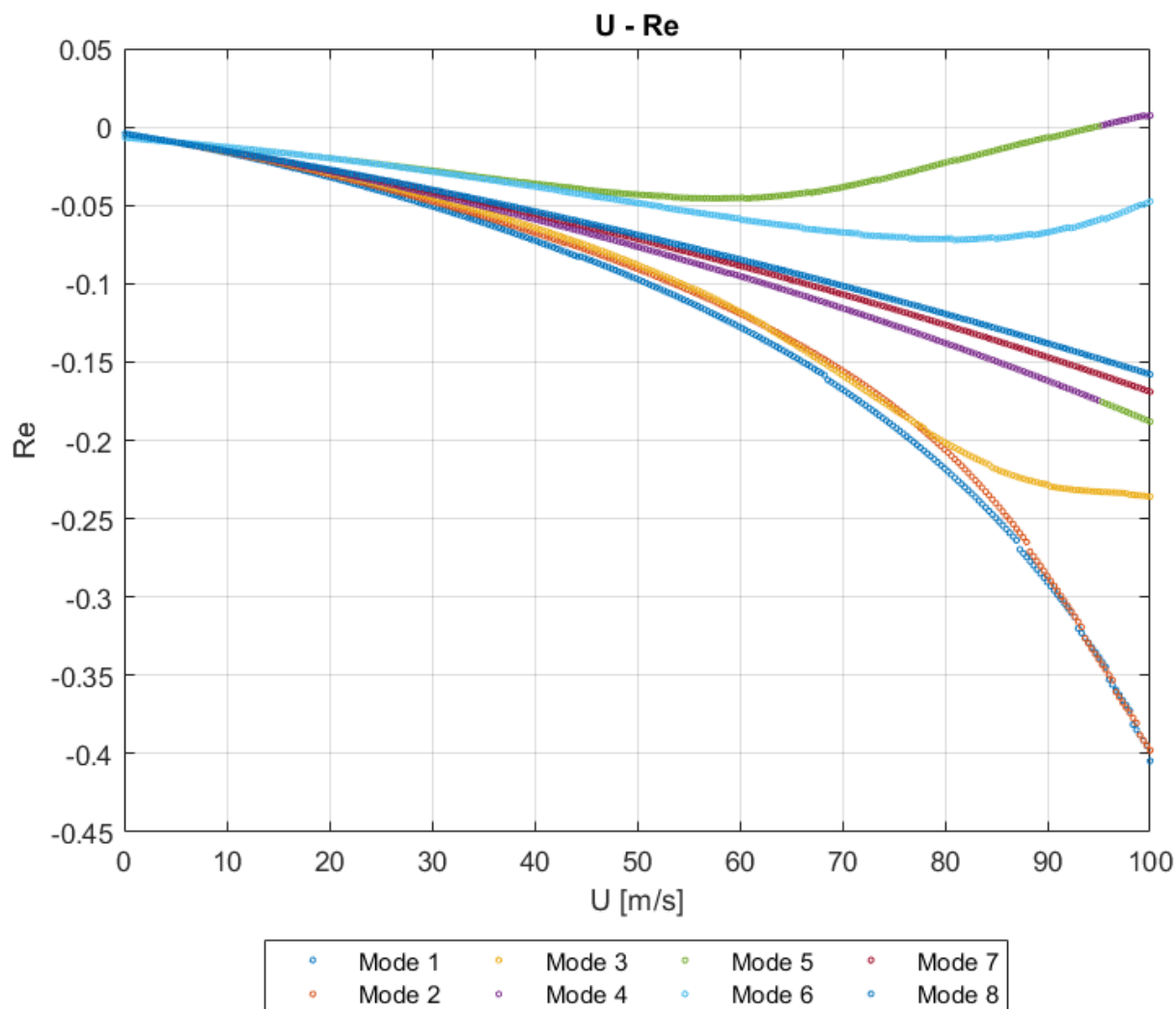


Figure 6.7 - Variation of the real part of complex eigenvalues

The real part of the eigenvalue corresponding to the fifth mode becomes positive at the critical wind speed of 94.7 m/s and at a flutter frequency of 0.193 Hz. This mode is the one that at null wind velocity has purely torsional symmetric deformed shape.

The results suggest that incorporating the gap-width scaling factor may help mitigate the overestimation of flutter analysis outcomes when using Andersen's simplified method for calculating flutter derivatives.

#### 6.1.4 Results comparison

In this section are shown the differences between the cases, discussed in Sections 6.1.1, 6.1.2 and 6.1.3, in terms of numerical results. In Table 6.1, where present, the critical values of instability are presented.

Table 6.1 - MATLAB Flutter Analysis, result comparison

Flutter derivatives	MATLAB			
	U_cr [m/s]	f_cr [Hz]	%Δ U_experimental	%Δ f_experimental
Experimental	97.5	0.177	-	-
Andersen	>100	-	-	-
Andersen with $\mu=0.7$	94.7	0.193	-2.9%	9.0%

As it is clear from the Table 6.1, it is interesting to compare the results obtained considering experimental flutter derivatives with the same found using the reduced Andersen's flutter derivatives. This comparison shows similarity in the results, and this could be object of more studies.

## 6.2 Flutter analysis of central-span models in ANSYS

The damped complex eigenvalue analyses were conducted on the central span models under wind velocities ranging from 0 to 100 m/s (0 to 360 km/h). The incremental step of wind velocity was set variable, from a standard value of 10 m/s to a minimum of 1 m/s when the instability was expected.

The computational steps described in Section 2.6 have been followed for the two modes involved in the coupled-mode flutter instability: the first symmetric torsional one and the second symmetric vertical one.

As done for the analytic model in Section 6.1, the Flutter Analyses were conducted using different flutter derivatives and for the models described in Section 5.2.

### 6.2.1 Single-axis model

#### 6.2.1.1 Experimental flutter derivatives

The results obtained for the central span 1-axis model using experimental flutter derivatives are plotted below (Figures 6.8 and 6.9).

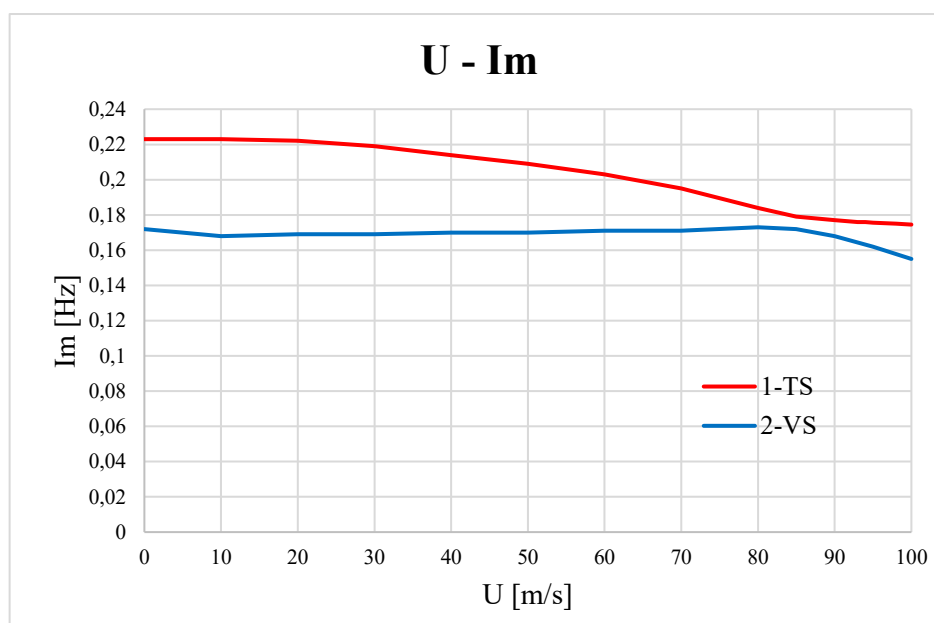


Figure 6.8 - Variation of the imaginary part of complex eigenvalues

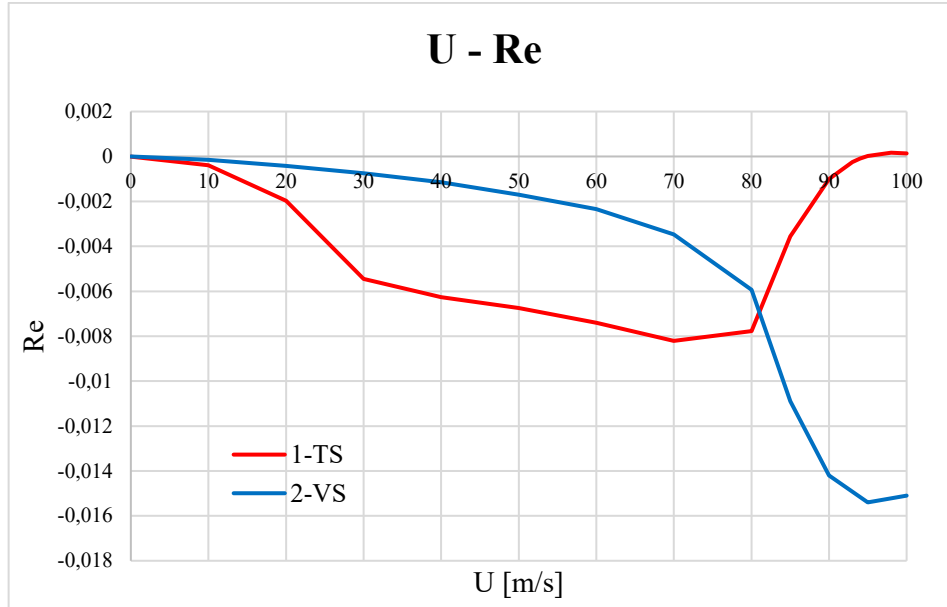


Figure 6.9 - Variation of the real part of complex eigenvalues

The flutter condition occurs when the real part, related to the modal damping, becomes null, and the corresponding wind velocity is the critical flutter wind velocity. Hence, the analysis produced a critical wind speed of 95 m/s and a corresponding critical frequency of 0.1756 Hz. This wind speed of 342 km/h is significantly higher than the maximum design wind speed of 148.032 km/h (41.12 m/s) for a return period of 100 years over the Zhoushan Archipelago in the East China Sea [19], and it also exceeds the stability requirement of 282.4 km/h (78.4 m/s) [19] by a considerable margin.

As seen in the analytical analysis in MATLAB, contrary to what can be deduced from the analysis output, the torsional mode itself doesn't initiate the flutter instability: the increase of wind velocity causes a variation of modal shape associated with the variation of the eigenvalues, in fact flutter instability is caused by the interaction between modes. Figure 6.10 shows how torsional and vertical degrees of freedom are coupled together when the flutter condition is approached.

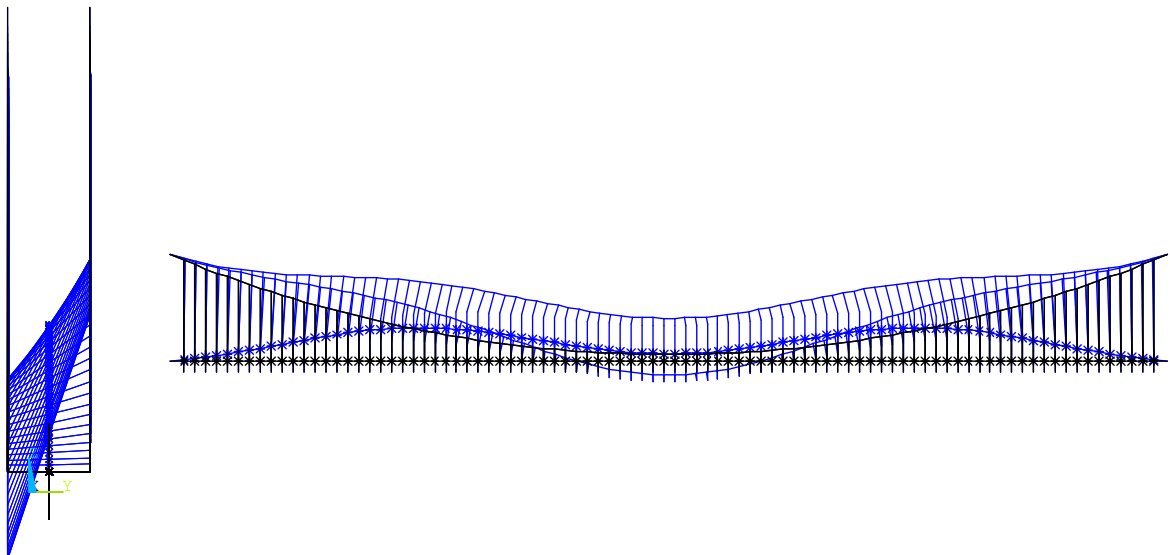


Figure 6.10 - Deformed shape at flutter critical condition

### 6.2.1.2 Andersen's flutter derivatives

In this section, analytical flutter derivatives obtained with the superposition of flat plates theory (Section 4.2) are used to estimate the critical value of the velocity and frequency.

The evolution of real and imaginary parts of the coupling eigenvalues are shown in Figures 6.11 and 6.12.

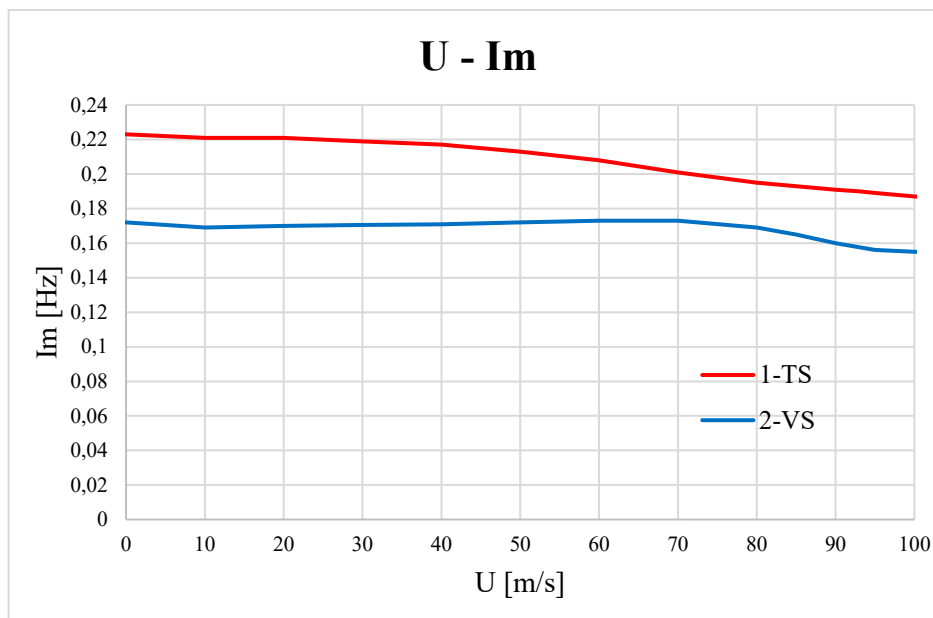


Figure 6.11 - Variation of the imaginary part of complex eigenvalues

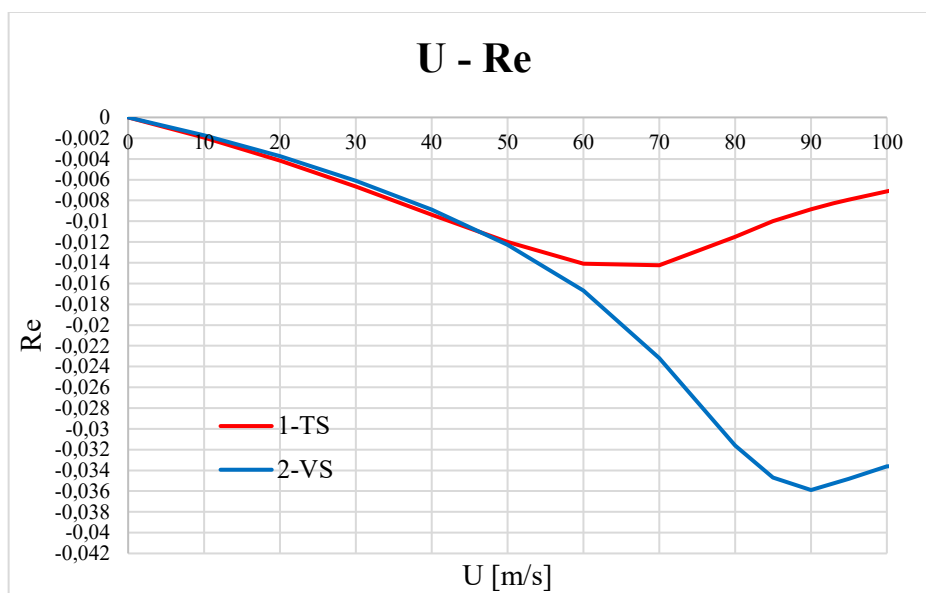


Figure 6.12 - Variation of the real part of complex eigenvalues

The analysis did not detect a critical flutter wind speed in the speed range investigated.

This was expected, as in MATLAB analysis, due to the possible overestimation of aeroelastic instability using such simplified approach for the flutter derivatives estimation.

### 6.2.1.3 Andersen's flutter derivatives with gap-width scaling factor

The analysis is performed considering the coefficient discussed in Section 4.2.1, to contrast the overestimation of the previous case.

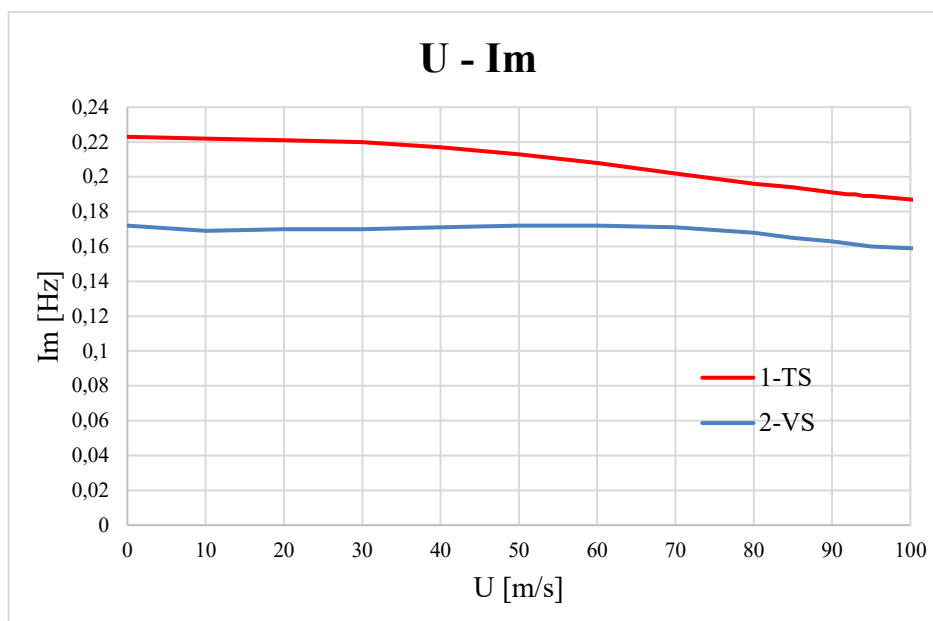


Figure 6.13 - Variation of the imaginary part of complex eigenvalues

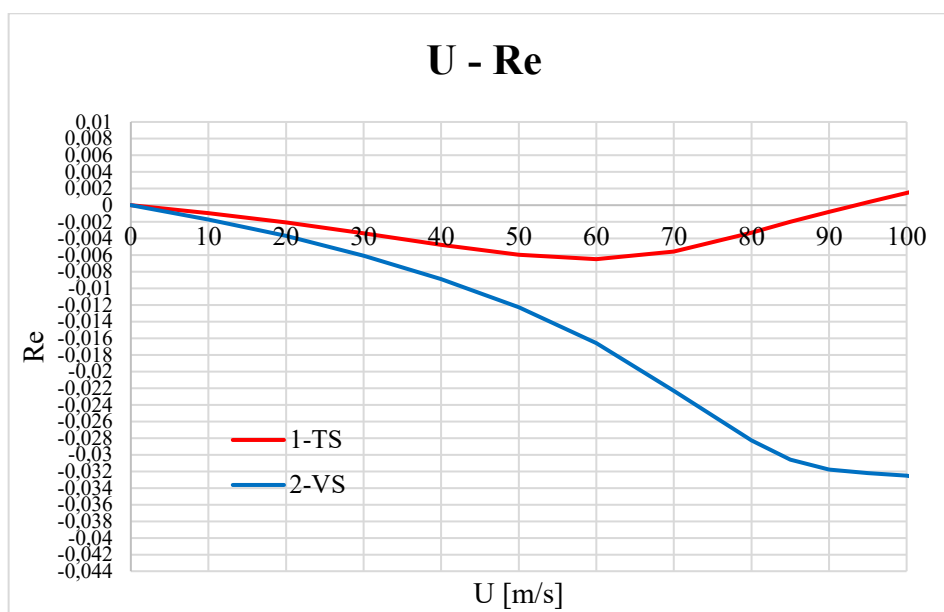


Figure 6.14 - Variation of the real part of complex eigenvalues

The analysis led to a flutter wind speed of 94 m/s and a corresponding critical frequency of 0.189 Hz.

## 6.2.2 Double-axis model

The analysis is performed using Theodorsen's flutter derivatives, as described in Section 4.1, applied separately to the longitudinal axes of each box.

### 6.2.2.1 Theodorsen's flutter derivatives

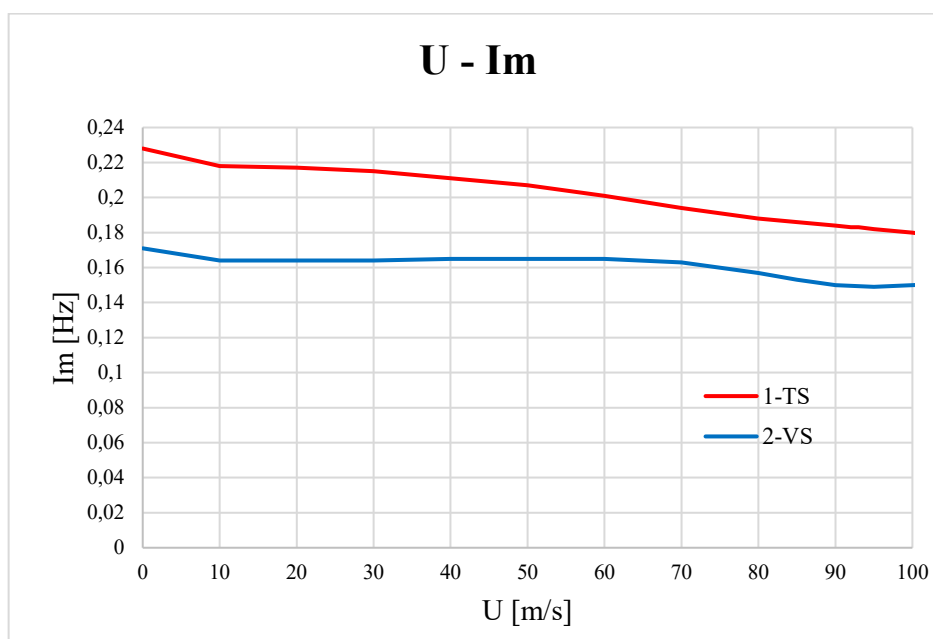


Figure 6.15 - Variation of the imaginary part of complex eigenvalues

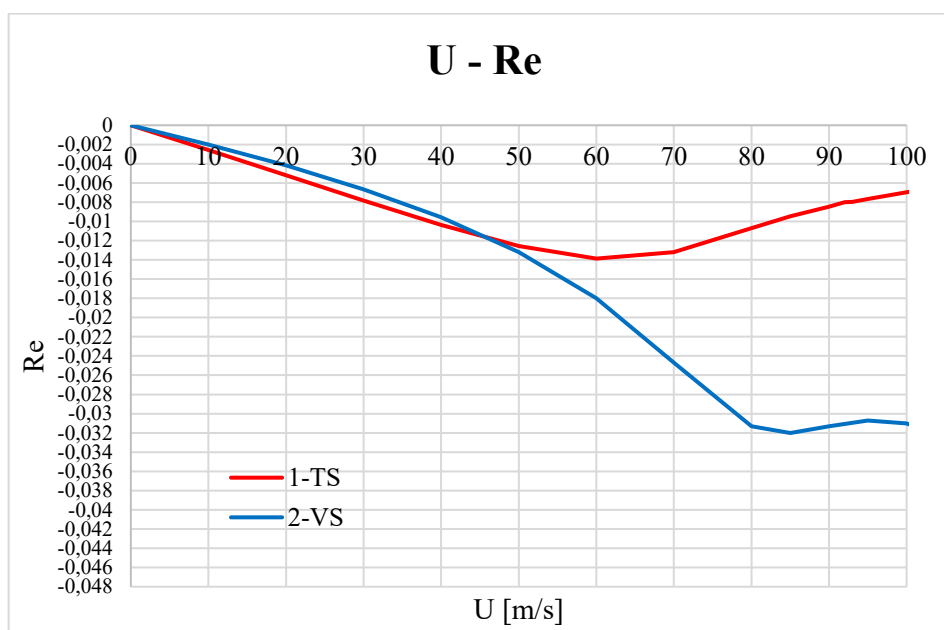


Figure 6.16 - Variation of the real part of complex eigenvalues

No flutter instability was detected in this analysis within the 0-100 m/s wind speed range. In fact, the real part, which provides information about the stability of the solution, assumes negative values throughout the considered wind speed interval for both analysed modes.

### 6.2.3 Results comparison

It is relevant to show the difference between these cases in terms of numerical results. In Table 6.2, where present, the critical values of instability are shown.

Table 6.2 - ANSYS Flutter Analysis on Central Span Models, result comparison

ANSYS - Central span models					
	Flutter derivatives	U_cr [m/s]	f_cr [Hz]	%Δ U_experimental	%Δ f_experimental
1-axis model	Experimental	95	0.1756	-	-
	Andersen	>100	-	-	-
	Andersen with $\mu=0.7$	94.0	0.189	-1.1%	7.6%
2-axes model	Theodorsen	>100	-	-	-

As evident from Table 6.2, it is valuable to compare the results obtained using experimental flutter derivatives with those obtained using the reduced Andersen's flutter derivatives. This comparison reveals similarities in the results, which warrant further investigation.

It worths noting that in all models compared in this section, an interaction between the investigated modal branches is found between 75 and 85 m/s. The interaction is evident from the *veering* of the vertical and torsional modal branches which can be observed in Figures 6.8, 6.11, 6.13 and 6.15. As usual [30], the detected *veering* was characterised by the mutual exchange of vertical and torsional modal shape component, which is not explored in detail in this section for the sake of brevity.

Nevertheless, in two of the four models, the interaction was not such to trigger the flutter phenomenon.



## 6.3 Flutter analysis of complete models in ANSYS

### 6.3.1 Single-axis model

The damped complex eigenvalue analyses were conducted on the complete model under wind velocities ranging from 0 to 120 m/s (0 to 432 km/h). For the experimental derivatives case, the range is limited to 0-100 m/s, because for values higher than 100, the reduced velocities exceed the domain studied in wind tunnel. The incremental step of wind velocity was set variable, from a standard value of 10 m/s to a minimum of 1 m/s when the instability was expected.

The computational steps have been followed for the two modes coupling in flutter instability: the first symmetric torsional one and the second symmetric vertical one.

Following the approach outlined for the analytic model in Section 6.1, the Flutter Analyses were conducted using different sets of flutter derivatives for the models described in Section 5.2.

#### 6.3.1.1 Experimental flutter derivatives

The results obtained for the complete 1-axis model using flutter derivatives are plotted below (Figures 6.17 and 6.18).

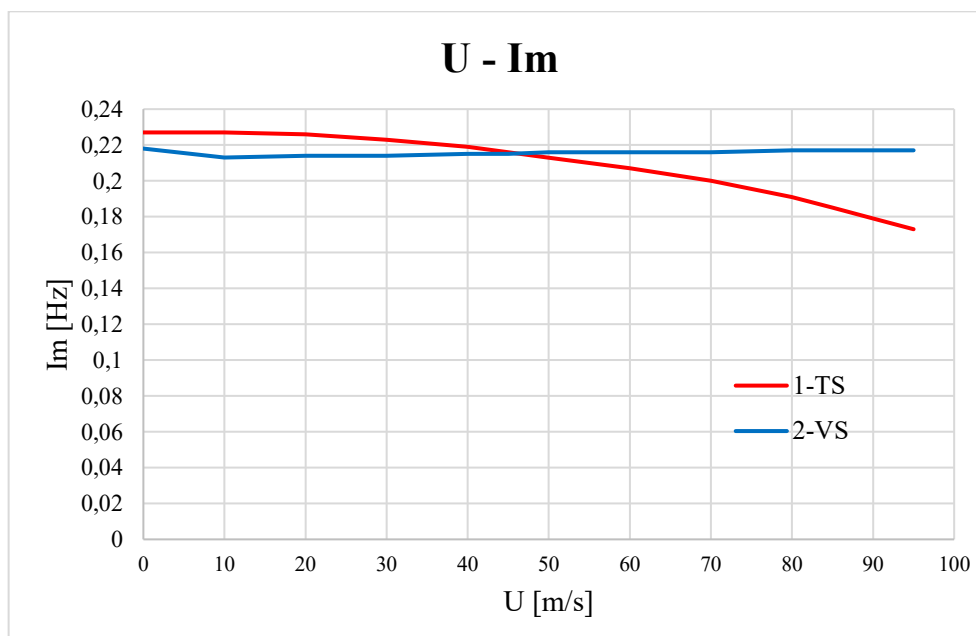


Figure 6.17 - Variation of the imaginary part of complex eigenvalues

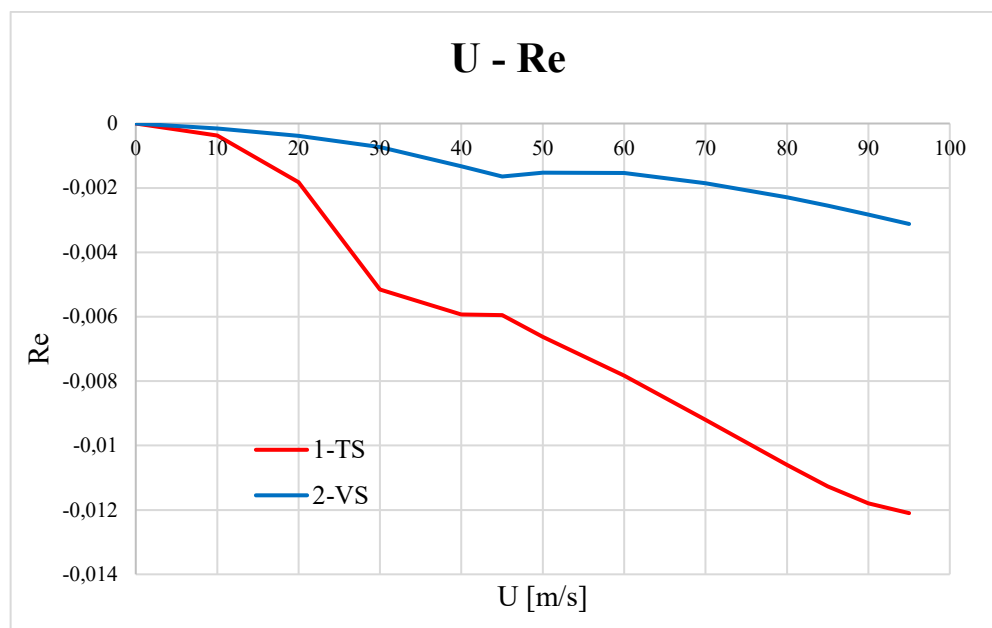


Figure 6.18 - Variation of the real part of complex eigenvalues

No flutter instability was detected in this analysis within the 0-100 m/s wind speed range. In fact, the real part, which provides information about the stability of the solution, assumes negative values throughout the considered wind speed interval for all analysed modes, including the first symmetric torsional mode, which is responsible for instability in two of the other three cases.

Furthermore, no positive slope is detected for the two curves, so it can be deduced that the flutter instability risk is removed in this velocity range.

It is interesting to note that the *crossing* phenomenon is present around 45 m/s.

### 6.3.1.2 Andersen's flutter derivatives

In this Section, analytical flutter derivatives obtained with the Superposition of flat plates method (Section 4.2) are used to estimate the critical value of the velocity and frequency. The outcomes of the analyses are shown in Figures 6.19 and 6.20.

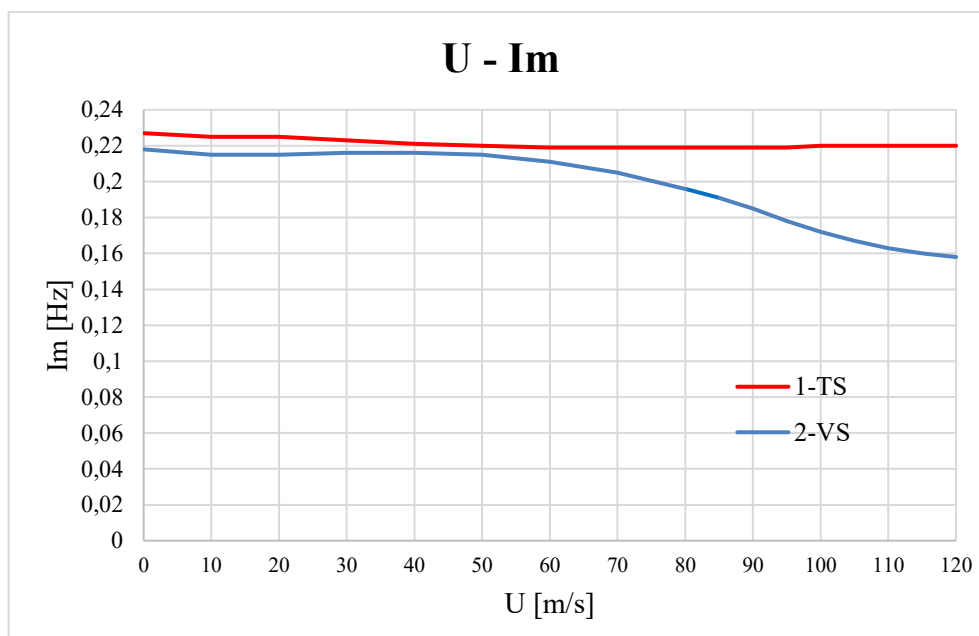


Figure 6.19 - Variation of the imaginary part of complex eigenvalues

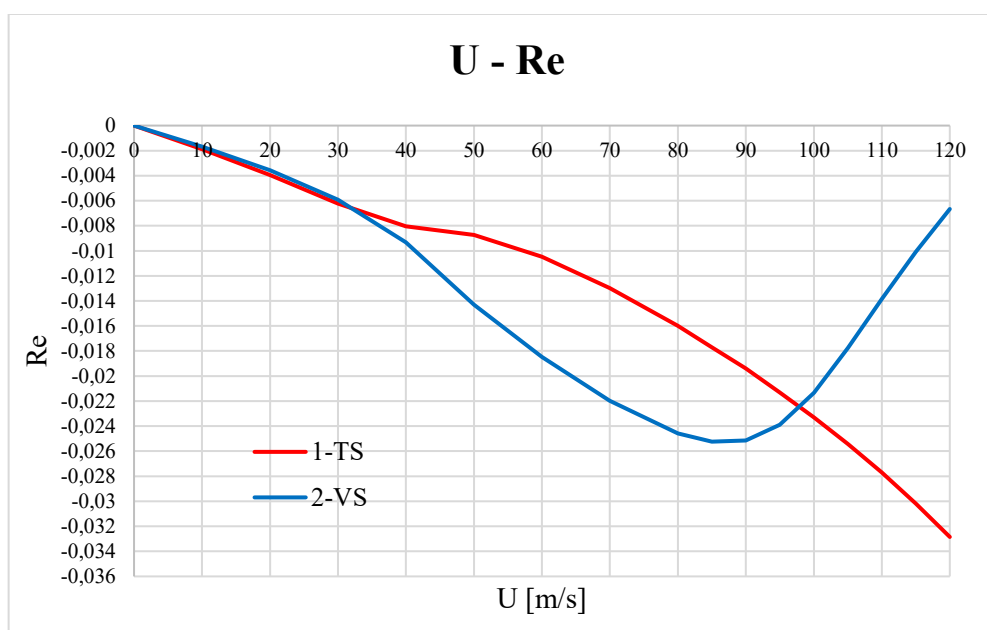


Figure 6.20 - Variation of the real part of complex eigenvalues

No flutter instability was detected in this analysis within the 0-100 m/s wind speed range. In fact, the real part, which provides information about the stability of the solution, assumes negative values throughout the considered wind speed interval for all analysed modes, including the first symmetric torsional mode, which is responsible for instability in two of the other three cases.

These results are possible due to the overestimation of aeroelastic instability using simplified calculations of flutter derivatives.

However, the positive slope blue curve might suggest the flutter instability will occur for velocity higher than 120 m/s.

Contrary to the previous case, around 45m/s *veering* phenomenon is present. From this velocity value, the two modal deformed shape exchange each other: the torsional branch is characterized by the vertical deformation and vice versa. As usual for the curve *veering*, the corresponding eigenvectors exhibit a dramatic yet continuous change, which is associated to a modal shapes variation. This phenomenon is called *mode localization* [30].

### 6.3.1.3 Andersen's flutter derivatives with gap-width scaling factor

The analysis is performed considering the coefficient discussed in Section 4.2.1, to address contrast the overestimation found in previous case. In Figures 6.21 and 6.22, the evolution of the real and imaginary part of the eigenvalues provided by the analysis is shown.

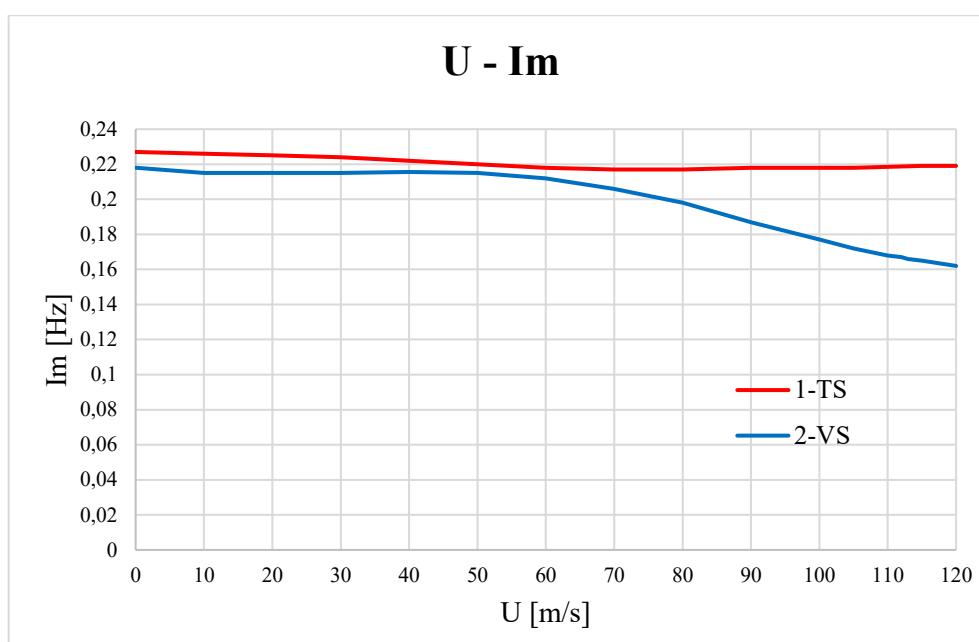


Figure 6.21 - Variation of the imaginary part of complex eigenvalues

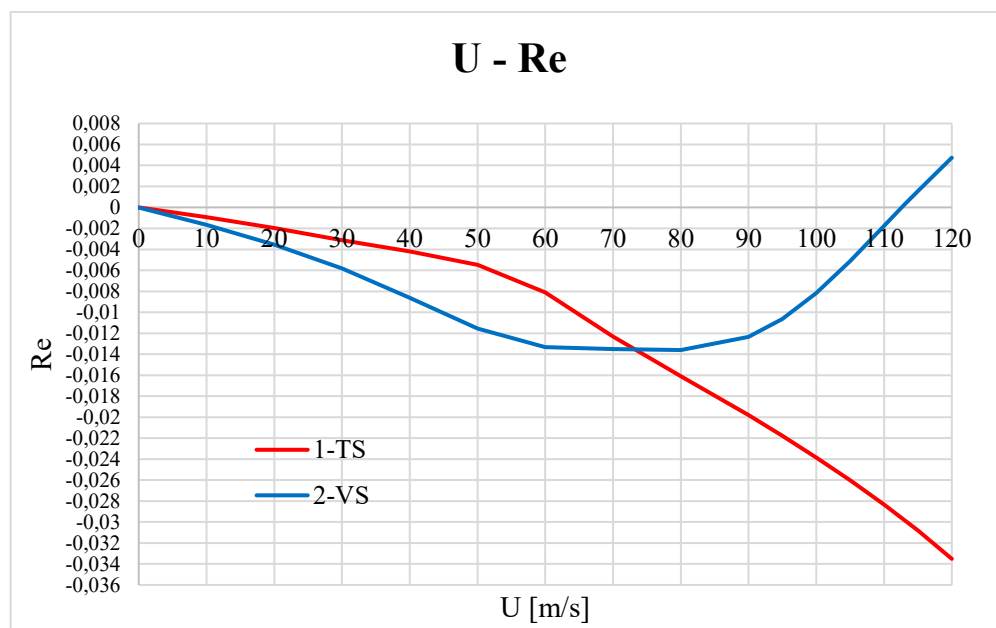


Figure 6.22 - Variation of the real part of complex eigenvalues

The analysis produced a critical flutter wind speed of 113 m/s and a corresponding critical frequency of 0.166 Hz.

As in the previous case, *veering* phenomenon can be noticed from 45 m/s on, and so also *mode localization* phenomenon is present.

### 6.3.2 Double-axis model

#### 6.3.2.1 Theodorsen's flutter derivatives

The results obtained for the complete 2-axis model using Theodorsen's flutter derivatives are plotted below (Figures 6.23 and 6.24).

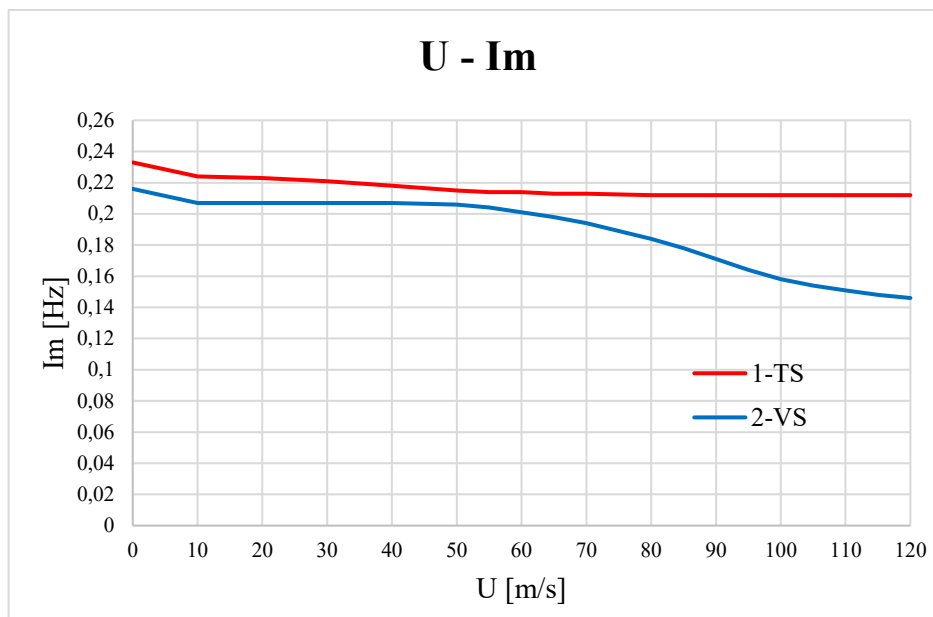


Figure 6.23 - Variation of the imaginary part of complex eigenvalues

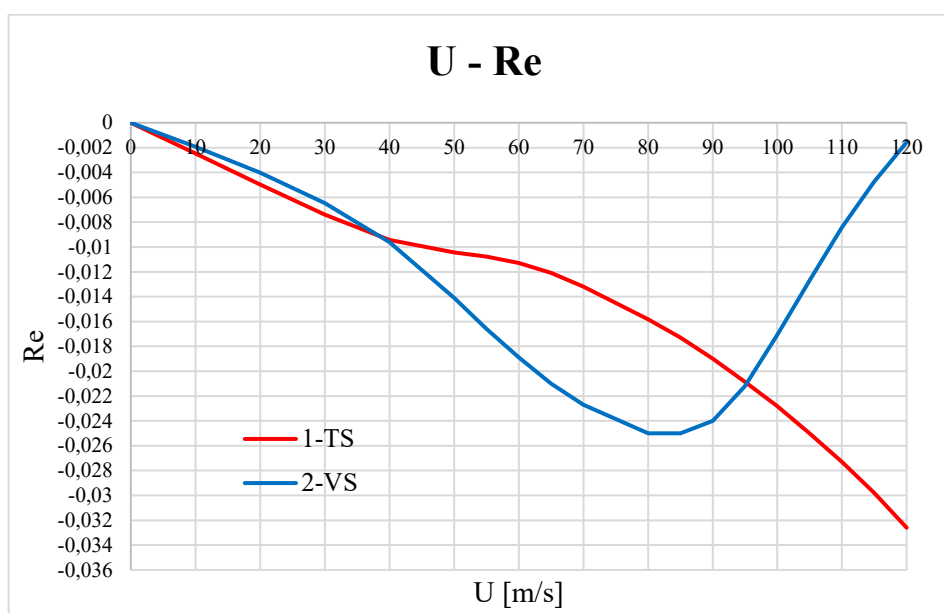


Figure 6.24 - Variation of the real part of complex eigenvalues

No flutter instability was detected in this analysis within the 0-120 m/s wind speed range. In fact, the real part, which provides information about the stability of the solution, assumes negative values throughout the considered wind speed interval for all analysed modes, including the first symmetric torsional mode, which is responsible for instability in two of the other three cases.

However, the positive slope blue curve might suggest the flutter instability may occur for velocity higher than 120 m/s.

As in the previous 1-axes cases, *veering* phenomenon can be noticed around 45 m/s, and so also *mode localization* phenomenon is present.

### 6.3.3 Results comparisons

Evaluating the shape of the branches of the graphs described above, it is interesting to note that the Imaginary branches of Figure 6.17 (Experimental derivatives) is characterized by a *crossing* whereas the ones found with Andersen (Figures 6.19 and 6.21) and Theodorsen's (Figure 6.23) derivatives are characterized by a *veering*. This comports a difference in the real parts curves: for increasing speed values, it is noted that the torsional branch (named in this way because at null velocity, the deformed shape is torsional) is characterized by a vertical deformed shape and viceversa. As well-known [30], the *veering* between vertical and torsional frequency branches denotes interaction between vertical and torsional motion which is highlighted by the mutual exchange of the displacement components characterizing the modal branches. It is worth noting that when the *veering* of the frequency loci is observed (Figures 6.19, 6.21 and 6.23), the real component of the vertical branch begins to increase following the interaction, indicating a destabilizing coupling, eventually leading to flutter in the case of Section 6.3.1.3. Due to the modal shape exchange, flutter originated by the vertical branch is physically consistent with the more common flutter originating from the torsional branch [30]

On the other hand, when the modal branches cross each other without interacting (Figure 6.18), the real eigenvalue components remain negative proving the absence of the degree-of-freedom.

It is also relevant to show the difference between these cases in terms of numerical results. In Table 6.3, where presents, the critical values of instability are presented.

Table 6.3 - ANSYS Flutter Analysis on Complete Models, result comparison

ANSYS - Complete models			
	Flutter derivatives	U_cr [m/s]	f_cr [Hz]
1-axis model	Experimental	>100	-
	Andersen	>120	-
	Andersen with $\mu=0.7$	113.0	0.166
2-axes model	Theodorsen	>120	-

Only with the use of reducing coefficient on Andersen's derivatives, it is reached a critical value. This confirms, as found in Section 6.1 and 6.2, that this coefficient leads to reduce the overestimation of the simplified calculation of those derivatives.

It must also be considered that the complete model used in these analyses could have less accuracy, due to more hypothesized data. In particular, boundary conditions of this model could need more studies to reach more significant and realistic results.

## 6.4 Comparison of different models' results

In conclusion, the flutter wind speed and the flutter frequency derived from the ANSYS models and MATLAB analytic analysis in this chapter, are compared with the results obtained by Yu et al. [22]. For simplicity, the comparison is based on only one of the several analyses presented in [22]. In particular, the results from the two-dimensional flutter analysis were selected, as these can be directly compared with the analytical analysis in Section 6.1.

Table 6.4 - Flutter Analysis on different models, result comparison

%Δ		Literature	Experimental flutter derivatives			Andersen flutter derivatives with $\mu=0.7$		
		<i>Yu et al.</i>	MATLAB	ANSYS Central span model	ANSYS Complete model	MATLAB	ANSYS Central span model	ANSYS Complete model
$U_{cr}$	[m/s] (%Δ vs Lit.)	91.367 (-)	97.5 (6.7%)	95 (4.0%)	-	94.7 (3.6%)	94 (2.9%)	113 (23.7%)
$f_{cr}$	[Hz] (%Δ vs Lit.)	0.1456 (-)	0.177 (20.9%)	0.1756 (20.6%)	-	0.193 (32.6%)	0.189 (29.8%)	0.166 (14.0%)

In this table the results of the previous sections are reported in terms of difference with the studies of *Yu et al.* [22]. The analysis using the 2-axis models with Theodorsen's derivatives was omitted since no flutter instability was observed. Similarly, results from analyses using only Andersen's derivatives are not presented. This may be due to the idealized or simplified assumptions inherent in the two methods used to calculate flutter derivatives (Chapter 4), which can lead to an overestimation of the flutter analysis results.

As it is clear from Table 6.4, the ANSYS flutter analysis produced accurate values in terms of flutter wind velocity for the central span models. In fact, for both analysis using different derivatives, the relative error is less than 4%. This models, however, led higher differences in terms of flutter frequency. This may be due to the errors observed in the modal analysis (Section 5.3), which can, in turn, be attributed to the asymmetry of the bridge, featuring a supported deck on one side and a suspended deck on the other.

On the other hand, the analysis conducted on the complete model using Andersen's derivatives (considering reduced non-dimensional gap-width), reached more accurate estimation result of flutter frequency, but moving away from the realistic outcome of flutter wind velocity. This latest result should be interpreted with caution, given the uncertainty of the input data and boundary conditions.

In conclusion, the comparison with the MATLAB results is particularly valuable, as both this analysis and the ANSYS study on the central span model yield nearly identical outcomes. This is reached involving different approaches and for different flutter derivatives cases. This is due to the similar hypothesis of both multi-order flutter analysis in MATLAB and the full-order flutter analysis in ANSYS.



For the case study analysed, the vertical branch flutter observed in complete models (in Section 6.3) is consistent with the torsional branch flutter detected by the central span models (in Section 6.2) and aeroelastic analysis performed with the MATLAB code (in Section 6.1). Thus, the phenomenon of transfer of the instability between eigenvalue branches [31] is observed due to the variation of certain analysis parameters.

## Chapter 7 - Conclusions

This Thesis provides an in-depth exploration of flutter instability in long-span suspension bridges, with a particular focus on enhancing aerodynamic stability through multi-box girder designs. The multi-box configuration offers, in fact, significant improvements in aerodynamic stability compared to the traditional single-box design.

This Thesis attempts to assess the problem using both analytical and numerical approaches based on flutter derivatives obtained through different simplified calculations. This is done using the Xihoumen Bridge as a case-study.

Initially a zero-wind modal analysis is performed for all Finite Element models described in Section 5.2. The results, in terms of natural frequencies, are compared with those found in the literature. Preliminary conclusions can be drawn, highlighting that the central span models produce more accurate results than the complete models. The complete models were developed with the aim of reproducing the real design as accurately as possible. In particular, an effort was made to directly model the structural elements involved in the interaction between central span, towers, and the lateral spans. As a drawback, complete models required more assumptions in the input parameters due to the absence of some mechanical and geometrical data. This could be the reason why central span models produced more accurate and robust results.

A variety of methodologies for estimating flutter derivatives were introduced and discussed. The aim was to evaluate the accuracy of the analytical and numerical predictions given by simplified formulas.

Theodorsen's flat plate theory [12] was discussed in Section 4.2 and through this method flutter derivatives were obtained and applied to both axes of the 2-axis models, each considered as a flat plate that spans the width of the single box.

On the other hand, the superposition of Theodorsen's flat plates, introduced by Andersen [27], was employed for the estimation of the twin-box derivatives assigned to the 1-axis models.

In addition, in Chapter 4, the gap-width sensitivity of multi box girders is examined through a scaling factor that reduces the gap between the total deck's centroid and the single box's barycentre in the Andersen formulas.

Flutter derivatives provided by the discussed simplified approaches were finally compared with literature values obtained with sophisticated experimental tests on reduced models in the wind tunnel.

Andersen's methods provided a good estimation for  $A_3^*$  flutter derivative, which describes the aerodynamic torsional stiffness. In the same way, the application of the gap-width scaling factor slightly improved the estimation of the  $A_2^*$  flutter derivative, which describes the aerodynamic

torsional damping. On the other hand, the flutter derivatives  $A_1^*$ ,  $A_4^*$ ,  $H_1^*$ ,  $H_2^*$ ,  $H_3^*$ , and  $H_4^*$  showed no variation regardless of whether the gap-width scaling factor is applied, as they are independent of the non-dimensional distances  $a_j$ .

Theodorsen's method showed good agreement for the  $A_1^*$ ,  $A_2^*$ ,  $A_4^*$ ,  $H_3^*$ , and  $H_4^*$  flutter derivatives. In contrast, it significantly underestimates  $A_3^*$ , the aerodynamic torsional stiffness derivative that plays a crucial role in stiffness-driven (classic) flutter.

Following the studies proposed by Hua and Chen [16] [15], the flutter analyses were carried out as iterative modal damped analyses in the ANSYS APDL Finite Element package. The comparison of the results obtained with literature data showed that the ANSYS flutter analyses produced accurate values in terms of flutter wind velocity for central span model, with relative errors less than 4%. This model, however, produced higher differences in terms of flutter frequency. This may be due to the errors previously detected in the modal analysis (Section 5.3), which can, in turn, be attributed to the asymmetry of the bridge, featuring a supported deck on one side and a suspended deck on the other.

On the other hand, the analysis conducted on the 1-axis complete model using Andersen's derivatives (including the gap-width scaling factor), achieved a more accurate estimation result of flutter frequency, but moving away from the realistic outcome of flutter wind velocity. This outcome should be approached with caution due to uncertainties in the input data and the boundary conditions documented in the literature for the complete model.

In the analysis conducted on the 2-axis models with Theodorsen's derivatives, no flutter instability was observed. The same result has been observed in all models studied using Andersen's derivatives (without the scaling factor) and also when experimental flutter derivatives were applied to the complete 1-axis model. This may be due to the idealized or simplified assumptions done, in particular in the two methods used to calculate flutter derivatives (Chapter 4), which can lead to an overestimation of the flutter analysis results.

Ultimately, the comparison with the MATLAB results was particularly valuable, as both this analysis and the ANSYS study on the 1-axis central span model yield nearly identical outcomes. This was achieved using different approaches and for different cases of flutter derivatives. The alignment of the results obtained can be ascribed to the similar hypothesis of both multi-order flutter analysis in MATLAB and the full-order flutter analysis in ANSYS.

In general, the differences in flutter derivatives observed in Figure 4.5 and discussed in Section 4.4 are partially confirmed by the outcomes of the flutter analysis conducted in Chapter 6 as well as by experiments reported in the literature. In fact, it is worth noting that the presence of gap-width provides a reduction of  $A_2^*$  (a stabilizing contribution) and an increase of  $A_3^*$  (a destabilizing contribution). Andersen's formulas, through the superposition approach, capture this phenomenon, generally leading to an increase in the flutter critical speed compared to Theodorsen's method, due to the predominant effect of  $A_2^*$ . This is one reason why multi-box girders are inherently more stable than single-box ones.

The simplified methods adopted in this Thesis, due to the simplifications and assumptions introduced, could not explain comprehensively the complex aerodynamic behaviour of the multi-box deck but could provide a good starting point to analyse the aeroelastic instability without experimental tests in wind tunnel. Future more detailed studies could consider flutter derivatives calculated by analytical formulations based on the aerodynamic static coefficients [32], which may be determined using Computational Fluid Dynamics (CFD) [33] or, more generally, with extensive experimental data. A comparison with the experimental flutter derivatives will allow to assess validity and limitations of such simplified approaches.

## References

- [1] “Wikipedia.” Accessed: Mar. 10, 2025. [Online]. Available: [https://en.wikipedia.org/wiki/List\\_of\\_longest\\_suspension\\_bridge\\_spans#:~:text=The%201915%20%C3%87anakkale%20Bridge%20in%20Turkey%20holds%20the%20record%20since,1%2C991%20metres%20\(6%2C532%20ft\)](https://en.wikipedia.org/wiki/List_of_longest_suspension_bridge_spans#:~:text=The%201915%20%C3%87anakkale%20Bridge%20in%20Turkey%20holds%20the%20record%20since,1%2C991%20metres%20(6%2C532%20ft))
- [2] W. Lin and T. Yoda, “Suspension Bridges,” in *Bridge Engineering*, Elsevier, 2017, pp. 195–211. doi: 10.1016/B978-0-12-804432-2.00011-6.
- [3] “Encyclopædia Britannica, Inc.” Accessed: Mar. 10, 2025. [Online]. Available: <https://www.britannica.com/technology/suspension-bridge>
- [4] S. Russo, “FLUID-DYNAMICS AND FLUTTER ANALYSIS OF THE GEORGE WASHINGTON SUSPENSION BRIDGE [Master Thesis],” 2018.
- [5] F. Di Agabito, “ANALYSIS OF SUSPENSION BRIDGES IN ANSYS: THE AKASHI KAIKYO BRIDGE CASE-STUDY [Master Thesis],” 2017.
- [6] L. Vailati, “Flutter instability of long-span suspension bridges: The case-study of the 1915Çanakkale Bridge in Turkey [Master Thesis],” 2023.
- [7] “Teknoring.” Accessed: Mar. 14, 2025. [Online]. Available: <https://www.teknoring.com/ingegneria/1915-canakkale-bridge-turchia-ponte-sospeso-piu-lungo-del-mondo/>
- [8] S. Huang, “FLUTTER ANALYSIS OF LONG-SPAN SUSPENSION BRIDGES: THE CASE-STUDY OF THE MESSINA STRAIT PROJECT [Master Thesis],” 2022.
- [9] A. Carpinteri, *Advanced Structural Mechanics*. CRC Press, 2017. doi: 10.1201/9781315375298.
- [10] G. Piana and A. Carpinteri, “Course of ‘Static and Dynamic Instability of Structures’ - Practice lecture - Examples of calculation for suspension bridges (aeroelastic instability),” Torino, 2023.
- [11] R. H. Scanlan and J. J. Tomko, “Airfoil and Bridge Deck Flutter Derivatives,” *Journal of the Engineering Mechanics Division*, vol. 97, no. 6, pp. 1717–1737, Dec. 1971, doi: 10.1061/JMCEA3.0001526.
- [12] Theodore Theodorsen, “General Theory of Aerodynamic Instability and the Mechanism of Flutter,” *American Institute of Aeronautics and Astronautics*, 1935.
- [13] G. Piana and A. Carpinteri, “Long-span Suspension Bridge Flutter Analysis with Drag Force Effects,” *Journal of Applied and Computational Mechanics*, vol. 7, pp. 1077–1089, 2021, doi: 10.22055/JACM.2021.32481.2025.
- [14] S. Russo, G. Piana, and A. Carpinteri, “Multimodal aeroelastic analysis of suspension bridges with aerostatic nonlinearities,” in *Journal of Physics: Conference Series*, Institute of Physics, 2024. doi: 10.1088/1742-6596/2647/24/242006.

- [15] X. G. Hua and Z. Q. Chen, “Full-order and multimode flutter analysis using ANSYS,” *Finite Elements in Analysis and Design*, vol. 44, no. 9–10, pp. 537–551, Jun. 2008, doi: 10.1016/j.finel.2008.01.011.
- [16] X. G. Hua, Z. Q. Chen, Y. Q. Ni, and J. M. Ko, “Flutter analysis of long-span bridges using ANSYS,” *Wind and Structures*, vol. 10, no. 1, pp. 61–82, Feb. 2007, doi: 10.12989/was.2007.10.1.061.
- [17] H. Song, “Zhoushan Xihoumen Bridge with the World Record Span Length of Steel Box Girder, China.”
- [18] Glabb [User], “Wikimedia Commons.” Accessed: Mar. 02, 2025. [Online]. Available: <https://commons.wikimedia.org/w/index.php?curid=125090629>
- [19] G. Jian, “Key technical innovation of Xihoumen Bridge - the longest steel box gird suspension bridge in the world,” *Engineering Sciences*, 2010.
- [20] Y. Deng, S. Li, M. Zhang, X. Lei, and Z. Chen, “Wake-Induced Vibrations of the Hangers of the Xihoumen Bridge,” *Journal of Bridge Engineering*, vol. 26, no. 10, Oct. 2021, doi: 10.1061/(asce)be.1943-5592.0001779.
- [21] Tyg728 [User], “Wikimedia Commons.” Accessed: Mar. 02, 2025. [Online]. Available: <https://commons.wikimedia.org/w/index.php?curid=83025016>
- [22] M. Yu, H. Liao, M. Li, C. Ma, and M. Liu, “Analysis of flutter stability of the Xihoumen bridge in the completed stage,” in *Advanced Materials Research*, 2011, pp. 1629–1633. doi: 10.4028/www.scientific.net/AMR.243-249.1629.
- [23] X. Chu, H. N. Sinh, W. Cui, L. Zhao, and Y. Ge, “Life-cycle assessment for flutter probability of a long-span suspension bridge based on field monitoring data,” Jun. 2021, [Online]. Available: <http://arxiv.org/abs/2106.10694>
- [24] H. Li *et al.*, “Investigation of vortex-induced vibration of a suspension bridge with two separated steel box girders based on field measurements,” *Eng Struct*, vol. 33, no. 6, pp. 1894–1907, Jun. 2011, doi: 10.1016/j.engstruct.2011.02.017.
- [25] S. J. Jiang, Y. L. Xu, J. Zhu, G. Q. Zhang, and D. H. Dan, “Vortex-Induced Force Identification of a Long-Span Bridge Based on Field Measurement Data,” *Struct Control Health Monit*, vol. 2023, 2023, doi: 10.1155/2023/9361196.
- [26] S. de Miranda, L. Patrino, F. Ubertini, and G. Vairo, “Indicial functions and flutter derivatives: A generalized approach to the motion-related wind loads,” *J Fluids Struct*, vol. 42, pp. 466–487, Oct. 2013, doi: 10.1016/j.jfluidstructs.2013.08.009.
- [27] M. S. Andersen, M. B. Eriksen, S. V. Larsen, and A. Brandt, “The influence of gap- and chord-widths for multi-box girders: Superposition of flat plate flutter derivatives and section model tests,” *J Fluids Struct*, vol. 109, Feb. 2022, doi: 10.1016/j.jfluidstructs.2021.103489.
- [28] ANSYS, *ANSYS Mechanical APDL Element Reference*. 2011.
- [29] M. Como, “Stabilità aerodinamica dei ponti di grande luce,” in *Ingegneria delle strutture*, vol. 2, Elio Giangreco, Ed., UTET, 2002.
- [30] X. Chen and A. Kareem, “Curve Veering of Eigenvalue Loci of Bridges with Aeroelastic Effects”, doi: 10.1061/ASCE0733-93992003129:2146.
- [31] A. P. Seyranian and A. A. Mailybaev, *Multiparameter Stability Theory with Mechanical Applications*, vol. 13.

- [32] S. Russo, G. Piana, and A. Carpinteri, “On the simplified calculation of multi-box deck flutter derivatives.”
- [33] S. Russo, G. Piana, L. Patruno, and A. Carpinteri, “Preliminary Flutter Stability Assessment of the Double-Deck George Washington Bridge,” *Applied Sciences (Switzerland)*, vol. 13, no. 11, Jun. 2023, doi: 10.3390/app13116389.